NOVEL REACTION PROCESSING TECHNIQUES FOR THE FABRICATION OF ULTRA-HIGH TEMPERATURE METAL/CERAMIC COMPOSITES WITH TAILORABLE MICROSTRUCTURES

A Dissertation
Presented to
The Academic Faculty

by

David William Lipke

In Partial Fulfillment
Of the Requirements for the Degree
Doctor of Philosophy in Materials Science and Engineering

Georgia Institute of Technology

May, 2011

NOVEL REACTION PROCESSING TECHNIQUES FOR THE FABRICATION OF ULTRA-HIGH TEMPERATURE METAL/CERAMIC COMPOSITES WITH TAILORABLE MICROSTRUCTURES

Approved by:

Dr. Kenneth H. Sandhage, Advisor
School of Materials Science
and Engineering
Georgia Institute of Technology

Dr. Wesley P. Hoffman
Propulsion Directorate
Air Force Research Laboratory

Dr. W. Brent Carter
School of Materials Science
and Engineering
Georgia Institute of Technology

Dr. Arun M. Gokhale
School of Materials Science
and Engineering
Georgia Institute of Technology

Dr. Thomas H. Sanders, Jr.
School of Materials Science
and Engineering
Georgia Institute of Technology

Date Approved: December 12, 2010

Acknowledgements

My development as a scientist is owed to the numerous brilliant individuals whose experience and wisdom persevered in the face of my oftentimes woeful ignorance. I am especially indebted to my advisor, Dr. Kenneth Sandhage, whose guidance and patience in the face of slow research progress has enabled me to come to this point. I am also especially thankful for the assistance of Dr. Yunshu Zhang and Dr. Ye Cai, without whose expertise in high temperature processing and transmission electron microscopy, respectively, this research could not have been completed. I would like to thank my advisor and the members of my dissertation committee – Dr. Brent Carter, Dr. Arun Gokhale, Dr. Wesley Hoffman and Dr. Thomas Sanders – for their guidance and direction throughout the course of this research. I am also grateful to the Air Force Office of Scientific Research, whose sponsorship of this research under program manager Dr. Joan Fuller enabled my tenure during these past five years. To that end, I also thank the Boeing Corporation for their fellowship award which considerably eased the financial burden living on a graduate stipend in urban Atlanta.

Every member of the Sandhage research group past and present has contributed in some way to this research, whether in one of our frequent philosophical discussions or problem solving sessions or in contribution to research and lab maintenance. (In alphabetical order) Thank you to Dr. Gul Ahmad, Shawn Allen, Dr. Zhihao Bao, Daniel Berrigan, Craig Cameron, Dr. Benjamin Church, Stan Davis, Dr. Matthew Dickerson, Eric Ernst, Dr. Yunnan Fang, Ari Gordin, Phillip Graham, Dr. Michael Haluska, Dr.

Yajun Liu, Taylor McLaughlin, Dr. Samuel Shian, Amy Spero, Jonathan Vernon, Dr. Michael Weatherspoon and Dr. Qingzhong Wu.

I would like also to thank friends and family, without whose support and camaraderie I would be a lesser person. Thank you especially to my mother, Arlene Gerken, and my father, Kenneth Lipke, and my sister, Elizabeth Bowen.

Table of Contents

List of Tables

List of Figures

List of Symbols and Abbreviations

ΔG^{o}	standard Gibbs free energy change
CTE	coefficient of thermal expansion
DCP	Displacive Compensation of Porosity
Z	solid volume change of reaction
Ψ	minimum pore volume fraction capable of accommodating solid volume change of reaction
f	volume fraction of reacting species in preform
CNC	computer numerical controlled
3DP	three-dimensional printing
AAc	ammonium acetate
RS	rice starch
PEI	polyethylene imine
SEM	scanning electron microscopy
XRD	x-ray diffraction
EDS	energy dispersive spectroscopy
TEM	transmission electron microscopy
HRTEM	high resolution transmission electron microscopy
SAED	selected area electron diffraction
BET	Brunauer-Emmett-Teller
H	W:WC peak area ratio from x-ray diffraction pattern
X	molar extent of reaction
Λ	net change in number of moles of ideal gas due to reaction
ρ	mass density
U	volume
ζ	average linear dimension change upon reaction
V	volume fraction
$\bar{V}$	molar volume
β	instantaneous reactant ratio within reactively infiltrated body
Γ	molar extent of reaction occurring during infiltration
r	radius
Y	molar ratio of phases in product layer
Σ	reaction stoichiometry
m	weight
n	number of moles
a	activity
AW,MW	atomic or molecular weight
u	gas stream velocity
A	area
D	diffusion coefficient
δ	diffusion distance
F,G	invariant constants
Sc	Schmidt number
ν	kinematic viscosity

Ω	collision integral
σ	collision diameter
ε	Leonard-Jones interaction energy
L	length
b	lattice parameter
d	interplanar spacing
h,k,l	Miller indices
χ	Pauling electronegativity

Summary

Ultra-high temperature (i.e., > 2500°C) engineering applications present continued materials challenges. Refractory metal/ceramic composites have great potential to satisfy the demands of extreme environments (e.g., the environments found in solid rocket motors upon ignition), though general scalable processing techniques to fabricate complex shaped parts are lacking. The work embodied in this dissertation advances scientific knowledge in the development of processing techniques to form complex, near net-shape, near net-dimension, near fully-dense refractory metal/ceramic composites with controlled phase contents and microstructure.

Three research thrusts are detailed in this document. First, the utilization of rapid prototyping techniques, such as computer numerical controlled machining and three dimensional printing, for the fabrication of porous tungsten carbide preforms and their application with the Displacive Compensation of Porosity process is demonstrated. Second, carbon substrates and preforms have been reactively converted to porous tungsten/tungsten carbide replicas via a novel gas-solid displacement reaction. Lastly, non-oxide ceramic solid solutions have been internally reduced to create intragranular metal/ceramic micro/nanocomposites. All three techniques combined have the potential to produce nanostructured refractory metal/ceramic composite materials with tailorable microstructure for ultra-high temperature applications.

CHAPTER 1: Design and Fabrication of Porous Tungsten Carbide Preforms and their Application to the Production of Tungsten/Zirconium Carbide-Bearing Composites via the Displacive Compensation of Porosity Process

Discussions in this chapter are distinct from and expand upon the research presented in: Lipke, D.W., Zhang, Y., Liu, Y., Church, B.C. and Sandhage, K.H. "Near net-shape/net-dimension ZrC/W-based composites with complex geometries via rapid prototyping and Displacive Compensation of Porosity," *J. Euro. Ceram. Soc.*, **30**(11), 2265-2277 (2010).

1.1. *Summary*

Two methods of preform manufacture – computer numerical controlled machining of uniaxially cold pressed and sintered billets and three dimensional printing – are applied to the fabrication of porous tungsten carbide preforms for use in the Displacive Compensation of Porosity process to produce tungsten/zirconium carbide-bearing composites. Processing conditions leading to defect-free parts and controlled pore volume fractions are discussed. Microstructural features generated by each preform fabrication method, and subsequently retained in the produced composite, are examined. Theoretical models involved in preform design with applications to the production of reactively infiltrated composites are also detailed.

1.2. *Introduction*

Composites are multi-phase materials whose material properties of interest can exceed those of its monolithic constituents. For high-temperature applications, metal/ceramic composites offer great promise for improvements in mechanical properties such as fracture toughness[1] and resistance to creep[2], erosion[3] and thermal shock[4]. Metal/ceramic composites have been fabricated by a variety of techniques including hot

pressing[5], hot isostatic pressing[6], plasma spraying[7], chemical vapor infiltration[8] and reactive melt infiltration[9].

The Displacive Compensation of Porosity (DCP) process utilizes pressureless (capillary-driven) reactive infiltration of a porous ceramic preform to produce near net-shape/dimension parts with tailorable phase contents[10,11,12]. Reactions between a preform and liquid infiltrant can broadly be classified as either additive or displacive, the former combining elements to synthesize a new chemical compound while the latter forms new compounds by the redistribution of an element(s) from one phase to another. While additive reactions tend to be volume expansive (e.g. – Si/SiC composites produced via infiltration of molten silicon into carbon preforms[13]), such reactions taken alone are incapable of generating metal/ceramic composites whose operating temperature can greatly exceed its processing temperature due to the liquid infiltrant (or a derivative thereof) comprising the metal phase. By contrast, displacive reactions can generate metal phases whose melting points significantly exceed the processing temperature. While many embodiments of reactive melt infiltration processes (also called reactive casting) feature solid-volume reducing displacive reactions[14], DCP processes generate greater product volume than consumed reactant volume, resulting in reaction-induced densification.

The DCP process has been under investigation as a method for producing composites for extreme environments, such as solid fueled rocket motors (Figure 1), that must operate at ultra-high temperatures (i.e. - greater than 2500°C) under supersonic impingement by molten combustion products[15].

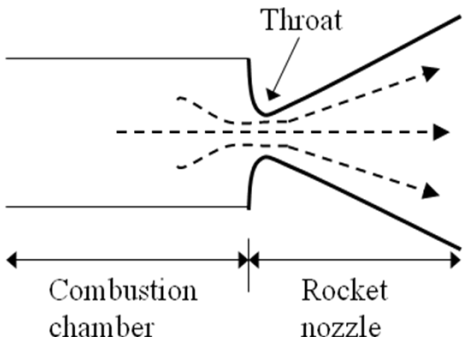

Figure 1: Solid rocket motor schematic

In particular, motor materials must exhibit exceptional erosion and thermal shock resistance. One family of composites with the potential to display such simultaneous properties is refractory metal/carbides. For example, W/ZrC-bearing composites can be created by the infiltration of zirconium-bearing liquids into a porous WC preform via the reaction:

$$\{Zr\} + WC \leftrightarrow W + ZrC \tag{1.1}$$

where {Zr} denotes zirconium as the reactive component of the infiltrating liquid. Pure zirconium melts at approximately 1850°C; in order to conduct reactive infiltration at lower temperatures, zirconium alloy compositions with low melting points must be used. One such alloy system is Cu-Zr, which forms a continuous liquid phase above 1125°C containing up to 75 at.% Zr. The selection of Cu has also been made owing to its chemical compatibility with W, exhibiting extremely limited mutual solubilities, and forming no compounds or low melting liquids[16]. Additionally, the presence of residual copper in minor quantities may not prove to be detrimental to the performance of the composite. For example, copper has been introduced to tungsten-based nozzles to enable transpirational cooling[15].

The Gibbs free energy change of reaction (1.1) can be calculated for a fixed temperature and pressure by:

$$\Delta G_{rxn} = RTln\left(\frac{Q}{K}\right) \tag{1.2}$$

where *K* is the reaction equilibrium constant and *Q* is the activity quotient defined by:

$$Q = \frac{a_W a_{ZrC}}{a_{\{Zr\}} a_{WC}} \tag{1.3}$$

For a fixed temperature and pressure, the minimum activity of zirconium in the infiltrating liquid for reaction (1.1) to proceed spontaneously to the right is found by substitution of (1.3) into (1.2), which, upon setting equal to zero and rearranging is:

$$a_{\{Zr\}} = \frac{1}{K}\left(\frac{a_W a_{ZrC}}{a_{WC}}\right) \tag{1.4}$$

Assuming that WC, W and ZrC are present in their pure reference states and in equilibrium, then their activities can be taken as unity. It has been estimated from available data[17,18,19,20,21] on the activity of Zr in Zr-Cu liquids as a function of composition and temperature that reaction (1.1) is thermodynamically favorable at 1300°C for concentrations of Zr in the melt greater than 920 ppm[15]. As a result, infiltrating liquid entrapped within the pores of the densifying body is typically observed to be nearly pure copper essentially entirely depleted of Zr.

The W/ZrC system possesses an attractive combination of thermochemical and thermomechanical characteristics. For example, the C-W-Zr phase diagram shown in Figure 2 reveals that W and ZrC are chemically compatible:

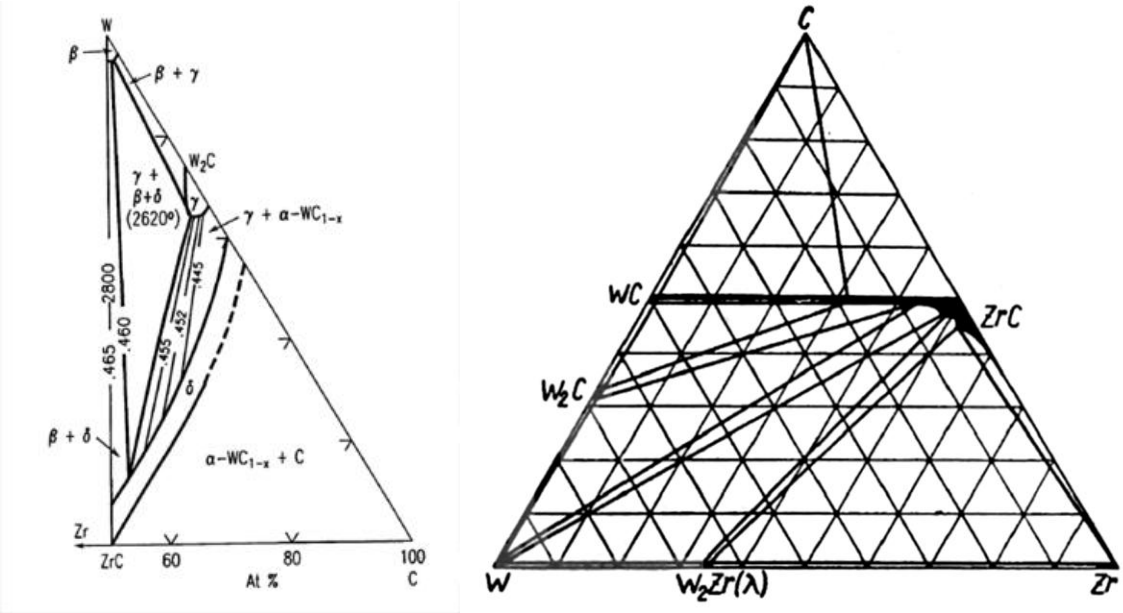

Figure 2: Ternary phase diagrams for the C-W-Zr system. (left) Pseudo-binary projection[22]; (right) Isothermal section at 1500°C[23].

The tie line between W and ZrC indicates that no intermediate compounds form in this system and the mutual solid solubilities are limited even at the eutectic melting temperature of 2800°C (e.g., 7 at. % W soluble in ZrC)[22]. Additionally, these two phases display thermomechanical compatibility as evidenced by their limited coefficient of thermal expansion (CTE) mismatch as shown in Figure 3 below[24,25]:

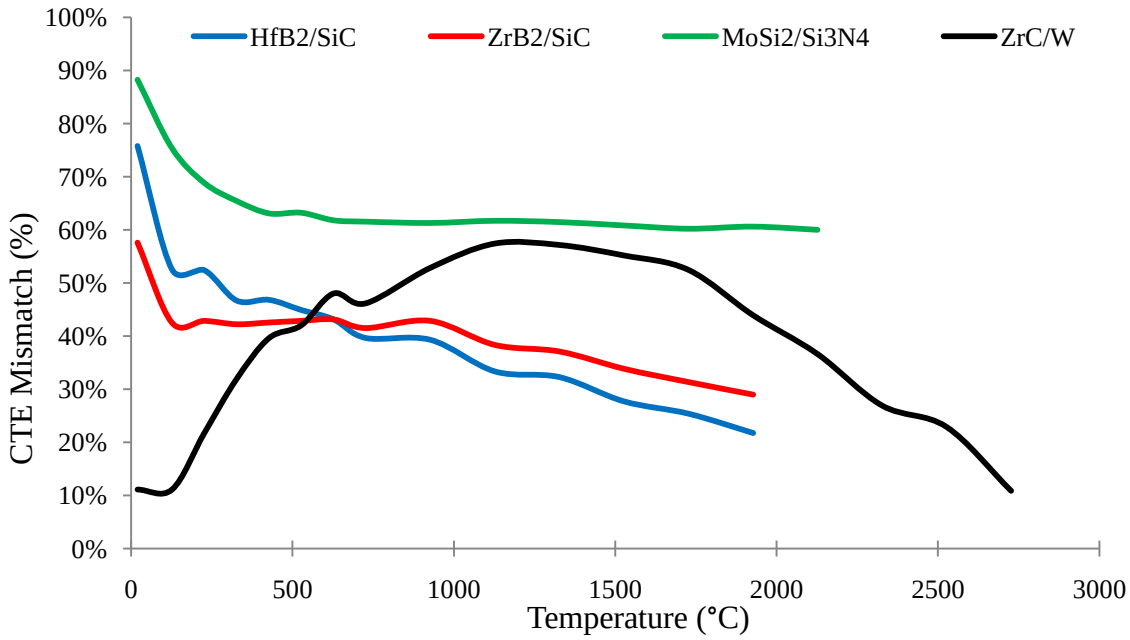

Figure 3: CTE mismatch for several high temperature composite compositions

The CTE mismatch for the metal/ceramic composite W/ZrC falls within the range of ceramic/ceramic and intermetallic/ceramic composites designed for use to similar maximum temperatures[26,27]. It is interesting to note that the maximum in the CTE mismatch (approximately 60%) coincides with the processing temperature at which W/ZrC composites are typically produced via the DCP process. Upon cooling from a processing temperature of 1100-1300°C, ZrC, having a higher CTE than W, is expected to be placed in tension, while, conversely, W is expected to be placed in compression. It has been speculated that this residual stress state may provide additional resistance to failure due to the thermal shock in a solid rocket motor. Upon heating, the residual tensile stress in ZrC is relieved, reaching a zero-stress state at the processing temperature of 1100-1300°C. Upon further heating, the stress state in ZrC becomes compressive, which may improve resistance to crack propagation.

W/ZrC composites are expected to exhibit other enhanced mechanical properties relative to monolithic counterparts based upon the materials property data summarized in Table 1:

Table 1: Selected thermal, mechanical and physical properties of W and ZrC

Property	W	ZrC
CTE[24,25] @ 25°C [1/°C]	4.5×10^{-6}	4.0×10^{-6}
CTE[24,25] @ 2700°C [1/°C]	9.2×10^{-6}	10.2×10^{-6}
Melting point[28] [°C]	3680	3445
Density[29] [g/cm^3]	19.259	6.633
Hardness[30,31] [kg/mm^2]	360	2900

The high hardness and low density of ZrC are expected to enhance erosion resistance[5] and provide weight savings relative to pure W, while the presence of ductile W is expected to improve toughness relative to pure ZrC[15].

Densification of metal/ceramic composites via the DCP process is caused by reaction-induced volume expansion within a porous, partially-sintered ceramic preform. The solid volume change, *Z*, defined as the change in solid product volume divided by the initial volume, for reaction (1.1) is +100.8% (see Table 3 for molar volume data). The minimum pore volume fraction, Ψ, required to accommodate the solid volume change upon complete reaction for a preform containing volume fraction *f* of reacting species, assuming no net change in external dimensions, is calculated as:

$$\Psi = \frac{Zf}{1 + Zf} \tag{1.5}$$

For a preform containing only WC ($f = 1$) undergoing reaction (1.1), Ψ = 50.2%. Rigid preforms whose porosity is greater than Ψ can accommodate the solid volume change upon complete reaction without change in external dimensions, with additional remaining

pore volume filled by the infiltrating liquid (depleted of its reactive constituents). On the other hand, preforms whose porosity is less than Ψ cannot accommodate the solid volume change upon complete reaction; therefore, partial reaction may occur until the pore volume is filled, leaving unreacted WC cores and causing premature pore closure (choke-off). For these reasons, controlling preform pore volume fraction is paramount for optimization of composites produced via the DCP process.

Two rapid prototyping methods of fabricating controlled porosity WC preforms with complex shapes have been implemented: computer numerical controlled (CNC) machining of uniaxially cold pressed/sintered billets and three dimensional (3-D) printing. This chapter is devoted to discussions of theoretical considerations, implementation, and application of these fabrication techniques to generate W/ZrC-bearing composites via the DCP process.

1.3. *Experimental Procedures*

Tungsten carbide preforms with controlled pore volume fraction were produced in cone, crucible, and nozzle shapes via CNC machining or 3-D printing. For all procedures, tungsten carbide powder (99.9% purity, 5-6 μm average diameter, Global Tungsten & Powders Corp., Towanda, PA) was used in the as-received state.

1.3.1. CNC Machining

Billets of WC having controlled pore volume fraction were produced by first uniaxially cold pressing a mixture of WC powder with either ammonium acetate (AAc) or rice starch (RS) as a binder. This was followed by inert atmosphere heat treatments to

achieve binder burnout and partial sintering. Pre-sintered billets were then shaped into predefined geometries via CNC machining.

A well-mixed blend of WC/AAc was achieved by mixing WC powder with 2.5 wt. % of an aqueous solution of 70 wt. % AAc (Sigma-Aldritch, St. Louis, MO) under mortar and pestle followed by drying at room temperature under vacuum desiccation for at least 12 hours (W.A. Hammond Drierite Co., Xenia, OH). The dried mixture was homogenized, and AAc agglomerates were eliminated, by low-energy ball milling at 260 rpm for 4 hours using 9.5 mm diameter WC media (Salem Specialty Ball Company, Canton, CT) in a polyethylene jar (75 mm diameter x 250 mm length) with loadings of 50 wt. % media relative to powder mixture filling approximately 50% of the milling jar volume. WC/AAc mixtures were packed into a stainless steel die (57 mm diameter) and uniaxially cold pressed to a peak pressure of 1.7 MPa to form billets of 35 mm height (corresponding to a nominal green density of 7.47 g/cm^3). Careful handling of the green body allowed for transfer of the billets onto MgO trays (99.4% purity, Ozark Technical Ceramics, Webb City, MO) which were subsequently placed at the center of the uniform hot zone of a 76 mm diameter mullite work tube (CoorsTek, Golden, CO) within a SiC-element resistance heated furnace. The tube was sealed at its ends using custom aluminum endcaps with viton o-ring seals, evacuated three times with a mechanical pump to an absolute pressure of 9.9 kPa and backfilled with oxygen-gettered (less than 0.1 ppb oxygen) argon gas (model OG-120 furnace with titanium getter, Oxy-gon Industries, Epsom, NH and 99.999% ultra-high purity argon, Airgas, Atlanta, GA). A multi-step heating schedule was implemented, consisting of heating under flowing argon gas at a rate of 0.5°C/min. to 160°C and holding for 4 hours followed by heating at 2.5°C/min. to

800°C, 2°C/min. to 1100°C, and 1.5°C/min. to 1450°C and holding for 4 hours, to facilitate AAc binder removal and partial sintering of WC particles respectively.

A well-mixed blend of WC/rice starch was achieved by mixing WC powder with 2.5 wt. % anhydrous rice starch (MP Biomedicals, Solon, OH) using a high-energy shaker (Red Devil Equipment, Plymouth, MN). WC/rice starch mixtures were packed into a stainless steel die (57 mm diameter) and uniaxially cold pressed to a peak pressure of 35 MPa to form billets of 35 mm height (corresponding to a green density of 7.13 g/cm^3). A multi-step heating schedule was implemented, consisting of heating under flowing oxygen-gettered argon gas at a rate of 0.5°C/min. to 250°C and holding for 6 hours followed by heating at 2°C/min. to 1100°C and 1.5°C/min. to 1450°C and holding for 4 hours, to facilitate rice starch binder removal and partial sintering of WC particles respectively (after which, exhibiting a density of 7.40 g/cm^3, a modest increase with respect to the green density). Upon decomposition of the rice starch in flowing argon atmosphere, up to 15 wt. % (relative to the starch additions) residual carbon remains within the pore volume. Selective oxidation of this carbon residue was performed by subsequent heating in a 100 mL/min. flowing gas mixture of 90 vol. % carbon monoxide/10 vol. % carbon dioxide at 1000°C for 12 hours.

After binder removal and partial sintering, WC billets were mounted onto graphite plates using a water soluble adhesive (Aremco Products, Valley Cottage, NY) and shaped using a CNC milling machine (Flashcut CNC, Deerfield, IL). The CNC machine was operated using toolpaths generated by DeskProto software interface (Delft Spline Systems, Utrecht, Netherlands) taking technical drawings from Solidworks (Dassault Systems, Concord, MA) as input.

1.3.2. 3-D Printing

Porous preforms were prepared by use of a commercially available 3-D printer (Z-Corp, Burlington, MA) adapted for printing of WC powder. The preform was built layer-by-layer by alternating repeated selected area deposition of an aqueous 2.5 wt. % polyethyleneimine/0.5 wt. % glycerol binder solution (both chemicals obtained in 99% purity from Polysciences, Warrington, PA) onto a loosely packed bed of WC powder followed by free-form rolling of approximately 0.1 mm thick layer of WC powder atop the bed. A computer interfaced with the printer controlled locations of binder deposition using technical drawings produced in Solidworks.

An area of the powder bed containing the 3-D printed part, and at least an additional two inches of material surrounding the part, was removed and placed in an oven at 150°C for 1 hour to crosslink the binder (after which, the green density was measured to be 5.10 g/cm^3). With the polymerized binder, sufficient green strength was developed to allow for removal of unbound powder. A multi-step heating schedule was implemented, consisting of heating at a rate of 5°C/min. to 400°C and holding for 2 hours followed by heating at 5°C/min. to 1100°C and 2°C/min. to 1400°C and holding for 2 hours, to facilitate binder removal and partial sintering of WC particles respectively (corresponding to a bulk density of 5.20 g/cm^3). Subsequent heating in a graphite furnace (Oxy-gon Industries, Epsom, NH) under flowing oxygen-gettered argon gas and holding at 2100°C for 4 hours was conducted for additional densification of the printed preforms (corresponding to a final bulk density of 6.63 g/cm^3).

1.3.3. DCP Processing of Preforms

W/ZrC-bearing composites were fabricated by pressureless infiltration and reaction of WC preforms via immersion in a Zr-Cu liquid between 1100-1300°C followed by removal from the melt and light surface polishing to remove excess adhered solidified metal. The large difference in relative hardness of the solidified metal and the ZrC/W-bearing composite allowed for selective removal of the adhered solidified metal without measurable abrasion of the underlying part.

The Zr-bearing melt of congruently melting composition Zr_2Cu was made via arc melting (model 5BJ, Centorr Vacuum Industries, Nashua, NH) within a water-cooled copper hearth under flowing O_2-gettered argon gas using starting materials of Zr ingots (99.9% purity, nominally 5 cm diameter x 1.5 cm thick, Zirconium Research, Philomath, OR) and Cu ingots (99.9% purity, 2.5 cm x 1.5 cm x 0.95 cm, McMaster-Carr, Atlanta, GA). The melt pool was homogenized by repeated melt stirring under the arc followed by mechanical flipping upon solidification for a total of six iterations.

Pressureless infiltration was conducted in a custom vertically-oriented SiC-element resistance furnace equipped with an elevator platform and low-RPM motor that controls the movement of a steel rod to which was attached a graphite bucket containing a part to be immersed. This arrangement is depicted below in Figure 4:

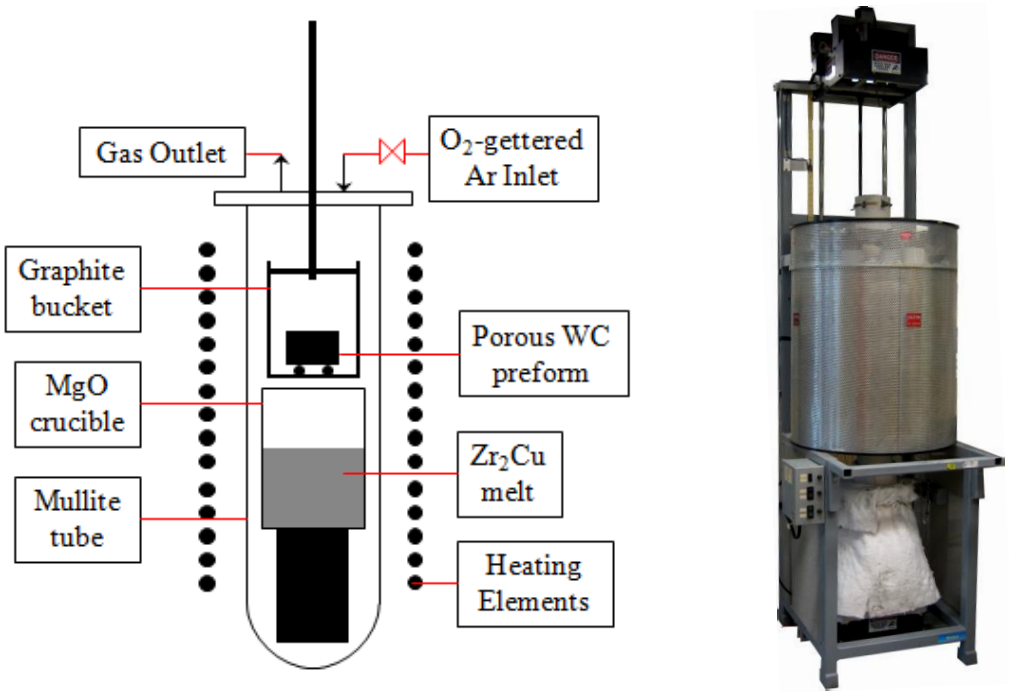

Figure 4: Reactive infiltration apparatus. (left) Schematic view of interior, (right) Exterior view.

A mullite process tube and aluminum end cap with silicone gaskets were used to maintain an inert oxygen-gettered argon atmosphere to prevent oxidation of the Zr-bearing melt. A calibrated K-type thermocouple (Omega Engineering, Stamford, CT) was used to measure the internal temperature near the melt-containing MgO crucible (99.4% purity, 12 cm internal diameter x 20 cm internal height, Ozark Technical Ceramics, Webb City, MO). The temperature was found to vary by +/- 5°C from calibrated set points at 1100°C and 1300°C between the crucible bottom and a position 20 cm above the crucible bottom. Once the furnace temperature reached thermal equilibrium at the infiltration temperature (1100°C), the graphite bucket with a porous WC preform was lowered into the melt and maintained for a time sufficient for complete infiltration and a small amount of reaction (30 min.). The part was then raised above the melt (the infiltrated liquid remained within the preform pore volume by capillary forces) and the temperature was increased to

1300°C for 2 hours to induce faster reaction. Upon removal from the bucket, the infiltrated and reacted part was polished using alumina abrasives to remove surface excess metal resulting from extrusion of the Zr-depleted, Cu-rich liquid out from the closing preform pore volume.

1.3.4. Characterization

Microstructural morphology and phase identification of starting materials, sintered preforms, and DCP processed composites were conducted using a field emission scanning electron microscope (LEO 1530, Carl Zeiss, Cambridge, UK) equipped with backscattered (BSE) and secondary electron (SE) detectors and an energy dispersive x-ray spectrometer (EDS) (INCA, Oxford Instruments, Bucks, UK), and an x-ray diffractometer (XRD) (X'Pert Alpha-1 Diffractometer, PANalytical, Almelo, The Netherlands) equipped with monochromator using Cu Kα1 radiation. Thermogravimetric analysis (TGA) was conducted using an analytical thermobalance (STA 449C, Netzsch Instruments North America, LLC, Burlington MA).

Quantification of composite phase contents was performed using measurements of weight, dimension and density via analytical balance, digital caliper, and Archimedes water displacement measurements, respectively, coupled with quantitative peak-area-ratio XRD analysis. For this purpose, a calibration curve was developed using standardized mixtures of W (99.8% purity, >40 μm diameter, Buffalo Tungsten, Depew, NY), ZrC (99.8% purity, <150 μm diameter, Atlantic Equipment Engineers, Bergenfield, NJ) and WC powders representative of various extents of reaction according to the stoichiometry of reaction (1.1) (i.e. – the total number of moles of tungsten and carbon were individually held constant, while the number of moles of zirconium was

incrementally increased). Weighed powder mixtures were blended under acetone in mortar and pestle, suspended in petroleum jelly, and spread as thin layers onto a single crystal silicon substrate for XRD spectrum collection using a fixed measurement program. Peak areas were evaluated using peak profile fitting algorithms found in X'Pert HighScore Pro software (PANalytical, Almelo, The Netherlands) which adequately accounted for background level and peak overlap effects. The average peak area ratio of W(110):WC(100), obtained from 9 independent measurements at each composition, was plotted versus the molar extent of reaction corresponding to each composition to generate a calibration curve that was used as a basis for comparison for subsequent XRD analysis of DCP processed composites.

1.4. *Results*

As seen in the Cu-Zr phase diagram (Figure 5), narrow two-phase fields exist between line compounds, especially on the Cu-rich portion of the diagram:

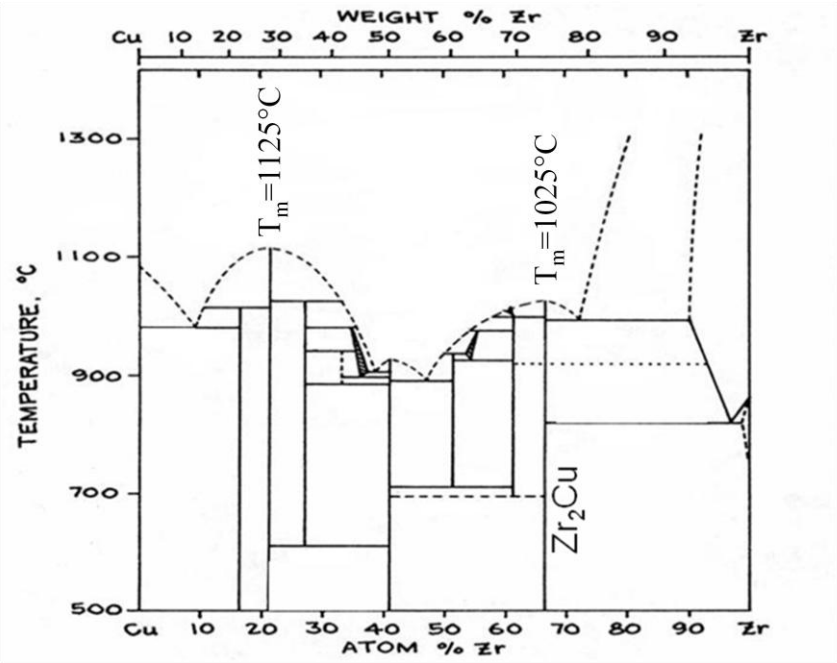

Figure 5: Cu-Zr phase diagram[32]

Therefore, a small deviation in overall composition can result in a large amount of secondary phase formation. Arc-melting has proven to effectively homogenize weighed mixtures of Cu and Zr ingots, as evidenced by XRD analyses of Zr_2Cu (Figure 6) and $Zr_{14}Cu_{51}$ (Figure 7) compositions:

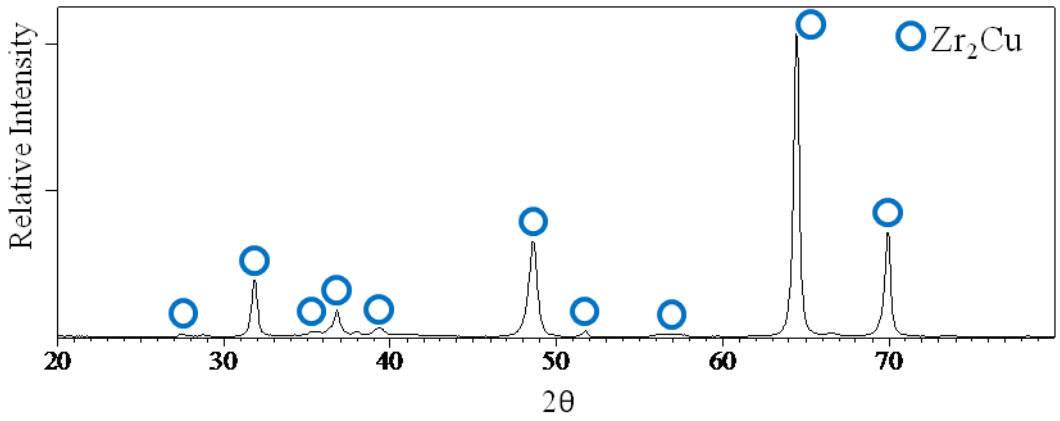

Figure 6: XRD analysis of arc-melted Zr_2Cu (PDF Card No. 04-004-2397)

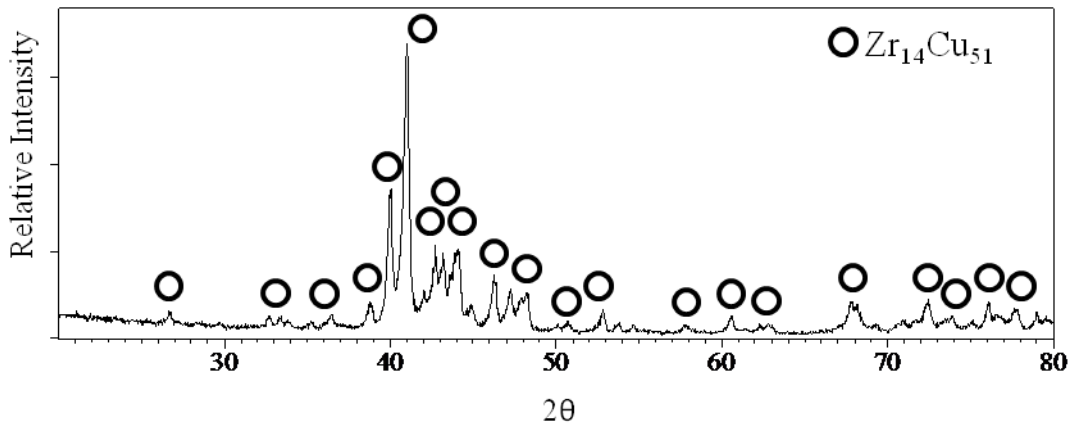

Figure 7: XRD analysis of arc-melted $Zr_{14}Cu_{51}$ (PDF Card No. 42-1185) (all peaks corresponded to $Zr_{14}Cu_{51}$ – only major peaks labeled for clarity)

The phase purity of the infiltrating alloy assures congruent melting, preventing premature off-stoichiometric liquid formation and solid phase separation.

Optimal heating conditions for removal of rice starch (Figure 8) and ammonium acetate (Figure 9) binders were evaluated via TGA at a heating rate of 10 K/min. under flowing oxygen-gettered argon:

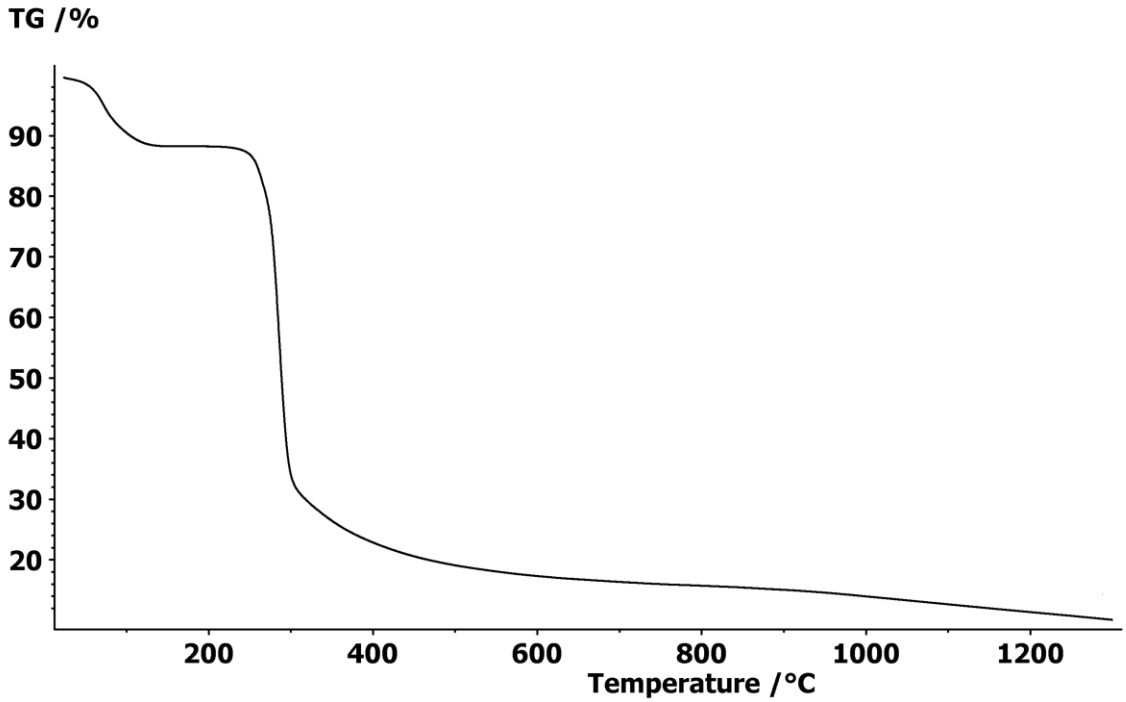

Figure 8: Weight loss of rice starch binder under flowing oxygen-gettered argon heated at 10 K/min.

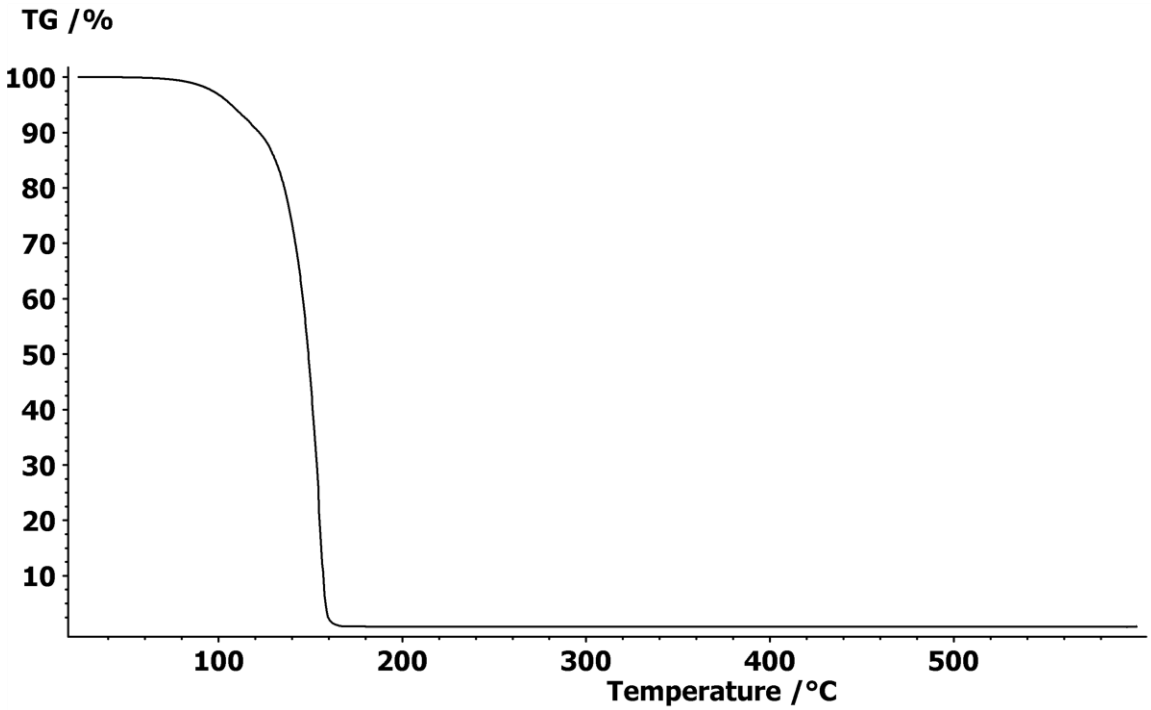

Figure 9: Weight loss of ammonium acetate under flowing oxygen-gettered argon heated at 10 K/min.

Thermal decomposition of rice starch under an argon atmosphere leaves in excess of 10 wt. % carbon residue while ammonium acetate is completely decomposed. Further analysis of the tail of the weight loss curve in Figure 8 indicates that the rice starch itself appears to contain some slowly-decomposing material which continues even to high temperature. Additional investigation into the possible presence of inorganic material naturally occurring in the rice starch may be warranted.

Selective oxidation of the carbon residue from rice starch thermal decomposition proceeds faster at 1000°C than at 900°C, as evidenced by static thermogravimetric weight loss measurements (Figure 10):

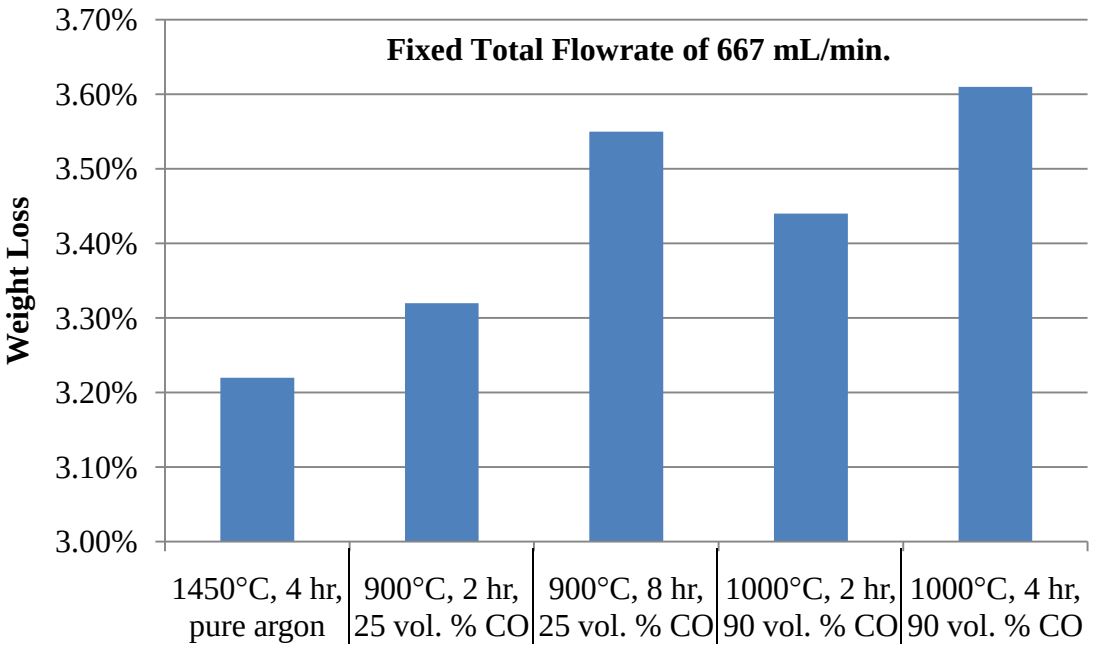

Figure 10: Weight loss measurements from selective oxidation of carbon residue in CO/CO_2 atmospheres in WC preforms using 3.60 wt. % rice starch binder

For WC preforms having 3.60 wt. % rice starch binder, heating in pure argon at 1450°C for 4 hours leaves behind a carbon residue of approximately 10.8 wt. % of the initial rice starch weight. Subsequent heating in CO/CO_2 atmospheres (whose composition is chosen on the basis of thermodynamic calculations, discussed in section 1.5.3) induces selective oxidation of this carbon residue without oxidation of the WC in the preform. Heat treatment times in excess of 8 hours at 900°C would have been required to fully remove all residue from WC preform pellets (46.5 +/- 0.5% relative density on the basis of WC, nominally 12.7 mm diameter x 5.2 mm height) while times less than 4 hours at 1000°C were required.

XRD analyses of WC preforms were conducted after binder burnout (and selective oxidation, in the case of rice starch binder being used) and partial sintering to assess the presence of contaminants and the potential oxidation of WC. Figure 11 and

Figure 12 show XRD spectra for cross sections of partially sintered CNC machined and 3-D printed WC preforms made using rice starch and PEI/glycerol binders, respectively:

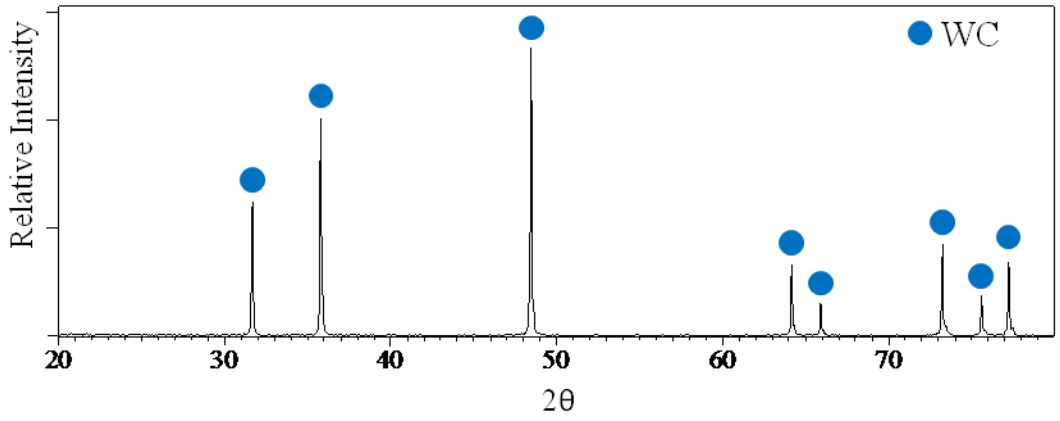

Figure 11: XRD analysis of 3-D printed WC preform after firing in oxygen-gettered argon at 1450°C, 4h (PDF Card No. 25-1047)

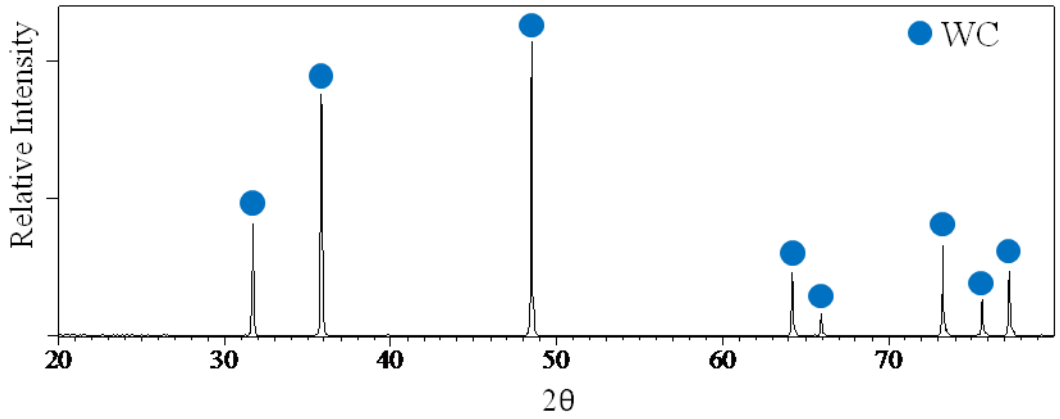

Figure 12: XRD analysis of CNC machined WC preform after firing in oxygen-gettered argon at 1450°C, 4h and selective oxidation in 9:1 vol. ratio CO/CO_2 atmosphere at 1000°C, 4h (PDF Card No. 25-1047)

XRD spectra confirmed that WC did not exhibit detectable oxidation under conditions used for binder burnout and sintering, and that there were no detectable secondary phases in the preform.

Sintered WC preforms in the shapes of nozzles, crucibles and cones were fabricated via CNC machining and subsequently immersed in molten Zr_2Cu to produce W/ZrC-bearing composites, as seen in Figure 13, Figure 14, and Figure 15:

Figure 13: Optical images of a nozzle at various stages of production. (left) CNC machined WC preform; (middle) after DCP infiltration, with excess surface copper and oxidation; (right) after light surface polishing to remove adhered solidified metal.

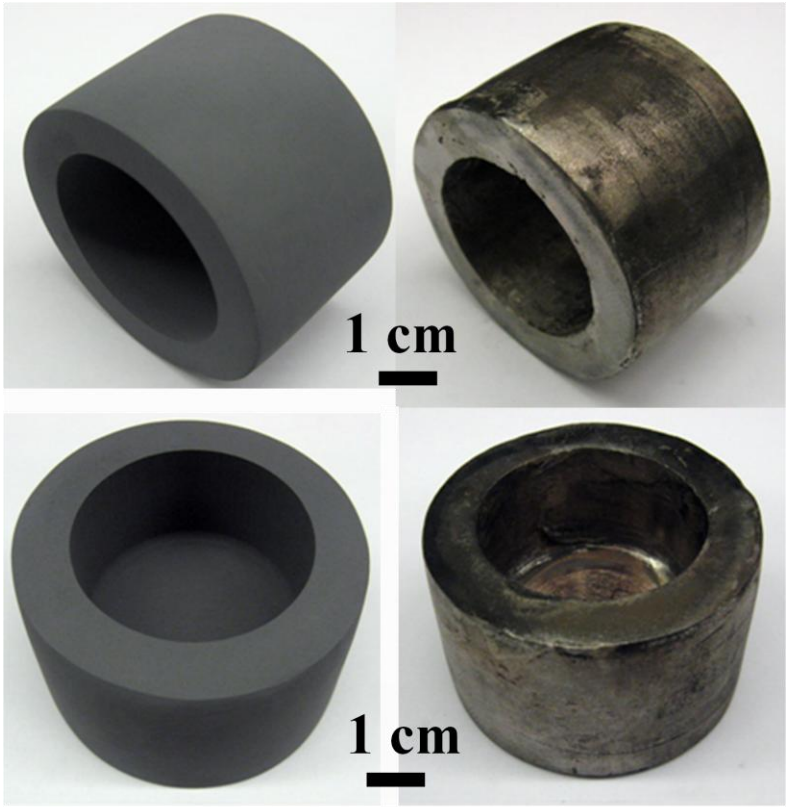

Figure 14: Optical images of a crucible at various stages of production. (left) CNC-machined WC preforms; (right) after DCP infiltration and light surface polishing to remove adhered solidified metal.

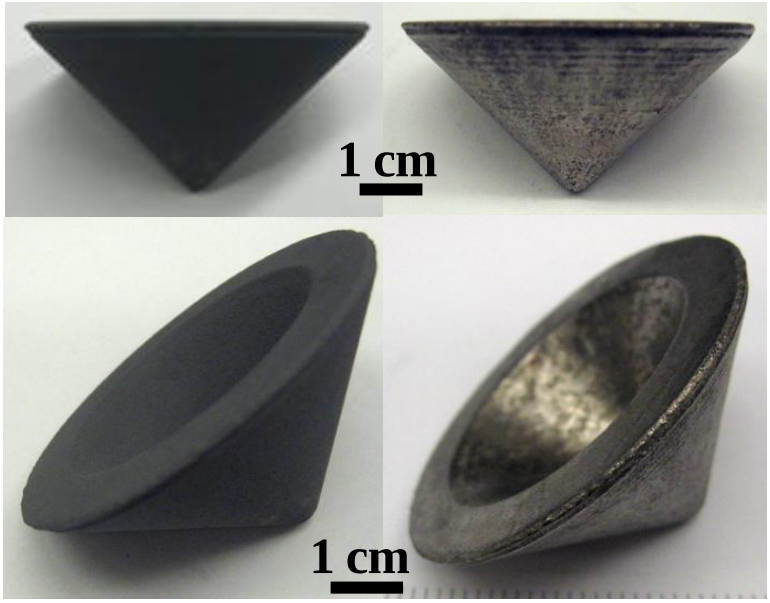

Figure 15: Optical images of a cone at various stages of production. (left) CNC-machined WC preforms; (right) after DCP infiltration and light surface polishing to remove adhered solidified metal.

Surface imperfections in WC preforms as small as 0.1 mm introduced by CNC machining were retained after DCP processing (see surface striations in Figure 13).

Tungsten carbide preforms in the shapes of nozzles were fabricated via 3D printing and subsequently immersed in molten Zr_2Cu to produce W/ZrC-bearing composites, as seen in Figure 16:

Figure 16: Optical images of a nozzle at various stages of production. (left) 3D-Printed WC preform; (middle) after DCP infiltration, with excess surface copper and oxidation; (right) after light surface polishing to remove adhered solidified metal.

Dimension measurements of characteristic geometrical features of the WC preforms and ZrC/W-bearing products shown in Figure 13, Figure 14, Figure 15 and Figure 16 are summarized in Table 2:

Table 2: Dimension measurements of WC preforms and DCP-derived W/ZrC-bearing composites

Geometrical Feature	Average Size in WC Preform [mm]	Average Size in W/ZrC Composite [mm]	% Change
CNC machined nozzle			
OD nozzle exit	50.65 ± 0.09	50.32 ± 0.16	-0.65%
OD nozzle entrance	37.50 ± 0.08	37.23 ± 0.07	-0.72%
Nozzle height	32.13 ± 0.22	32.00 ± 0.30	-0.40%
CNC machined cone			
Bottom diameter	52.40 ± 0.08	51.98 ± 0.15	-0.80%
Cone height	26.03 ± 0.05	25.87 ± 0.07	-0.61%
CNC machined crucible			
Outer diameter	55.62 ± 0.07	55.19 ± 0.05	-0.77%
Inner diameter	36.71 ± 0.08	36.44 ± 0.09	-0.74%
Outer height	35.20 ± 0.07	35.00 ± 0.06	-0.57%
Inner height	24.34 ± 0.06	24.22 ± 0.05	-0.49%
3D printed nozzle			
OD nozzle exit	54.23 ± 0.25	53.90 ± 0.12	-0.61%
OD nozzle entrance	40.34 ± 0.20	40.09 ± 0.13	-0.62%
Nozzle height	34.82 ± 0.15	34.53 ± 0.23	-0.83%

The measurements in Table 2 represent the median and absolute range of values taken from ten measurements of each geometrical feature. All characteristic dimensions of WC preforms were found to decrease slightly upon reactive infiltration.

The phase contents of W/ZrC-bearing composites produced by combination of rapid prototyping techniques with the DCP process were characterized by measurements of weight and dimension change combined with quantitative XRD analysis (Figure 17) to determine the extent of conversion of WC preforms after reactive infiltration.

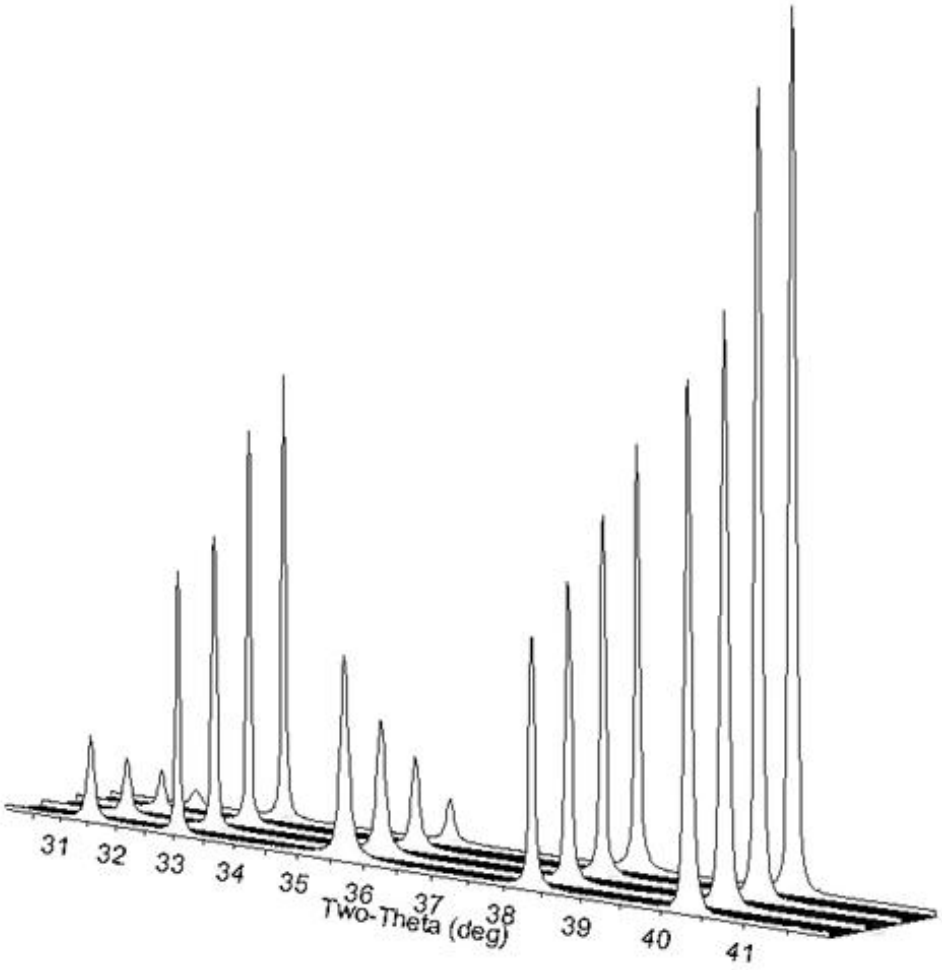

Figure 17: Representative XRD spectra for calibration curve

Figure 17 depicts averaged spectra from nine scans corresponding to (front-to-back) 70, 80, 90, and 95% conversion of WC to W and ZrC. The peaks in the displayed two-theta

range correspond to (left-to-right): WC(001), ZrC(111), WC(100), ZrC(200), W(110). The peak area ratio of the 100% intensity peaks for W(110) and WC(100) was plotted as a function of equivalent extent of conversion (Figure 18):

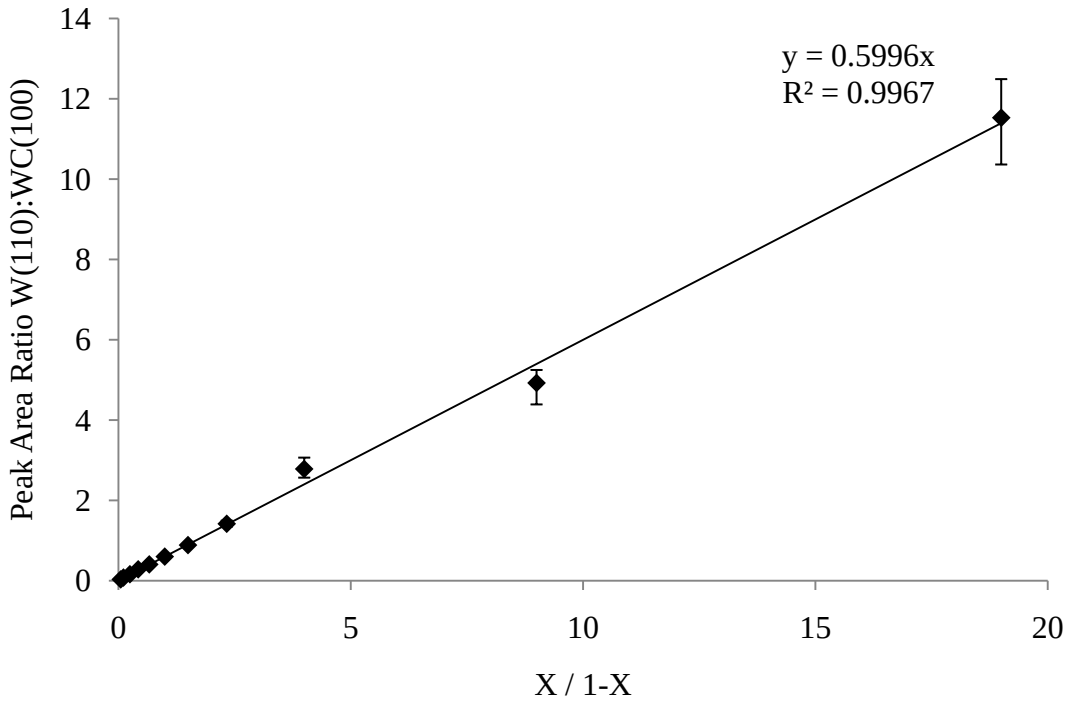

Figure 18: XRD calibration curve

The data was fitted to the equation:

$$H = \frac{KX}{1 - X} \tag{1.6}$$

where *H* is the W:WC peak area ratio, *K* is a fitted parameter (0.5966), and *X* is the extent of reaction (the molar ratio of W:WC being *X*/(1-*X*), assuming these are the only two W-containing phases in the sample and starting with only WC). The extent of reaction was therefore related to the measured W(110):WC(100) peak-area-ratio by the equation:

$$X = \frac{H}{H + K} \tag{1.7}$$

Although it was possible to construct an equivalent curve making use of ZrC(111):WC(100) peak area ratios, the relatively small observed intensities for ZrC diffraction peaks versus W peaks (due to differences in atomic scattering factors) resulted in greater susceptibility to error from profile fitting.

For example, XRD analysis (Figure 19) of a polished cross-section of a 3-D printed and DCP infiltrated W/ZrC-bearing composite exhibited an average W:WC peak area ratio of 12.5:1, corresponding to a molar composition of 20.8:1 W:WC.

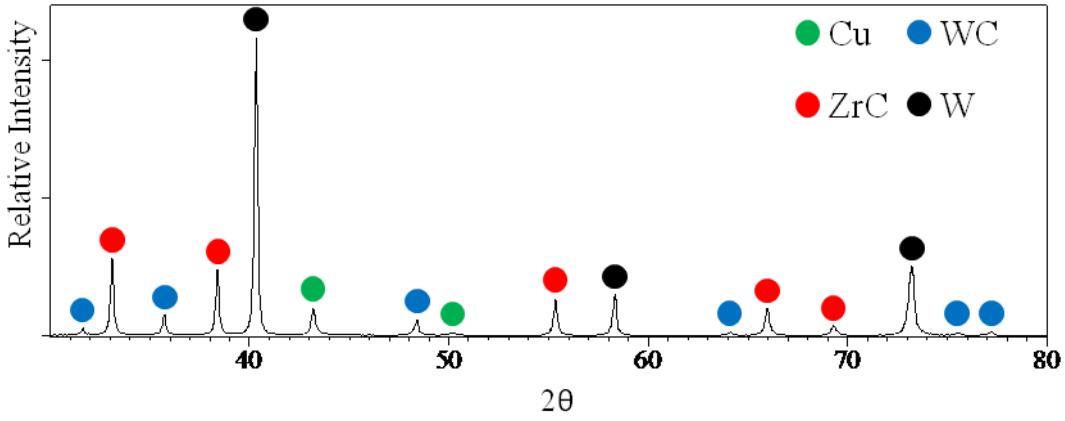

Figure 19: XRD analysis of a cross-section of DCP reacted 3-D printed preform (PDF Card No. for W 04-0806, Cu 08-0836, ZrC 35-0784, WC 25-1047)

Physical property data used for phase content calculations is summarized in Table 3:

Table 3: Selected physical property data for reactants and phases produced via DCP infiltration of Zr-Cu alloys into WC preforms

Phase (JCPDS PDF Card Number[29])		Molar Weight [g/mol]	Density [g/cm^3]	Molar Volume [cm^3/mol]
WC (25-1047)		195.861	15.667	12.502
W (04-0806)		183.850	19.259	9.546
ZrC (35-0784)		103.231	6.633	15.563
Cu (04-0836)		63.546	8.932	7.114
Liquids @ 1100°C	Cu(l)[33]	63.546	7.99	7.96
	Zr_2Cu(l)[37,38]	81.998	6.77	12.11
	$Zr_{14}Cu_{51}$(l)[37,38]	69.507	7.65	9.09

Calculations have been performed to determine the densities and phase contents for composites produced via combination of rapid prototyping and DCP processing (see

Appendix A for sample calculations), and the results are indicated in Table 4, Table 5, and Table 6:

Table 4: Characterization results of CNC machined preform with rich starch binder and resulting DCP-derived ZrC/W-bearing composite

WC Preform ρ [g/cm^3]	W/ZrC Composite ρ [g/cm^3]			W:WC Molar Ratio	Extent of Reaction (Vol. %)
7.25 ± 0.01	10.99 ± 0.05			11.5 ± 0.8	92 ± 1
Solid Phase Contents (Vol. %)				**W/ZrC Composite $\rho_{theo.}$ [g/cm^3]**	
ZrC	**W**	**Cu**	**WC**		
56 ± 6	35 ± 4	5.1 ± 0.6	3.9 ± 0.4	11.5 ± 0.9	

Table 5: Characterization results of CNC machined preform with ammonium acetate binder and resulting DCP-derived ZrC/W-bearing composite

WC Preform ρ [g/cm^3]	W/ZrC Composite ρ [g/cm^3]			W:WC Molar Ratio	Extent of Reaction (Vol. %)
7.47 ± 0.01	11.61 ± 0.05			8.7 ± 0.6	90 ± 1
Solid Phase Contents (Vol. %)				**W/ZrC Composite $\rho_{theo.}$ [g/cm^3]**	
ZrC	**W**	**Cu**	**WC**		
53 ± 6	33 ± 4	9 ± 1	4.9 ± 0.5	11.4 ± 1.2	

Table 6: Characterization results of 3-D printed preform with PEI/glycerol binder and resulting DCP-derived ZrC/W-bearing composite

WC Preform ρ [g/cm^3]	W/ZrC Composite ρ [g/cm^3]			W:WC Molar Ratio	Extent of Reaction (Vol. %)
6.63 ± 0.01	10.58 ± 0.05			21 ± 2	95 ± 1
Solid Phase Contents (Vol. %)				**W/ZrC Composite $\rho_{theo.}$ [g/cm^3]**	
ZrC	**W**	**Cu**	**WC**		
55 ± 6	33 ± 4	10 ± 1	2.1 ± 0.2	11.2 ± 1.2	

The calculated phase contents (including volume percent porosity) of DCP-derived ZrC/W-bearing composites summarized in Table 4, Table 5 and Table 6 for WC preforms having starting relative densities in the range 42.3-47.7% varied in the following ranges: 51-54 vol. % ZrC, 32-33 vol. % W, 5-9 vol. % Cu, 2-5 vol. % WC, and -1-7 vol. % porosity. It is notable that the ranges of phase contents do not show a strong dependence

on the method of preform fabrication, as the phase contents for 3-D printed preforms are comparable to those found in CNC machined preforms using rice starch or ammonium acetate as binders.

Dimensional analyses combined with phase content quantification indicated that the DCP process is capable of producing near-fully dense, near-net shape and near net-dimension parts. Surface features in addition to bulk shape are also capable of being preserved. Further, microstructural features of composites produced via the DCP process retain characteristics of the WC preform. For example, complex shaped WC preforms fabricated by CNC machining of uniaxially pressed and sintered billets had microstructures consisting of a uniform distribution of WC particles and pores, while DCP processed counterparts had microstructures primarily consisting of a uniform distribution of W particles surrounded by a continuous ZrC matrix. Microstructures of DCP processed WC preforms produced by CNC machining and 3-D printing characterized by BSE images and EDS spectra are shown in Figure 20, Figure 21, and Figure 22:

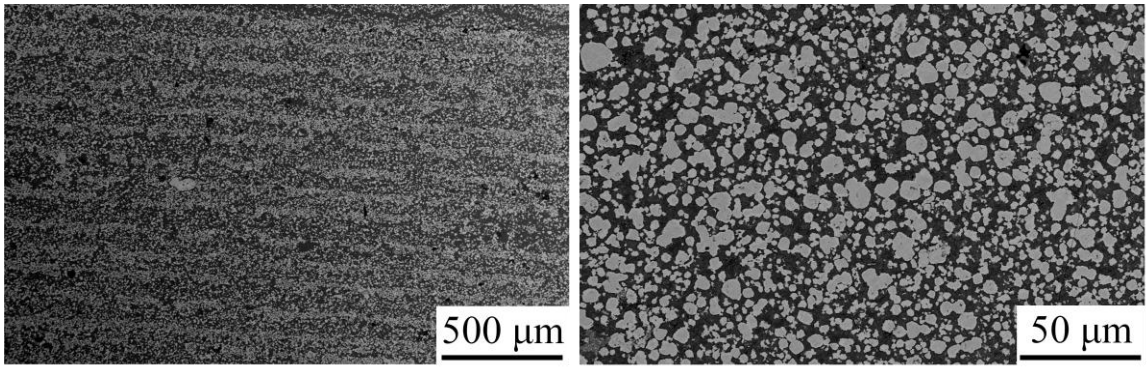

Figure 20: BSE images illustrating DCP-derived microstructures of (left) 3-D printed WC preform and (right) CNC machined uniaxially cold pressed WC preform

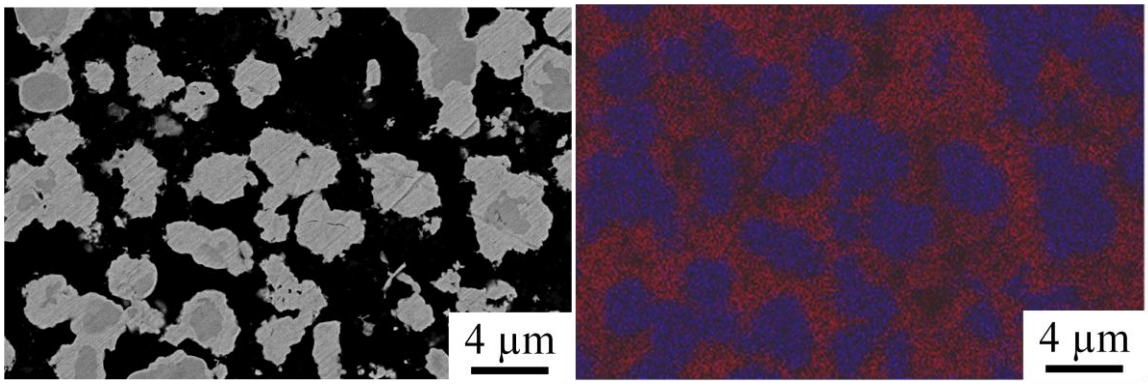

Figure 21: Characterization of reactively infiltrated CNC machined preform; (left) BSE image and (right) EDS element mapping (tungsten in blue, zirconium in red)

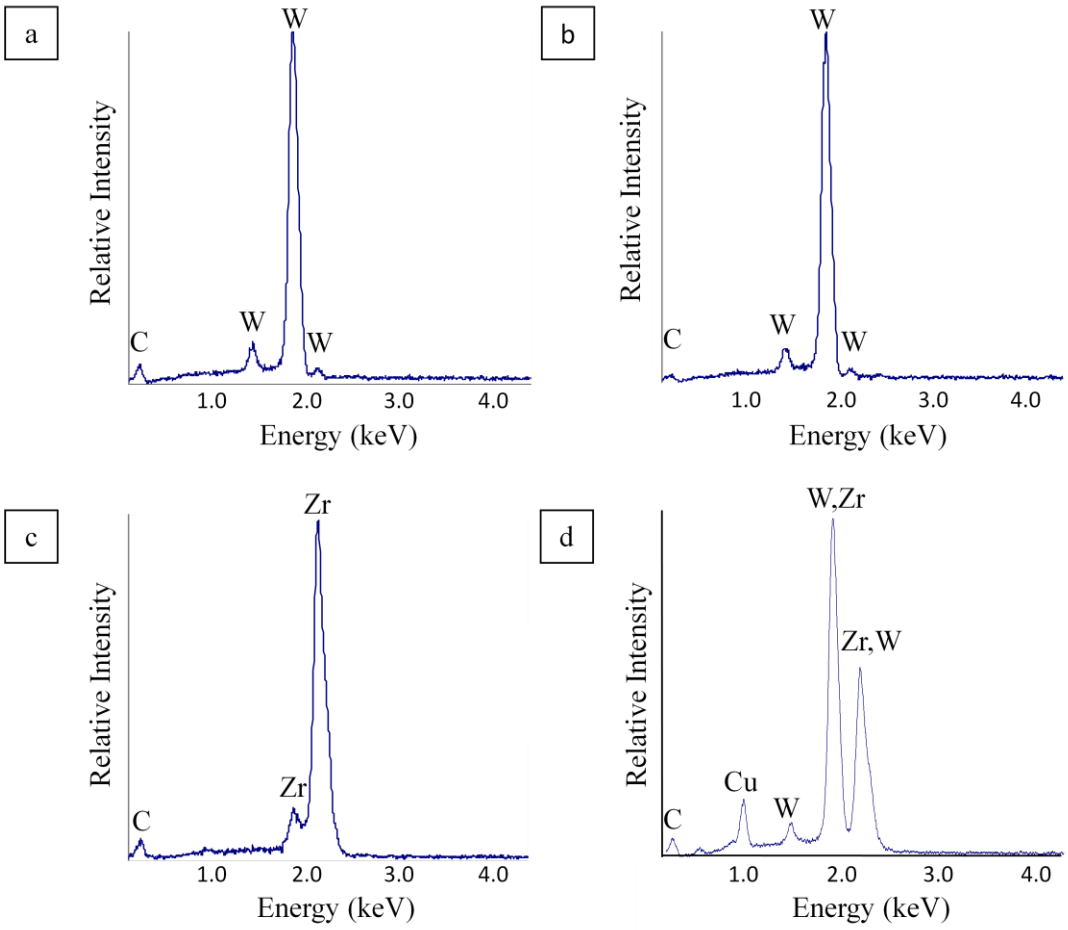

Figure 22: Representative EDS spectra of a reactively infiltrated preform (produced via CNC machining of uniaxially cold pressed and sintered billet) shown in Figure 20. These spectra correspond to (a) the dark (WC) core within some of the particles, (b) the bright (W) cladding around the dark (WC) core in some particles, (c) the dark (ZrC) matrix phase and (d) over a large (550 µm x 360 µm) area.

Based upon observations of partially reacted particles (Figure 22a-c), the mechanism for microstructural retainment was thought to be the formation of coherent, conformal product layers of W around WC and ZrC around W. The presence of minor peaks for copper in EDS spectra taken over large cross-sectional areas (Figure 22d) indicating the presence of minor amounts of copper and the observation of minor amounts of porosity are in qualitative agreement with the calculated phase contents for DCP-derived ZrC/W-bearing composites. Microstructural features preserved during DCP processing range from several microns (individual particles) to several hundreds of microns (lamination layers in 3-D printed preforms).

1.5. *Discussion*

1.5.1. Reactive Infiltration Modeling

Adoption of composites produced via the DCP process for advanced engineering applications requires predictive quantification of phase contents for design optimization on a per-application basis. Composite phase contents can be modeled to a first approximation by the stoichiometry of reaction and assuming uniform extent of reaction without impediment throughout the infiltrated body up to completion.

The phase contents of DCP processed composites can be evaluated in the following manner. Assume that the preform consists initially solely of mixtures of WC and ZrC such that:

$$U_{total,i} = U_{WC,i} + U_{ZrC,i} + U_{pore,i} \tag{1.8}$$

where $U_{k,i}$ is the initial volume of phase *k*, and that the final phase mixture present in the DCP processed composite consists of W, ZrC, WC, and Cu such that:

$$U_{total,f} = U_W + U_{ZrC,f} + U_{WC,f} + U_{Cu} + U_{pore,f} \tag{1.9}$$

with $U_{total,f}$ related to $U_{total,i}$ by:

$$U_{total,f} = (1-\zeta)^3 U_{total,i} \tag{1.10}$$

where ζ is the average linear fractional dimension change of the part upon reactive infiltration, assuming isotropic shrinkage. The volume fraction, V_j, of any given phase *j* is given by:

$$V_j = \frac{U_j}{U_{total}} \tag{1.11}$$

Treating pore volume fraction as a phase allows for V_{total} to take a value of unity. Measurement of preform weight and bulk density (ρ_i) allows for calculation of $V_{WC,i}$ and $V_{pore,i}$. Measurement of the extent of reaction, *X*, as defined by the volume percent WC reacted, by quantitative XRD analysis and of the final bulk density (ρ_f) of the DCP processed composite allows for calculation of the volume fractions of each phase. The remaining volume fraction of WC is given by:

$$V_{WC,f} = (1-X)V_{WC,i} \tag{1.12}$$

Given the stoichiometry of reaction (1.1), each mole of WC reacted generates one mole of W and one mole of ZrC, corresponding to W and WC volume fractions given by:

$$V_W = XV_{WC,i}\left(\frac{\cancel{V}_W}{\cancel{V}_{WC}}\right) \tag{1.13}$$

$$V_{ZrC,f} = XV_{WC,i}\left(\frac{\cancel{V}_{ZrC}}{\cancel{V}_{WC}}\right) + V_{ZrC,i} \tag{1.14}$$

where $\cancel{V}_j$ is the molar volume phase *j* (subscripts *i* and *f* refer to initial and final, respectively).

Measurement of the final bulk density of the composite allows for calculation of the remaining solid phase Cu via mass balance:

$$\rho_f = V_{Cu}(\rho_{Cu}) + V_{WC,f}(\rho_{WC}) + V_W(\rho_W) + V_{ZrC,f}(\rho_{ZrC}) \tag{1.15}$$

where ρ_j is the density of phase j. Upon re-arrangement, the volume fraction of copper is given by:

$$V_{Cu} = \frac{\rho_f}{\rho_{Cu}} - V_{WC,f}\left(\frac{\rho_{WC}}{\rho_{Cu}}\right) - V_W\left(\frac{\rho_W}{\rho_{Cu}}\right) - V_{ZrC,f}\left(\frac{\rho_{ZrC}}{\rho_{Cu}}\right) \tag{1.16}$$

Lastly, the pore volume fraction is found simply by:

$$V_{pore,f} = 1 - V_{WC,f} - V_W - V_{ZrC,f} - V_{Cu} \tag{1.17}$$

The solid volume fraction, V^s_j of each phase in the final composite, is calculated as:

$$V_j^s = \frac{V_j}{1 - V_{pore,f}} \tag{1.18}$$

The theoretical density of the composite if consolidated to 100% relative density is:

$$\rho_{theo} = \rho_{WC}V_{WC,f} + \rho_W V_W + \rho_{ZrC}V_{ZrC,f} + \rho_{Cu}V_{Cu} \tag{1.19}$$

Consider, for example, preforms consisting of mixtures of WC and ZrC subjected to reactive infiltration by Zr-Cu liquids. The calculated phase contents and bulk densities of infiltrated WC/ZrC preforms have been plotted as functions of preform composition and preform pore volume fraction (Figure 23-Figure 27):

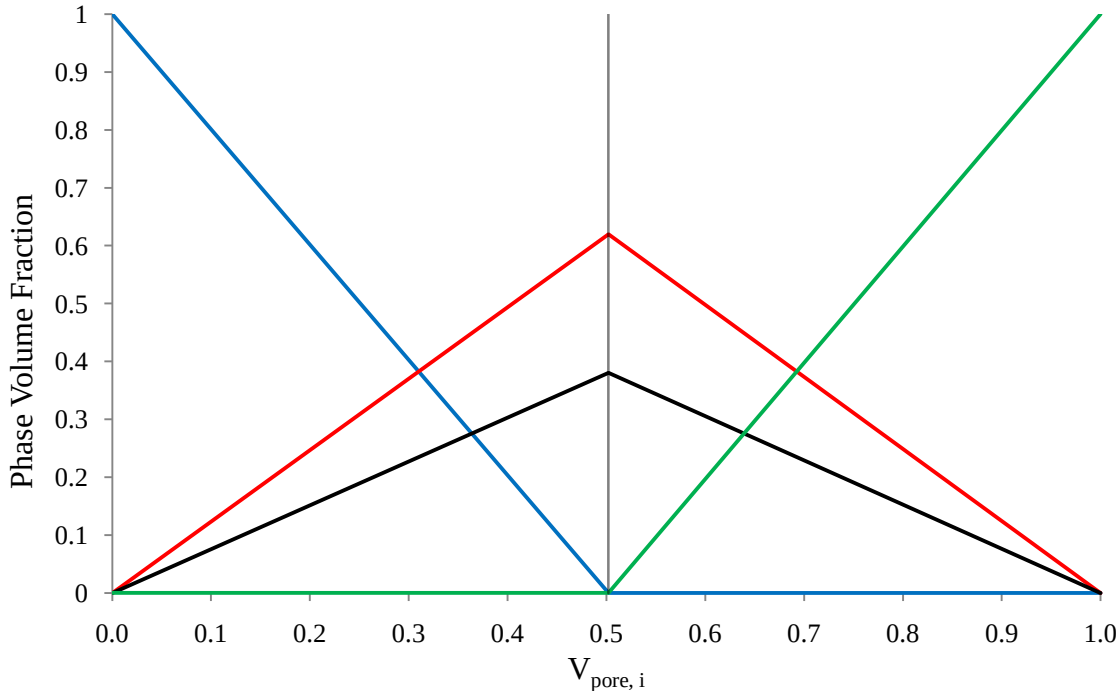

Figure 23: Calculated phase contents of 100 vol. % WC preform after reactive infiltration with Zr-bearing fluids, assuming no change in external dimensions and that pore choke off does not occur (ZrC (red), W (black), WC (blue) and Cu (green)).

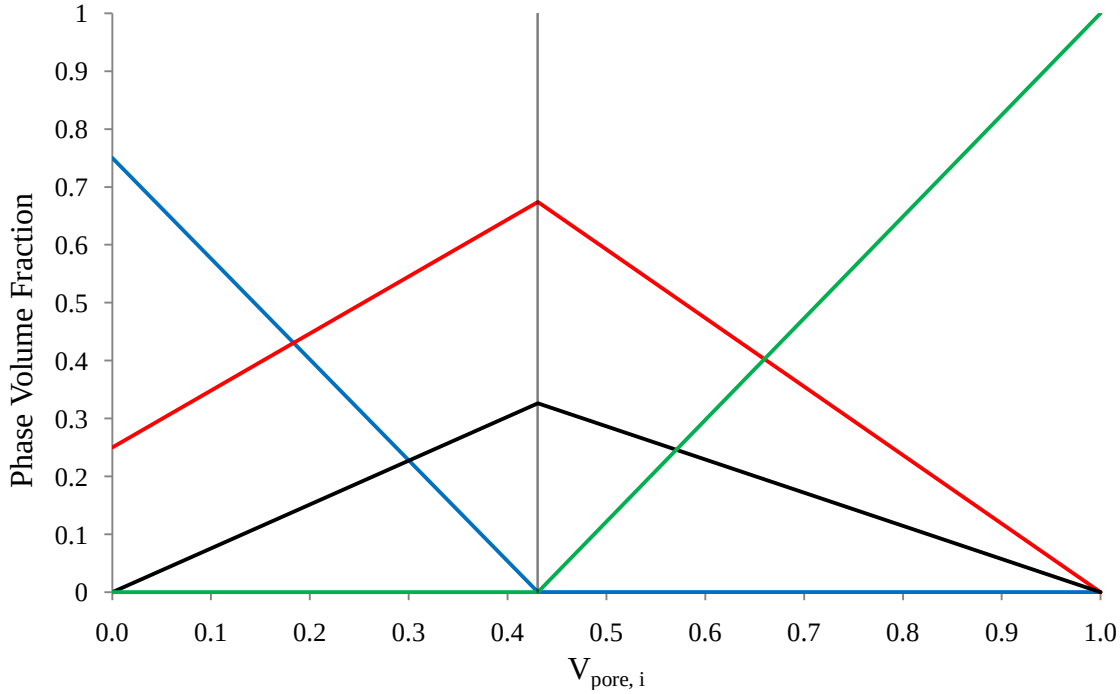

Figure 24: Calculated phase contents of 75 vol. % WC/25 vol.% ZrC preform after reactive infiltration with Zr-bearing fluids, assuming no change in external dimensions and that pore choke off does not occur (ZrC (red), W (black), WC (blue) and Cu (green)).

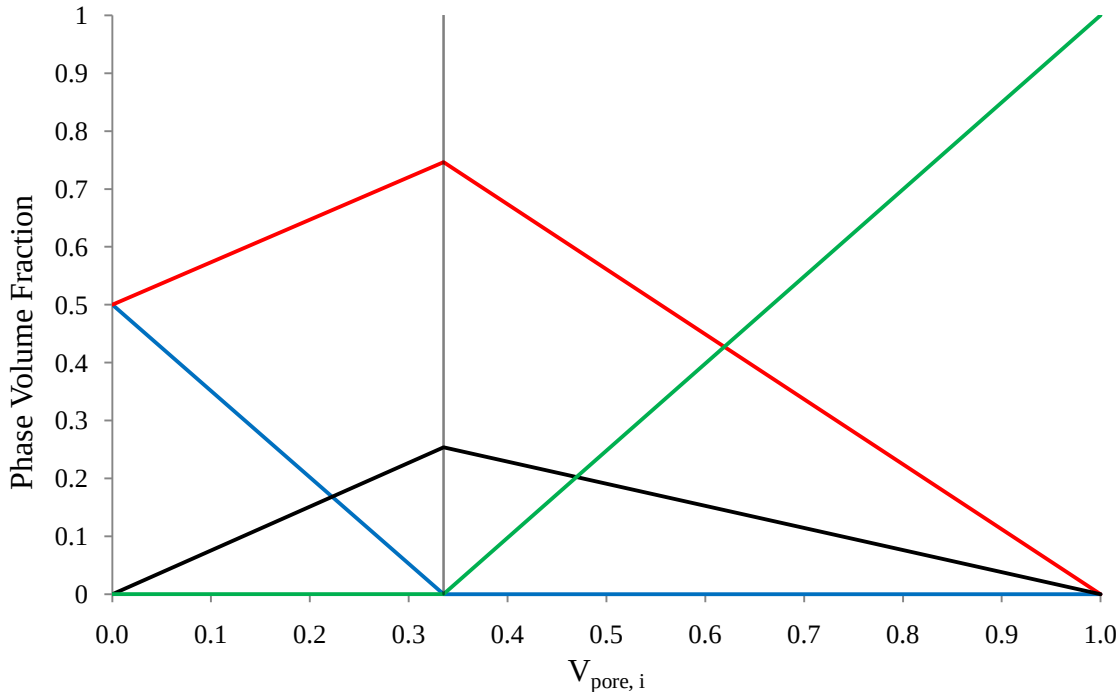

Figure 25: Calculated phase contents of 50 vol. % WC/50 vol.% ZrC preform after reactive infiltration with Zr-bearing fluids, assuming no change in external dimensions and that pore choke off does not occur (ZrC (red), W (black), WC (blue) and Cu (green)).

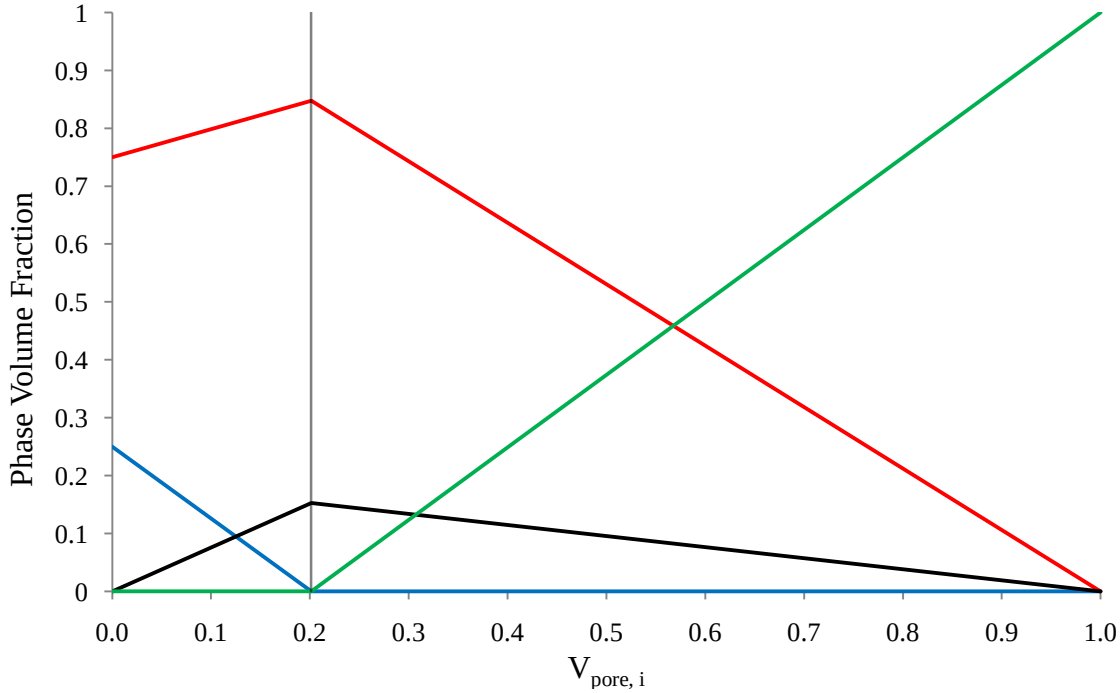

Figure 26: Calculated phase contents of 25 vol. % WC/75 vol.% ZrC preform after reactive infiltration with Zr-bearing fluids, assuming no change in external dimensions and that pore choke off does not occur (ZrC (red), W (black), WC (blue) and Cu (green)).

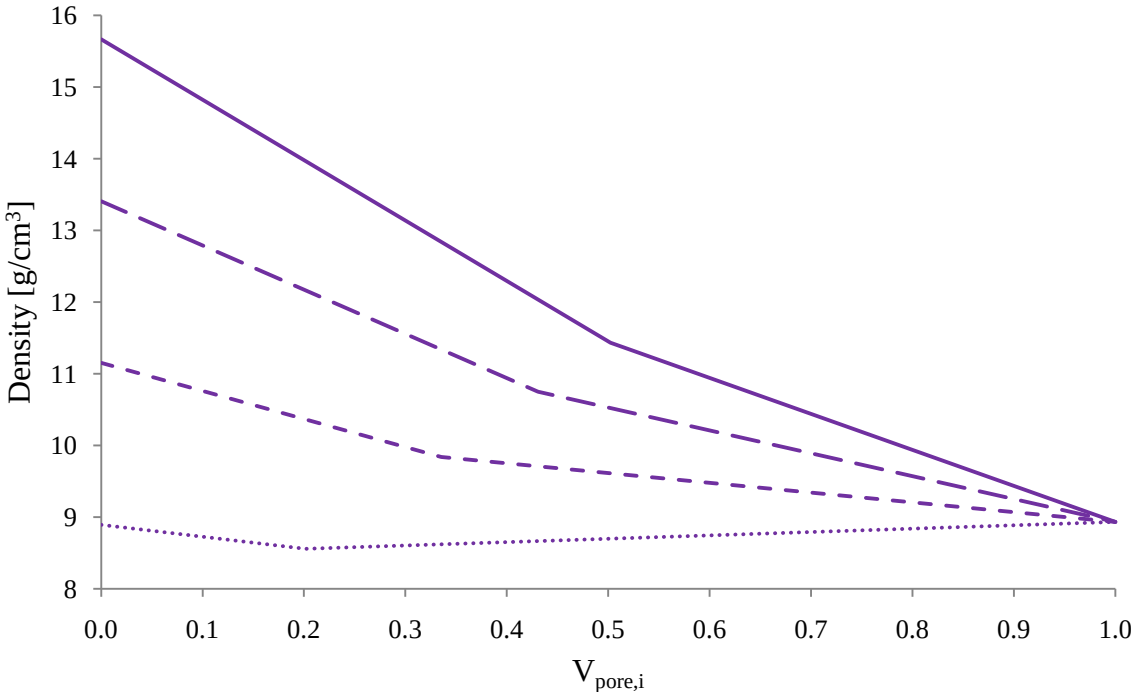

Figure 27: Calculated densities of WC/ZrC preforms after infiltration with Zr-bearing fluids. Solid lines correspond to 100 vol. % WC preforms, long dashed lines to 3:1 WC:ZrC ratio, short dashed lines to 1:1 WC:ZrC ratio, and dotted lines to 1:3 WC:ZrC ratio.

Preforms having compositions rich in ZrC can produce composites with decreased W content, resulting in lower part densities. For a given starting composition consisting of WC and ZrC, the preform pore volume fraction at which extent of reaction is maximized and residual copper content is minimized is calculated from equation (1.3). For values of f = 1, 0.75, 0.5 and 0.25, Ψ = 50.2%, 43.0%, 33.5% and 20.1%, respectively (shown as grey vertical lines in Figure 23-Figure 26). As the volume fraction of ZrC in the WC/ZrC preform mixture increases, so too does the relative target density necessary for its pore volume to become completely filled by reaction products upon complete reaction. Preforms having solids volume fractions above the corresponding critical target density will retain residual unreacted WC (and perhaps, depending on the competitive kinetics of infiltration versus reaction, uninfiltrated regions due to premature choke-off), while those below the critical value should be able to fully react all WC and have remaining pore

volume assumed to be filled by Cu (i.e., Zr-Cu liquid near fully depleted of Zr by reaction).

It is important to note that reactive infiltration processes require a continuous network of open pores to supply new reactant. As the relative density increases, portions of the pore network begin to choke-off until, at a critical threshold, nearly all pore interconnectivity disappears. This choke-off threshold is strongly dependant on microstructural features such as particle geometry and particle size distribution[34]. Typical pore choke-off values observed experimentally for three-dimensional random particulate and fibrous microstructures having tortuous pore networks (known as capillary percolation) fall in the range of 10-20% pore volume fraction[34,35,36]. By contrast, perfectly aligned microstructures should avoid pore choke-off almost entirely, owing to the one-dimensional symmetry of the open pore network.

The amount of reaction occurring after pore choke-off can be reactant-limited if the molar quantity of liquid reactant remaining in the pores (e.g., Zr) is less than the molar quantity of solid reactant remaining in the preform (e.g., WC). It can therefore be advantageous to maximize the reactant concentration in the infiltrating fluid in order to maximize the extent of reaction occurring after pore choke-off. For the case where infiltration is much faster than reaction, one can assume the entire pore volume to be filled by the bulk composition of the infiltrating liquid. A value of interest is the pore volume fraction at which there are equal numbers of moles of liquid reactant in the pores and solid reactant remaining in the preform. At this point, infiltration is no longer required for complete reaction and reaction kinetics can be increased without causing gradients in the extent of reaction in the body.

In the following discussions, three simplifying assumptions are made: first, that the external dimensions of the DCP-derived composite are unchanging; second, that the infiltration rate is much faster than the reaction rate, such that the composition of the liquid in the pores remains constant throughout the process; and, third, that preform consists initially of pure WC.

Then, the total extent of reaction, *X*, can be modeled as the sum of the extents of reaction occurring during infiltration and occurring after infiltration stops (either due to pore choke-off or removal of the preform from the melt), such that:

$$X = \Gamma + (1 - \Gamma)(\beta|_{X=\Gamma}) \tag{1.20}$$

where Γ is the extent of reaction occurring during continuous re-supply of reactant and $\beta|_{X=\Gamma}$ is the instantaneous molar ratio of liquid {Zr} to the unreacted solid WC within the infiltrated body after extent of reaction Γ. The second term on the right hand side of equation (1.20) represents the extent of reaction that can occur after the re-supply of reactant halts.

β is defined by the following expression:

$$\beta = \left(\frac{V_{\{Zr\},X}}{V_{WC,X}}\right) \Big/ \left(\frac{\bar{V}_{\{Zr\}}}{\bar{V}_{WC}}\right) \tag{1.21}$$

where $\bar{V}_{\{Zr\}}$ is the effective molar volume of {Zr} in the infiltrated liquid residing in the prior pore volume and is given by:

$$\bar{V}_{\{Zr\}} = \frac{\bar{V}_{Zr_yCu_{1-y}}}{y} \tag{1.22}$$

where *y* is the mole fraction of zirconium remaining in the Zr-Cu liquid and $\bar{V}_{ZryCu1\text{-}y}$ is the molar volume of the infiltrating liquid. Using equation (1.22) and available literature data[37,38] for the liquid densities of Cu-Zr alloys (see Table 3), $\bar{V}_{\{Zr\}}$ has been evaluated for

congruently melting infiltrating compositions Zr_2Cu and $Zr_{14}Cu_{51}$ at 1100°C as 18.17 and 42.18 cm^3/mol, respectively. During infiltration, the composition of the infiltrating liquid is assumed constant; however, after pore choke-off, the composition will continually be depleted of zirconium until either all WC and/or zirconium reactants are consumed.

The terms $V_{\{Zr\},X}$ and $V_{WC,X}$ in equation (1.21) are the instantaneous volume fractions of Zr-bearing liquid residing in the prior pore volume and WC, respectively, remaining after extent of reaction *X*. For a preform consisting initially of pure WC, the WC volume fraction remaining after any arbitrary extent of reaction *X* is given by:

$$V_{WC,X} = (1 - \mathrm{X})\left(1 - V_{pore,i}\right) \tag{1.23}$$

The volume fraction of Zr-bearing liquid remaining after any arbitrary extent of reaction *X* is given by:

$$V_{\{Zr\},X} = V_{pore,i} - \mathrm{X}Z\left(1 - V_{pore,i}\right) \tag{1.24}$$

where *Z* is the solid volume change upon reaction, which reduces to equation (1.3) for a target initial pore volume fraction $V_{pore,i} = \Psi$ such that, when $X = 1$, $V_{\{Zr\},X} = V_{pore,f} = 0$.

Recalling that Γ has been defined as the extent of reaction occurring during continuous, rapid infiltration of liquid reactant (relative to consumption via reaction), the maximum obtainable value of Γ, Γ_{max}, is determined by the point at which reaction-induced densification causes choke-off and is found by setting $V_{\{Zr\},X} = V_{choke\text{-}off}$ and solving for $X = \Gamma_{max}$ in equation (1.24):

$$\Gamma_{\max} = \left(\frac{1}{Z}\right)\frac{V_{pore,i} - V_{choke-off}}{1 - V_{pore,i}} \tag{1.25}$$

This is plotted below in Figure 28 for choke-off volume fractions of 0.05, 0.10, 0.15 and 0.20:

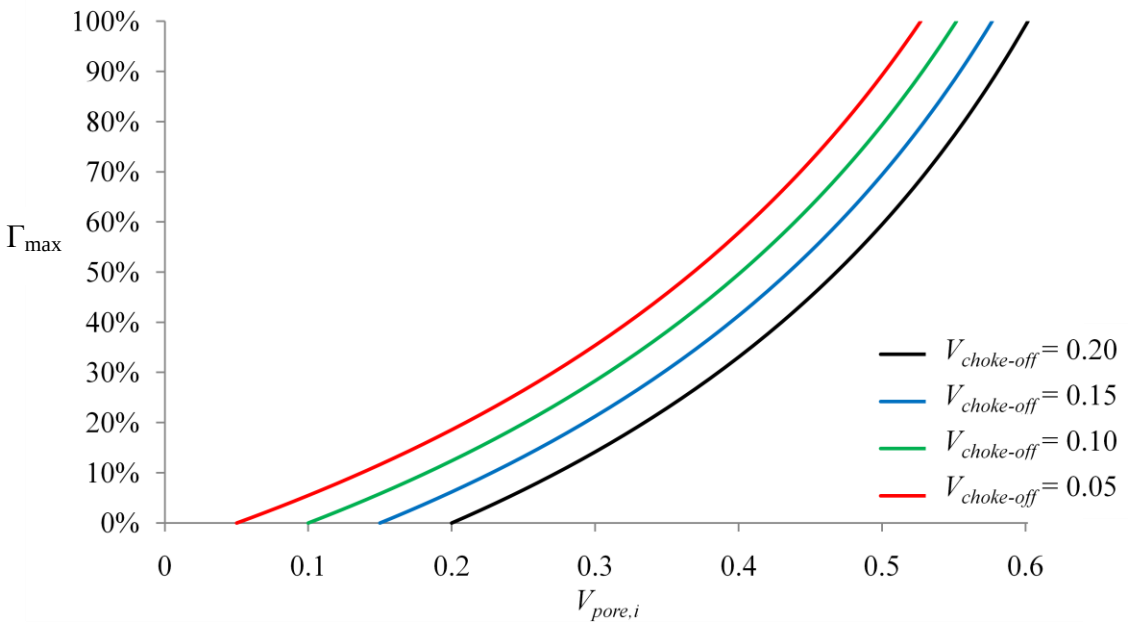

Figure 28: Maximum extent of reaction Γ_{max} to obtain final pore volume fraction $V_{choke\text{-}off}$ as function of preform pore volume $V_{pore,i}$.

Preforms having $V_{pore,i} < V_{choke\text{-}off}$ cannot be infiltrated, while preforms having $V_{pore,i} > V_{\Gamma}$, where V_{Γ} is the critical preform pore volume fraction for which complete reaction ($X = 1$) achieves $V_{\{Zr\},X} = V_{choke\text{-}off}$, would not reach the threshold for choke-off even after complete reaction. Therefore, Γ only takes on meaningful values for preform pore volume fractions in the range $V_{choke\text{-}off} < V_{pore,i} < V_{\Gamma}$. This value of V_{Γ} is readily obtained by setting $V_{\{Zr\},X} = V_{choke\text{-}off}$ in equation (1.24) and solving for $V_{pore,i} = V_{\Gamma}$ and is given by:

$$V_{\Gamma} = \frac{V_{choke-off} + Z}{1 + Z} \tag{1.26}$$

which corresponds to $V_{\Gamma} = 0.6016$ for Z=1.008 and $V_{choke} = 0.20$.

As shown in equation (1.20), in order to achieve complete reaction ($X = 1$), it is necessary for $\beta = 1$ at some stage of the reactive infiltration. β certainly cannot increase after infiltration is arrested since reactant supply would cease; however, it is not immediately clear how it changes during reactive infiltration under conditions of continual re-supply of liquid reactant. The change in β with extent of reaction during

infiltration, Γ, can be found by taking the derivative of (1.21) with respect to extent of reaction X (after substituting expressions (1.23) and (1.24) for $V_{\{Zr\},X}$ and $V_{WC,X}$) and evaluating for $X = \Gamma$ (i.e. – considering only the extent of reaction prior to choke-off), which is given by:

$$\left.\frac{d\beta}{d\mathrm{X}}\right|_{X=\Gamma} = \frac{V_{pore,i} - Z\left(1 - V_{pore,i}\right)}{(1-\Gamma)^2\left(1 - V_{pore,i}\right)} \Big/ \left(\frac{\bar{V}_{\{Zr\}}}{\bar{V}_{WC}}\right) \tag{1.27}$$

An inflection line exists in the curve at $V_{pore,i} = \Psi = \frac{Z}{1+Z}$ such that $d\beta/d\mathrm{X}|_{\mathrm{X}=\Gamma} = 0$. That is, at the target preform porosity, the molar ratio of zirconium within the infiltrated part to unreacted tungsten carbide remains constant during reaction *up to the point of pore choke-off*. (After pore choke-off, $\bar{V}_{\{Zr\}}$ is not constant and varies with extent of reaction, since the infiltrated liquid is continually depleted of zirconium.) For $V_{pore,i} > \Psi$, $d\beta/d\mathrm{X}|_{\mathrm{X}=\Gamma} > 0$ *up to the point of pore choke-off* while for $V_{pore,i} < \Psi$, $d\beta/d\mathrm{X}|_{\mathrm{X}=\Gamma} < 0$.

It may seem concerning that $d\beta/d\mathrm{X}|_{\mathrm{X}=\Gamma} < 0$ for preforms having $V_{pore,i} < \Psi$, since the extent of reaction that can occur after infiltration, given by $(1-\Gamma)\beta|_{\mathrm{X}=\Gamma}$ in (1.20), decreases with β. However, despite β decreasing with increasing X for preforms with $V_{pore,i} < \Psi$, the extent of reaction is nonetheless maximized by maximizing the extent of reaction occurring during infiltration. This can be shown by substitution of equations (1.21), (1.23), and (1.24) into (1.20):

$$X = \Gamma + (1-\Gamma)\left[\frac{V_{pore,i} - \Gamma Z\left(1 - V_{pore,i}\right)}{(1-\Gamma)\left(1 - V_{pore,i}\right)} \Big/ \left(\frac{\bar{V}_{\{Zr\}}}{\bar{V}_{WC}}\right)\right] \tag{1.28}$$

which can be re-arranged as:

$$X = \Gamma\left[1 - Z\Big/\left(\frac{\bar{V}_{\{Zr\}}}{\bar{V}_{WC}}\right)\right] + \left[\frac{V_{pore,i}}{\left(1 - V_{pore,i}\right)} \Big/ \left(\frac{\bar{V}_{\{Zr\}}}{\bar{V}_{WC}}\right)\right] \tag{1.29}$$

which, upon differentiating with respect to Γ, yields:

$$\frac{dX}{d\Gamma} = 1 - \left[Z \Big/ \left(\frac{\bar{V}_{\{Zr\}}}{\bar{V}_{WC}}\right)\right] \tag{1.30}$$

This expression is positive for $Z < (\bar{V}_{\{Zr\}}/\bar{V}_{WC})$, independent of the initial preform pore volume fraction. The ratio $(\bar{V}_{\{Zr\}}/\bar{V}_{WC})$ is evaluated as 1.45 and 3.37 for Zr_2Cu and $Zr_{14}Cu_{51}$, respectively, compared to $Z = 1.008$. This implies that, for both Zr_2Cu and $Zr_{14}Cu_{51,}$ increasing extent of reaction during infiltration always increases the maximum extent of reaction achievable for all preform pore volume fractions.

The maximum total extent of reaction, X_{max}, is given by substitution of the expression for Γ_{max} given by (1.25) for Γ in (1.29):

$$\begin{aligned} X_{max} &= \Gamma_{\max}\left[1 - Z\Big/\left(\frac{\bar{V}_{\{Zr\}}}{\bar{V}_{WC}}\right)\right] + \left[\frac{V_{pore,i}}{(1 - V_{pore,i})}\Big/\left(\frac{\bar{V}_{\{Zr\}}}{\bar{V}_{WC}}\right)\right] \\ &= \left[\left(\frac{1}{Z}\right)\frac{V_{pore,i} - V_{choke-off}}{1 - V_{pore,i}}\right]\left[1 - Z\Big/\left(\frac{\bar{V}_{\{Zr\}}}{\bar{V}_{WC}}\right)\right] \\ &+ \left[\frac{V_{pore,i}}{(1 - V_{pore,i})}\Big/\left(\frac{\bar{V}_{\{Zr\}}}{\bar{V}_{WC}}\right)\right] \end{aligned} \tag{1.31}$$

which, upon combining like terms, simplifies to:

$$X_{max} = \frac{V_{pore,i} - V_{choke-off}\left(1 - \left[Z\Big/\left(\frac{\bar{V}_{\{Zr\}}}{\bar{V}_{WC}}\right)\right]\right)}{Z(1 - V_{pore,i})} \tag{1.32}$$

This expression has been graphically evaluated (Figure 29 and Figure 30) for Zr_2Cu and $Zr_{14}Cu_{51}$ infiltrating compositions for selected preform pore volume fractions greater than 0.45:

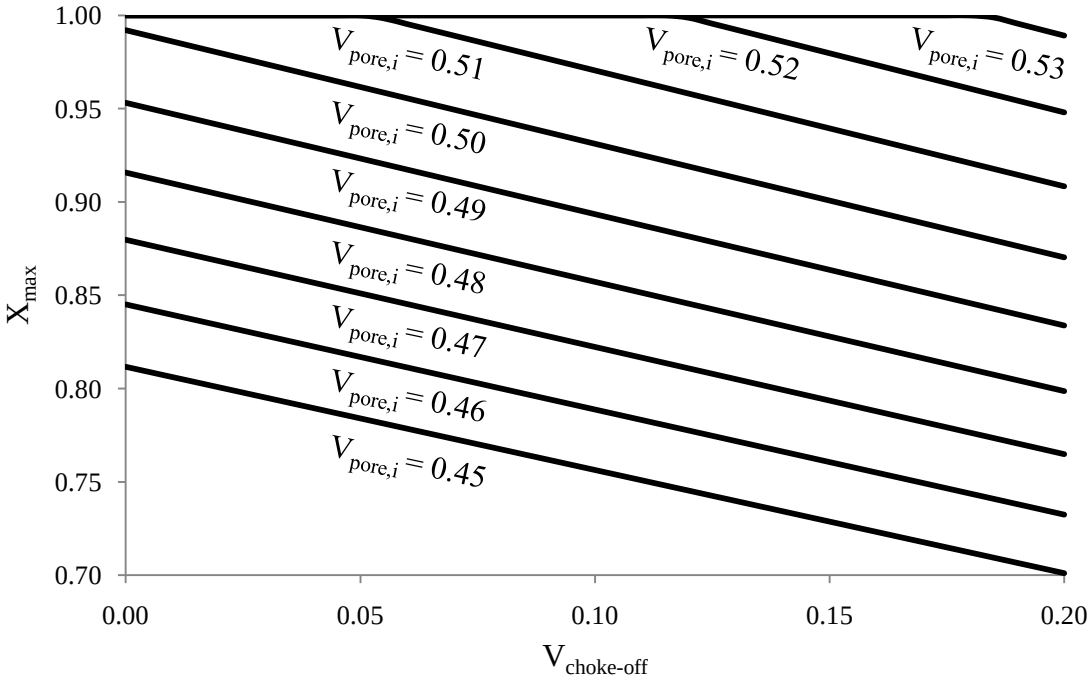

Figure 29: Maximum extent of conversion for preform infiltrated with Zr_2Cu.

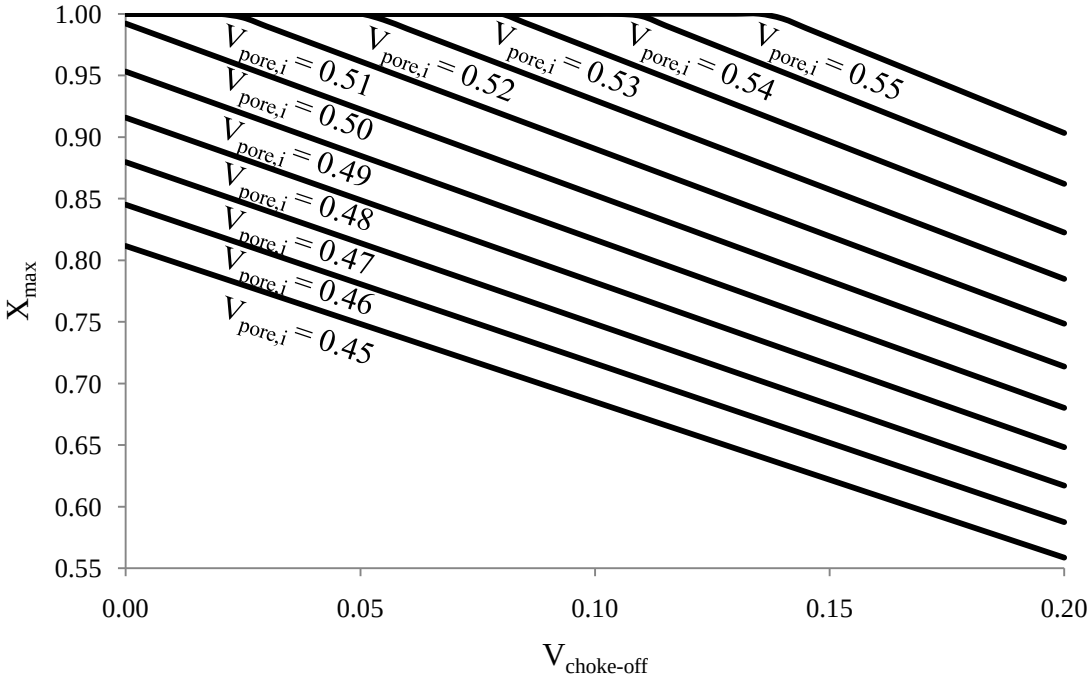

Figure 30: Maximum extent of conversion for preform infiltrated with $Zr_{14}Cu_{51}$.

The minimum preform pore volume fraction for which complete reaction (X_{max} = 1) is possible is found by re-arranging equation (1.32) to solve for $V_{pore,i}$ and is given by the following expression:

$$V_{pore,i} \geq \frac{Z + V_{choke-off}\left(1 - \left[Z/\left(\frac{V_{\{Zr\}}}{V_{WC}}\right)\right]\right)}{1 + Z} \tag{1.33}$$

This expression is graphically evaluated (Figure 31) for Zr_2Cu and $Zr_{14}Cu_{51}$ infiltrating compositions:

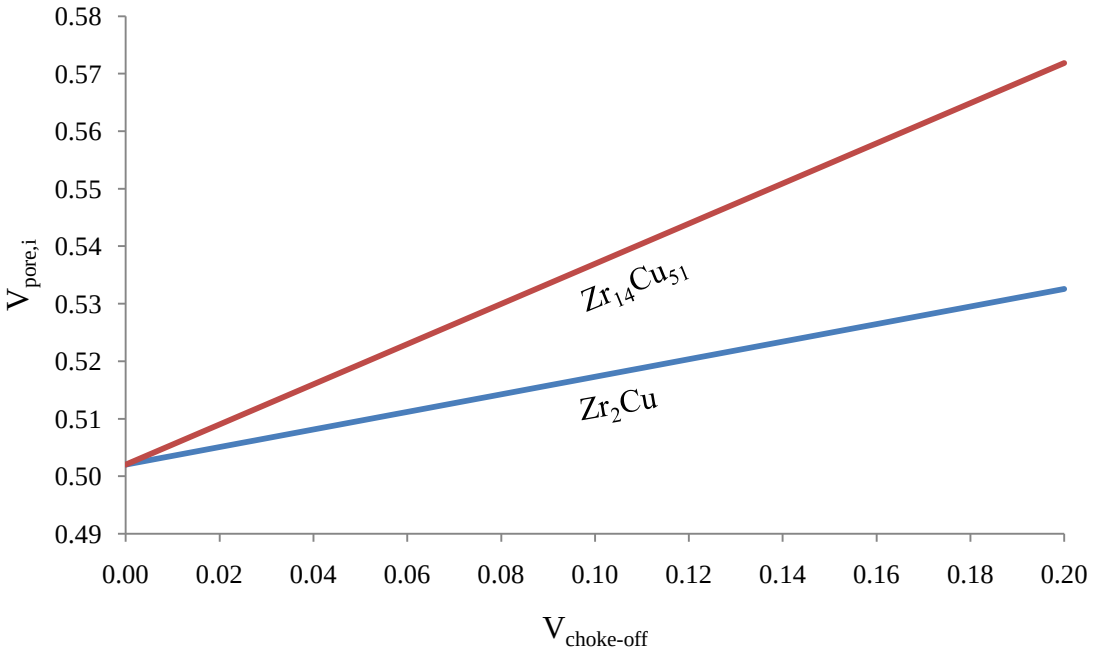

Figure 31: Minimum preform pore volume fraction as function of infiltrating composition and pore choke-off volume fraction to achieve complete reaction.

Values for X_{max} strongly depend on the value of $V_{choke-off}$. For example, for preforms having the target pore volume fraction Ψ (i.e. – those that are designed to produce composites maximal in ZrC content and minimal in Cu content), the theoretical maximum extent of conversion during continuous infiltration and total extent of conversion taking into account the effects of pore closure are summarized in Table 7:

Table 7: Maximum extents of conversion for pure WC preforms with $V_{pore,i} = \Psi$ as functions of infiltrating composition and $V_{choke\text{-}off}$.

Extent of Conversion	$V_{choke\text{-}off}$ = 0.20	$V_{choke\text{-}off}$ = 0.15	$V_{choke\text{-}off}$ = 0.10	$V_{choke\text{-}off}$ = 0.05	$V_{choke\text{-}off}$ = 0.00
Total (Zr_2Cu)	0.8778	0.9038	0.9389	0.9694	1.0000
Total ($Zr_{14}Cu_{51}$)	0.7206	0.7905	0.8603	0.9302	1.0000
Γ_{max}	0.6016	0.7012	0.8008	0.9004	1.0000

An additional consideration must be made concerning the molar volume change of reaction under conditions where pore choke-off has occurred. Consider the general reaction:

$$x\,WC + Zr_xCu_{1-x}(l) \leftrightarrow x\,ZrC + x\,W + (1-x)\,Cu(l) \tag{1.34}$$

where Cu(l) cannot be extruded out through an open pore network. The molar volume change of reaction (1.34) at 1100°C, including liquid phases, is -5.1% and -21.3% for $Zr_2Cu(l)$ and $Zr_{14}Cu_{51}(l)$, respectively using values tabulated in Table 3. Therefore, the consumption of {Zr} from the reactive liquid entrapped within the pores after choke-off can result in the generation of minor amounts of porosity.

1.5.2. Unreacted Cores

Preforms with $V_{pore,i} < \Psi$ may retain solid reactant in the form of unreacted cores. Depending on its material properties, the presence of this unreacted phase may or may not be detrimental for the desired application. Therefore, it is useful to develop a method to quantify the amount and distribution of unreacted cores in composites produced by DCP.

Consider, for example, a spherical particle of WC reacting according to reaction (1.1) where the WC/W, W/ZrC and ZrC/liquid interfaces are described by their radial positions as shown in Figure 32:

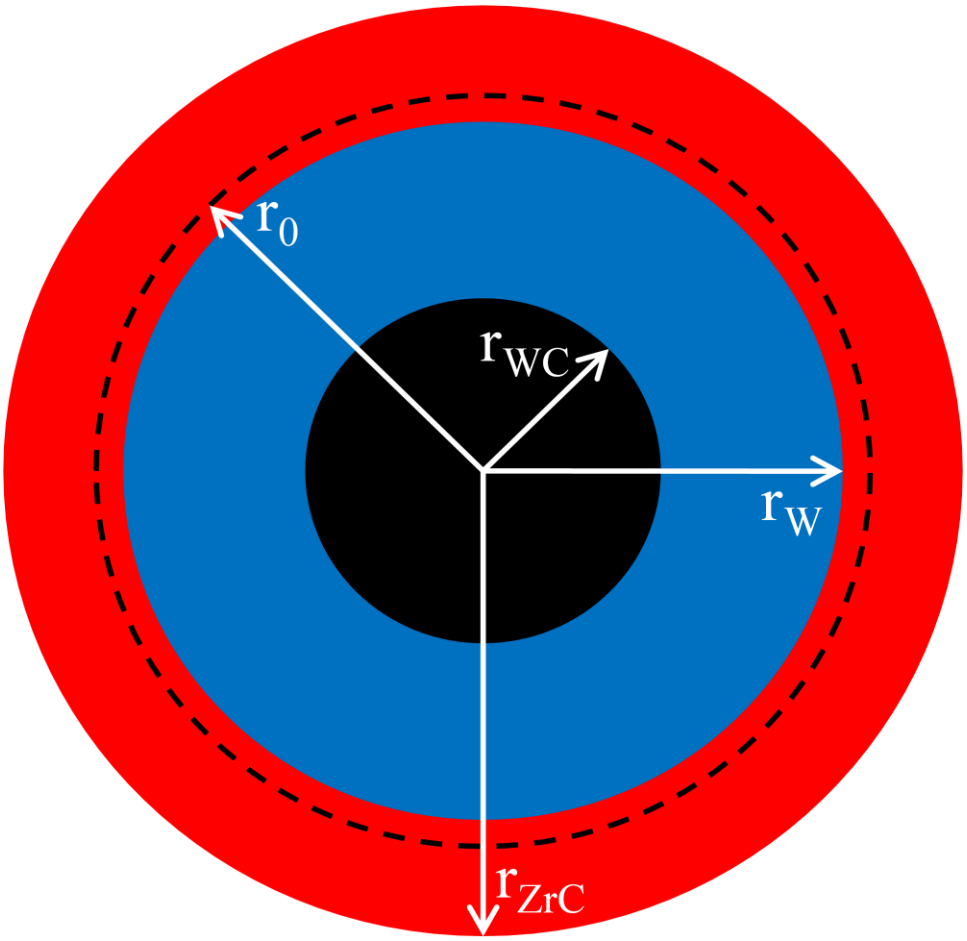

Figure 32: Reacting WC particle (black) with W (blue) and ZrC (red) layers relative to the original particle size (black dashed) (Drawn to scale for a spherical WC particle 90 vol. % reacted)

The radial positions of the WC/W, W/ZrC and ZrC/liquid interfaces as a function of volume extent of reaction are given by:

$$\frac{r_{WC}}{r_0} = (1 - X)^{1/3} \tag{1.35}$$

$$\frac{r_W}{r_0} = \left(1 - X + X\left[{}^{V_W}/_{V_{WC}}\right]\right)^{1/3} \tag{1.36}$$

$$\frac{r_{ZrC}}{r_0} = (1 + ZX)^{1/3} \tag{1.37}$$

where r_0 is the original particle radius. Values are evaluated in Figure 33:

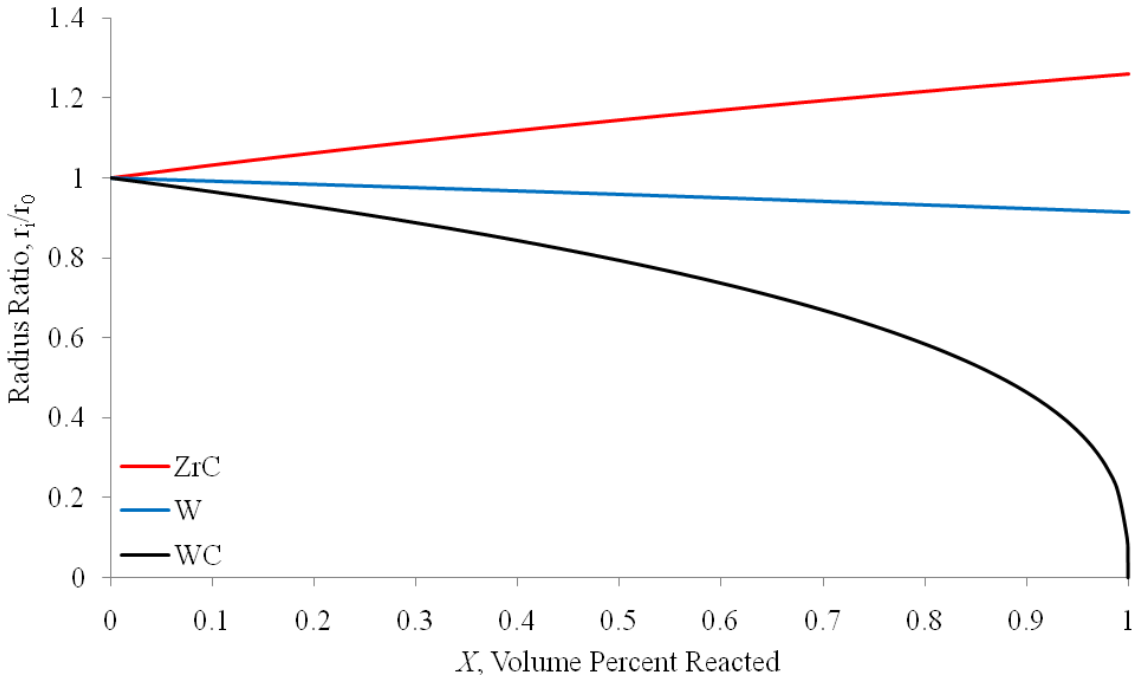

Figure 33: Ratio of the radial positions of the WC/W (black), W/ZrC (blue), and ZrC/liquid (red) interfaces to the unreacted particle radius as functions of the volume percent reacted.

As a WC particle undergoes reaction, the position of the WC/W interface recedes while the position of the ZrC/liquid interface expands as governed by particle geometry and molar volume ratios. Selected values are summarized in Table 8:

Table 8: Ratio of the radial positions of the WC/W, W/ZrC, and ZrC/liquid interfaces to the unreacted particle radius as functions of the volume percent reacted.

X	r_{WC}/r_0	r_W/r_0	r_{ZrC}/r_0
0.80	0.585	0.933	1.218
0.90	0.464	0.923	1.240
0.95	0.368	0.919	1.251
0.99	0.215	0.915	1.260
0.999	0.100	0.914	1.261
0.9999	0.046	0.914	1.262
1	0	0.914	1.262

Of particular interest is the size of the unreacted WC core: 80 vol. % converted spherical particles undergoing DCP reaction will have unreacted cores 58.5% of the original

particle radius. Similarly, unreacted cores 10.0% of the original particle radius will persist for 99.9 vol. % converted spherical particles.

It is unclear to what extent, if any, the presence of unreacted WC cores may have on the performance of W/ZrC-bearing composites produced via DCP. W and WC cannot be in equilibrium and will react to form W_2C above the eutectoid temperature of 1250°C[31]. However, the corresponding reaction to form W_2C is not accompanied by any appreciable volume change. W_2C does not melt substantially lower than WC, and neither carbide species melts significant lower than the W-ZrC eutectic temperature. Additionally, WC and W_2C exhibit similar hardness[31], density[29], and CTE[24,25] as compared to ZrC: thus, their presence may not prove detrimental for intended composite applications.

1.5.3. Selective Oxidation of Residual Carbon

WC preforms pressed with rice starch binder contain residual carbon[39] after inert atmosphere pyrolysis and sintering treatments. Removal of pore obstructing carbon residue is necessary prior to reactive infiltration. Controlled p_{O2} heat treatments using CO/CO_2 gas buffer mixtures can selectively oxidize free carbon without oxidation of WC. The following reactions are considered:

$$CO_2(g) + C \leftrightarrow 2CO(g) \tag{1.38}$$

$$CO_2(g) + WC \leftrightarrow W + CO(g) \tag{1.39}$$

$$3CO_2(g) + WC \leftrightarrow WO_2 + 4CO(g) \tag{1.40}$$

$$4CO_2(g) + WC \leftrightarrow WO_3 + 5CO(g) \tag{1.41}$$

$$CO_2(g) + 2WC \leftrightarrow W_2C + 2CO(g) \tag{1.42}$$

For sake of simplicity, the sub-oxides of W, including $WO_{2.72}$, $WO_{2.722}$, $WO_{2.9}$, and $WO_{2.96}$, are neglected. This may cause slight error in the calculated upper bound for the gas phase mixture composition, as the formation of these sub-oxides may precede the formation of the bounding oxide stoichiometries. Other reactions products, such as $O_2(g)$ or free carbon, are not considered, as the driving force for these reactions is considerably less than for the formation of CO(g). The following thermochemical analysis assumes a pure atmosphere consisting of the two species CO(g) and $CO_2(g)$. The total atmospheric pressure is assumed to be 1 atmosphere. All solid reactants and products are taken at unit activity.

In order to oxidize carbon, the p_{CO2}/p_{CO} ratio must be greater than the equilibrium values calculated for reaction (1.38). Therefore, this equilibrium p_{CO2}/p_{CO} value is taken as the lower bound for the gas composition needed to oxidize carbon. In order to avoid oxidation of WC, the p_{CO2}/p_{CO} ratio must be less than the equilibrium values calculated for reactions (1.39) thru (1.42). Table 9 summarizes the permissible range of a CO/CO_2 gas mixture in terms of the composition of CO(g) to selectively oxidize carbon from WC preforms:

Table 9: Selective oxidation of carbon in WC preforms using CO/CO_2 gas buffers

T [°C]	Lower Bound Percent CO	Upper Bound Percent CO
600	22.40%	25.37%
700	37.60%	61.28%
800	52.93%	88.58%
900	65.81%	97.26%
1000	84.95%	99.26%
1100	95.37%	99.76%
1200	98.53%	99.91%
1300	99.48%	99.96%
1400	99.81%	99.98%
1500	99.93%	99.99%

No gas composition from 0-500°C satisfies the requirements for selective oxidation. The practically useful temperature ranges for selective oxidation are between 600-1100°C. Since oxidation equilibrium is established locally, and gas phase reactants and products may require time to diffuse into/out of a tortuous path through the porous preform, it is desirable to choose a temperature which allows for selective oxidation over as wide a gas phase composition range as possible. Static thermogravimetric measurements (Figure 10) indicate that the oxidation process proceeds measurably between 900°C and 1000°C, though the oxidation of residual carbon proceeds at 1000°C using a gas composition of 90 vol. % CO/10 vol. % CO_2 at twice the rate observed at 900°C using a gas composition of 25 vol. % CO/75 vol. % CO_2 for the same fixed total flow rate of 667 mL/min (i.e. – after a 3.21 wt. % loss during inert atmosphere decomposition, an additional 0.21 wt. % loss was observed for treatment at 1000°C versus an additional 0.10 wt. % loss for treatment at 900°C for the same treatment times). Therefore, selective oxidation of carbon residue from WC preforms employing rice starch as a binder was preferably conducted at 1000°C using a gas composition of 90 vol. % CO/10 vol. % CO_2 prior to reactive infiltration.

1.6. *Concluding Remarks*

The DCP process has been shown to be capable of producing near net-shape/dimension metal/ceramic composites via reaction-induced densification of a porous ceramic preform. Two rapid prototyping techniques, CNC machining and 3-D printing, have been utilized to shape porous WC preforms that subsequently have been reactively infiltrated to produce W/ZrC-bearing composites. Independent of preform fabrication

technique, the reactive infiltration of Zr_2Cu into pure WC preforms having starting relative densities in the range 42.3-47.7% results in composites with calculated average phase contents of 51-54 vol. % ZrC, 32-33 vol. % W, 5-9 vol. % Cu, 2-5 vol. % WC, and -1-7 vol. % pores. Thus, W/ZrC-bearing composites having less than 13-17 vol. % secondary phases (residual copper, uninfiltrated closed porosity and unreacted WC) are readily achieved by combination of the DCP process with rapidly prototyped preforms.

The microstructures of DCP processed composites have been shown to be derived from the fabrication technique used for preparing the ceramic preform: preforms fabricated via CNC machining exhibit microstructures consisting of uniformly distributed W particles in a continuous ZrC matrix while those made via the layer-by-layer 3-D printing technique exhibit laminated microstructures consisting of alternating regions locally enriched in W and ZrC. Future implementations of the DCP process may include refined preform fabrication techniques to introduce greater anisotropy into the microstructure, so as to tailor both the phase distributions and properties of the DCP-derived composites.

A model has been developed to describe the evolution of phase contents during volume expansive reactive infiltration, using preform pore volume fraction, pore choke-off threshold and reactant physical properties as inputs. The model assumes that the process induces no change in external dimensions of the part, that reactive infiltration is conducted under conditions where the infiltration rate is much faster than the reaction rate, and that the preform consists of a single, pure reactive component. With further mathematical development, the model can likely be modified to ease the restrictions of these assumptions. Future work is suggested to verify the predictions of the models. For

example, the composite phase contents are predicted to vary based upon several parameters that can be adjusted systematically in the laboratory, such as the composition of the infiltrating liquid, the extent of reaction occurring during continuous re-supply of reactant (which is expected to be proportional to time spent immersed in the melt), and the starting preform pore volume fraction. It is also suggested that efforts be made to improve the accuracy of characterization methods to quantify composite phase contents in order to validate predicted trends that may fall within the calculated error of the currently employed methods.

1.7. *References*

[1] Evans, A.G. and Marshall D.B. "The mechanical behavior of ceramic matrix composites." *Acta Metall.*, **37**(10), 2567-2583 (1989).

[2] Chawla, N. and Shen. Y. "Mechanical behavior of particle reinforced metal matrix composites." *Adv. Eng. Mat.*, **3**(6), 357-370 (2001).

[3] Speyer, F. "Ablative composites containing in situ reaction-formed refractory metal carbides," *Ind. Eng. Chem. Prod. Res. Develop.*, **10**(1), 99-111 (1971).

[4] Raddatz, O., Schneider, G.A., Mackens, W., Voss, H. and Claussen, N. "Bridging stresses and R-curves in ceramic/metal composites," *J. Euro. Ceram. Soc.*, **20**(13), 2261-2273 (2000).

[5] Song, G.M., Wang, Y.J. and Zhou, H. "Elevated temperature ablation resistance and thermophysical properties of tungsten matrix composites reinforced with ZrC particles." *J. Mat. Sci.*, **36**, 4625-4631 (2001).

[6] Hebsur, M.G. "Development and characterization of SiC(f)/MoSi2-Si3N4(p) hybrid composites," *Mat. Sci. Eng.*, **A261**, 24-37 (1999).

[7] Fauchais, P. "Understanding plasma spraying," *J. Phys. D: Appl. Phys.*, **37**, R86-R108 (2004).

[8] Patterson, M.C.L., He, S., Fehrenbacher, L.L., Hanigofsky, J. and Reed, B.D. "Advanced HfC-TaC oxidation resistant composite rocket thruster," *Mat. Manu. Proc.*, **11**(3), 367-379 (1996).

[9] Chiang, Y., Haggerty, J.S., Messner, R.P. and Demetry, C. "Reaction-based processing methods for ceramic-matrix composites," *Am. Ceram. Soc. Bull.*, **68**(2), 420-428 (1989).

[10] Kumar, P. and Sandhage, K.H. "The displacive compensation of porosity (DCP) method for fabricating dense, shaped, high-ceramic bearing bodies at modest temperatures," *J. Mat. Sci.*, **34**, 5757-5769 (1999).

[11] Sandhage, K.H. and Kumar, P. "Method for Fabricating Shaped Monolithic Ceramics and Ceramic Composites through Displacive Compensation of Porosity, and Ceramics and Composites made Thereby," U. S. Patent No. 6,833,337, December 21, 2004.

[12] Sandhage, K.H., Unocic, R.R., Dickerson, M.B., Timberlake, M. and Guerra, K. "Method for Fabricating High-Melting, Wear-Resistant Ceramics and Ceramic Composites at Low Temperatures, U.S. Patent No. 6,598,656, July 29, 2003.

[13] Hozer, L., Lee, J.R. and Chiang Y.M. "Reaction-infiltrated, net-shape SiC composites," *Mat. Sci. Eng.*, **A195**, 131-143 (1995).

[14] Sandhage, K.H. "Materials 'alchemy': shape-preserving chemical transformation of micro-to-macroscale 3-D structures," *JOM*, **62**(6), 32-43 (2010).

[15] Dickerson, M.B. et al. "Near net-shape, ultra-high melting, recession-resistant ZrC/W-based rocket nozzle liners vis the displacive compensation of porosity (DCP) method," *J. Mat. Sci.*, **39**, 6005-6015 (2004).

[16] Subramanian,P.R. and Laughlin,D.E. *Binary Alloy Phase Diagrams*, Vol. 2, Massalski, T.B. (ed.), Materials Park, Ohio: The Materials Information Society, 1990.

[17] Novakovic, R., Muolo, M.L. and Passerone, A. "Bulk and surface properties of liquid X-Zr (X=Ag,Cu) compound forming alloys," *Surface Sci.*, **549**, 281-293 (2004).

[18] Zaitsev, A.I., Zaitseva, N.E., Alekseeva, Y.P., Kuril'chenko, E.M. and Dunaev, S.F. "Thermodynamic properties of melts and phase equilibria in the copper-zirconium system," *Inor. Mater.*, **39**(8), 816-825 (2003).

[19] Yamaguchi, K., Song, Y.-C., Yoshida, T. and Itagaki, K. "Thermodynamic investigation of the Cu-Zr system," *J. Alloys Compounds*, **452**, 73-79 (2008).

[20] Wang, N., Li, C., Du, Z., Wang, F. and Zhang, W. "The thermodynamic re-assessment of the Cu-Zr system," *CALPHAD*, **30**, 461-469 (2006).

[21] Turchanin, M.A. and Nikolaenko, I.V. "Enthalpies of solution of titanium, zirconium, and hafnium in liquid copper," *J. Alloys Compounds*, **236**, 236-242 (1996).

[22] Eremenko, V.N., Velikanova, T.Y., Artyukh, L.V., Aksel'rod, G.M. and Vishnevskii, A.S. *Dopov. Akad. Nauk Ukr. RSR, Ser. A: Fiz.-Mat. Tekh. Nauki*, 1, 80-85 (1976). From *Phase Diagrams for Zirconium and Zirconia Systems*, H. M. Ondik and H. F. Mcmurdie (ed.), American Ceramic Society, 2005.

[23] Kuz'ma, Y.B., Federov, T.F. and Shvets, E.A. "Phase equilibria in the system Zr-W-C," *Porosh. Met.*, **2**(26), 22-25 (1965).

[24] Touloukian, Y.S., Kirby, R.K., Taylor, R.E. and Desai, P.D. *Thermophysical Properties of Matter, Vol. 12: Thermal Expansion of Metallic Elements and Alloys*. New York: Plenum Press, (1975).

[25] Touloukian, Y.S., Kirby, R.K., Taylor, R.E. and Desai, P.D. *Thermophysical Properties of Matter, Vol. 13: Thermal Expansion of Non-Metallic Solids*. New York: Plenum Press, (1975).

[26] Hebsur, M.G. "Development and characterization of SiC(f)/$MoSi_2$-Si_3N_4(p) hybrid composites," *Mater. Sci. and Eng.*, **A261**, 24-37 (1999).

[27] Opeka, M.M., Talmy, I.G., Wuchina, E.J., Zaykoski, J.A. and Causey, S.J. "Mechanical, thermal, and oxidation properties of refractory hafnium and zirconium compounds," *J. Euro. Ceram. Soc.*, **19**, 2405-2414 (1999).

[28] Barin, I. *Thermochemical Data of Pure Substances*. Weinheim, Germany: VCH Verlagsgesellschaft, (1995).

[29] *JCPDS X-ray Diffraction Card File*. Newton Square, PA: International Centre for Diffraction Data, (2010).

[30] Storms, E.K. *The Refractory Carbides.* New York: Academic Press, (1967).

[31] Lassner, E. and Schubert, W.D. *Tungsten: Properties, Chemistry, and Technology of the Element, Alloys, and Chemical Compounds.* New York: Plenum Publishers, (1999).

[32] Arias, D. and Abriata, J.P. Cu-Zr Phase Diagram, ASM Alloy Phase Diagrams Center, P. Villars (ed.), Materials Park, OH: ASM International, (2006).

[33] Cahill, J.A. and Kirshenbaum, A.D. "The density of liquid copper from its melting point (1356K) to 2500K and an estimate of its critical constants," *J. Phys. Chem.*, **66**(6), 1080-1082, (1962).

[34] Rice, R.W. *Porosity of Ceramics.* New York: Marcel Dekker, (1998).

[35] Bentz, D.P. and Garboczi, E.J. "Percolation of phases in a three-dimensional cement paste microstructural model," *Cem. Concr. Res.*, **21**, 325-344, (1991).

[36] Ye, G., van Breugel, K. and Fraaij, A. "Three-dimensional microstructural analysis of numerically simulated cementitious materials," *Cem. Concr. Res.*, **33**, 215-222, (2003).

[37] Mendelev, M.I. et al. "Development of suitable interatomic potentials for simulation of liquid and amorphous Cu-Zr alloys," *Phil. Mag.*, **89**(11), 967-987, (2009).

[38] Krasovskyy, V.P., Naidich, Y.V. and Krasovskaya, N.A. "Surface tension and density of copper-zirconium alloys in contact with fluoride refractories," *J. Mat. Sci.*, **40**, 2367-2369, (2005).

[39] Lewis, J.A. "Binder removal from ceramics," *Annu. Rev. Mater. Sci.*, **27**, 147-173, (1997).

CHAPTER 2: Porous Metal/Metal Carbide Replicas of Carbon Templates via Gas-Solid Displacement Reactions

2.1. *Summary*

For the first time, shape-preserving gas-solid displacement reactions have been used to completely convert thick (> 1 mm) carbon templates into freestanding, monolithic porous metal/metal carbide replicas. The carbon template serves as consumable reducing agent for a suitable metal-bearing vapor phase, resulting in a self-limiting process that allows for uniform conversion throughout the body. Preservation of substrate morphology opens the possibility of utilizing biomorphic carbonaceous templates and well-established carbon microfabrication methods, such as polymerization/pyrolyzation and chemical vapor infiltration, for the direct fabrication of porous metal/metal carbide replicas.

Amorphous fibers and graphitic foams have been fully converted to tungsten replicas via reaction with tungsten oxychloride vapors generated *in-situ* via a displacement reaction between calcium chloride and tungsten oxide. Characterization via scanning electron microscopy, energy dispersive x-ray spectroscopy, x-ray diffraction, high resolution transmission electron microscopy and static thermogravitmetry indicate that no detectable residual carbon remains in the converted replicas.

A kinetic study was conducted to better understand the nature of the reaction of *in-situ* generated tungsten oxychloride vapors with dense graphite substrates at 1100°C for inlet gas velocities varying from 0.03-0.85 cm/s. Partial reaction of the substrates resulted in the formation of two product layers: a WC inner layer and a highly porous W

outer layer (nominal pore volume fraction of 64%). For a fixed molar extent of reaction, the thickness of the WC inner layer increased as a function of distance from the leading edge while the thickness of the W outer layer decreased. The molar composition of the product layer was determined as a function of inlet gas velocity for partially reacted samples (at extents of reaction of 15-20%) and found to increase from 25.4 mol.% W at an inlet gas velocity of 0.03 cm/s to 99.9 mol.% W at an inlet gas velocity of 0.85 cm/s. Chemical thermodynamic analysis of the likely reactions in this system is capable of explaining these trends as a result of gas phase composition and indicate that it should be possible, in theory, to selectively produce either W or WC by reactive conversion of carbon.

Complex reaction kinetics have been observed as a function of extent of reaction at a fixed inlet gas velocity of 0.85 cm/s. Further study is required to fully characterize the complex reaction pathways of this system, though likely rate determining steps have been identified on the basis of the magnitude and rate of change of reaction rate. Up to 50 vol. % conversion, substrate reaction kinetics are likely under a mass transport limited regime resulting in reactant starvation or are controlled by WO_2Cl_2(g) diffusion through a viscous gas layer of constant thickness. At greater than 50 vol. % conversion, the reaction is likely controlled by either diffusion of WO_2Cl_2 to the C/WC interface or a chemical reaction at the C/WC interface.

The application of tungsten/tungsten carbide replicas as porous preforms for use in conjunction with the Displacive Compensation of Porosity to produce near-fully dense, near-net shape ZrC/W-bearing composites with tailored microstructure has been demonstrated via the incorporation of W/WC-converted carbon fibers into reactively-

infiltratable porous preforms. Suggestions for future applications and improvements on the process are provided.

2.2. *Introduction*

2.2.1. Motivation for Reactive Conversion of Carbon Templates

The Displacive Compensation of Porosity (DCP) process is capable of producing complex, three-dimensional, near-net shape and near-net dimension metal/ceramic composites via the reactive infiltration of porous preforms[40]. As detailed in Chapter 1, the microstructures of composites produced via DCP are derived from microstructure of the starting preform. For example, WC preforms produced via CNC machining of partially-sintered cold-uniaxially-pressed billets developed uniform distributions of W particles in a continuous ZrC matrix microstructures while WC preforms produced via 3-D printing produced laminated W/ZrC-bearing microstructures consisting of alternating W-rich and ZrC-rich layers[41]. In either case, the observed microstructures develop as a result of the spatial distribution of WC particles whose phase contiguity results from particle necking during sintering.

Micromechanical models and experimental data show that the strength and fracture toughness of ceramic matrix composites can be improved by introduction of ductile metallic reinforcements[42,43,44,45,46,47]. The degrees by which crack deflection at weak metal/ceramic interfaces, and crack bridging by ductile metal reinforcements, improve fracture toughness have been shown to vary with both the amount, contiguity, and morphology of the reinforcing phase[44,45,46].

In order to introduce greater amounts of microstructural anisotropy in W/ZrC-bearing composites produced via the DCP process, it is necessary to develop WC preforms with aspected assemblages of WC particles having high amounts of phase

contiguity. Numerous attempts have been made to create highly-interconnected metal carbides (or metal carbide precursors, such as base metals and metal oxides) in the forms of discontinuous fibers and whiskers, continuous fibers and cloths, and as coatings by a wide variety of techniques. Chemical vapor deposition has widely been exploited using metal halide vapors, hydrogen, and hydrocarbon gases to deposit a variety of metal carbides[48,49,50]. Solution-based processing has yielded contiguous carbides by dissolution of metal chlorides in non-aqueous solvents, impregnation into organic templates and subsequent high temperature thermal treatment[51,52]. Sol-gel processing has produced oxide coatings that have been subsequently carbothermally reduced and carbidized[53,54,55]. Molten salts[56] and molten metal alloys[57,58] have been used as flux media for dissolution of reactive metals that react with carbon to form carbide coatings. Tungsten and tungsten oxide whiskers have been grown via vapor-liquid-solid mechanisms[59] by hydrogen reduction of tungsten oxide[60] and reaction of tungsten metal powder with nickel nitrate[61], respectively. Complex tungsten compounds have been grown as whiskers and subsequently simultaneously reduced and carbidized by thermal treatment in hydrogen/hydrocarbon atmospheres[62]. Nevertheless, these techniques require specialized processing equipment[50,60] or present processing challenges preventing their immediate adaptation to the production of contiguous WC preforms (such as cracking and shrinkage[51,52], limited chemistries for tungsten[56,57] or inability to produce thick coatings[53,54,55,58]).

Carbonaceous templates offer processing advantages for the production of porous WC preforms, such as the ease of graphite machining, readily available biomorphic templates,[63,64] and well-established carbon microfabrication methods, such as polymerization/pyrolyzation[65,66] and chemical vapor infiltration[67], whose complex geometries and microstructures may then be replicated as metals or metal carbides by direct and complete chemical conversion of the template. While some of the above-mentioned processing methods are able to form coatings on carbonaceous templates,

none directly and completely consume the template to form metal or metal carbide replicas; however, two reactive processing methods[68,69] have been reported to reactively convert high-surface area carbon to carbides via reaction with volatile metal oxide vapors:

$$MO_x(g) + (1+x)C \leftrightarrow MC + xCO(g) \quad (2.1)$$

Such reactions are feasible when sufficient metal oxide vapor pressures can be developed at desired reaction temperatures and appear to be enabled by the high reactivity of activated carbon surfaces. For example, the vapor pressure of silicon monoxide formed by equilibration of powdered silicon and silicon dioxide is 7.5×10^{-3} atm at 1400°C and 1 atm total pressure[70]. Similarly, the total vapor pressure of tungsten oxide vapor species formed over tungsten trioxide powder is 1.25×10^{-2} atm at 1400°C and 1 atm total pressure, and assuming an oxygen partial pressure greater than 6 ppb such that WO_3 is the most stable solid phase[70]. However, unlike silicon monoxide vapors, tungsten oxide vapors are highly corrosive and can react with refractory ceramic containers such as MgO, ZrO_2, Al_2O_3 and mullite to form eutectic liquids as low as 1120°C[71], making safe encapsulation of the carbon-containing article with tungsten oxide vapors challenging.

2.2.2. Initial Experimental Methods to Reactively Convert Carbon to W/WC Replicas

Due to difficulties in experimental design, initial attempts to convert carbon templates via reaction with tungsten oxide-based vapors proved unsuccessful. For example, experiments in quartz tube reactors at temperatures up to 1000°C generated no appreciable tungsten oxide-based vapors as evidenced by weight loss measurements of a WO_3 powder bed. Attempts to use mullite tube reactors at temperatures above 1200°C resulted in breakage of the tube (and damage to the furnace heating elements),

presumably due to formation of an Al_2O_3-WO_3 liquid. As a result of these challenges, a number of alternative coating and conversion techniques were explored in order to transform carbon templates, ranging from gas-solid reactions (halide and oxyhalide-based vapors), to liquid-solid reactions (oxide and metal alloy-based melts) to solid-solid reactions (oxide-based coatings). Of these various attempts, three potentially merit further investigation though are no longer being actively pursued by the present author: carbothermal reduction of B_2O_3-WO_3 melts[72], cathodic electodeposition of WO_3 from peroxotungstic acid solution[73] followed by carbothermal reduction, and the production of highly reactive tungsten sub-halides (preferably WCl_2) via displacement reaction with divalent transition metal halides. The results of the best efforts from such trials will now be briefly summarized.

The choice of oxide flux medium for liquid-solid reaction between carbon fibers and W-containing oxide melts is based on several factors: the flux should be non-volatile, exhibit high solubility for W-bearing species, non-reactive with carbon, and, preferably, exhibit poor or no solubility for carbon. Based on an evaluation of metal oxides, B_2O_3 was chosen as a flux medium as it is relatively non-volatile up to 1400°C[28], exhibits greater than 20 mol. % solubility for WO_3 above 1100°C[72], and is relatively inert with respect to carbon up to 1400°C[70]. Immersion of carbon fibers in a 4:1 W:C molar ratio in a 77 mol. % B_2O_3-23 mol. % WO_3 melt contained in a nickel crucible (99.9% purity, 45 mm top diameter x 57 mm height, Dual Mfg. Co. Ltd., Chicago IL) under an argon atmosphere at 1100°C for 30 hours produced tungsten coatings on carbon (as shown in Figure 34):

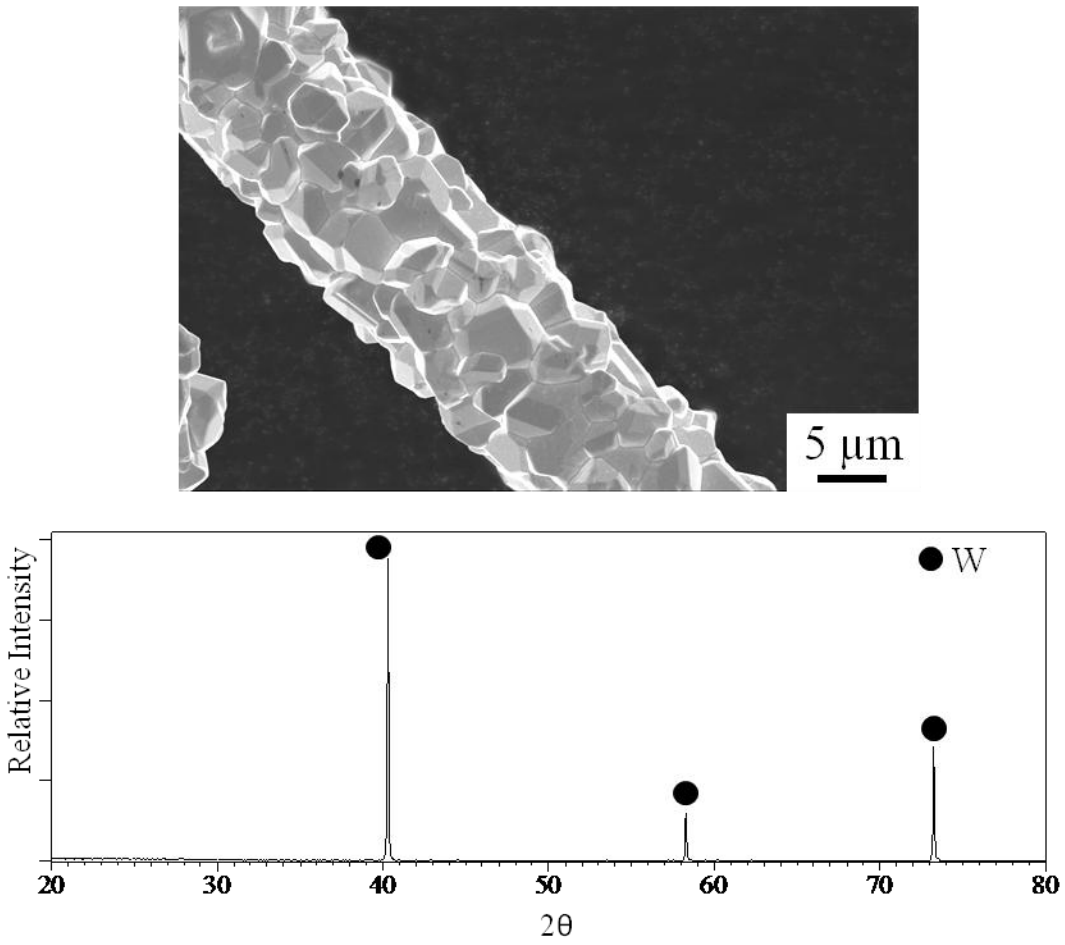

Figure 34: SEM and XRD analyses of carbothermal reduction of B_2O_3-WO_3 melts by carbon fibers at 1100°C (PDF Card No. 04-0806)

Carbothermal reduction is assumed to follow the reaction:

$$\{WO_3\} + 3C \leftrightarrow W + 3CO(g) \tag{2.2}$$

where $\{WO_3\}$ is tungsten oxide dissolved in the melt. In addition to W coatings, significant amounts of detached particles and abnormal grain growth were observed, as shown in Figure 35:

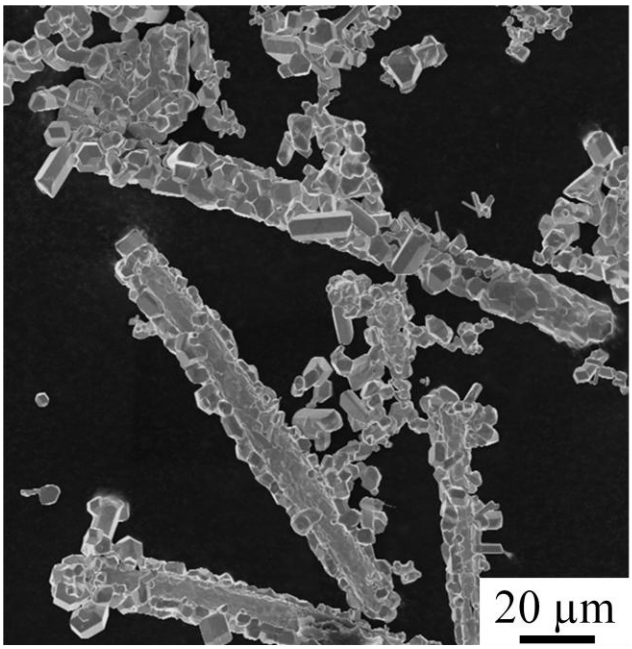

Figure 35: SEM image depicting detached particles and elongated grains resulting from reaction of carbon with B_2O_3-WO_3 melt at 1100°C, 30 hr

Methods to force the reaction front closer to the fiber surface are suggested, such as increasing the activity of WO_3 in the melt[74] or modification of melt composition to decrease carbon solubility.

A second experimental method to produce W/WC replicas of carbon templates involved cathodic electrodeposition of WO_3 coatings onto carbon from solutions of peroxotungstic acid prepared by dissolution of H_2WO_4 in 30 vol. % H_2O_2 via the following reaction[73]:

$$W_2O_{11}{}^{2-} + 6H^+ + 4e^- \leftrightarrow WO_3 + 3H_2O + O_2(g) \qquad (2.3)$$

Carbon fibers were pressed into a graphite cavity (see Figure 36), immersed into peroxotungstic acid electrolyte, and deposits were formed by application of +5 Vdc/20 mA for 10 minutes.

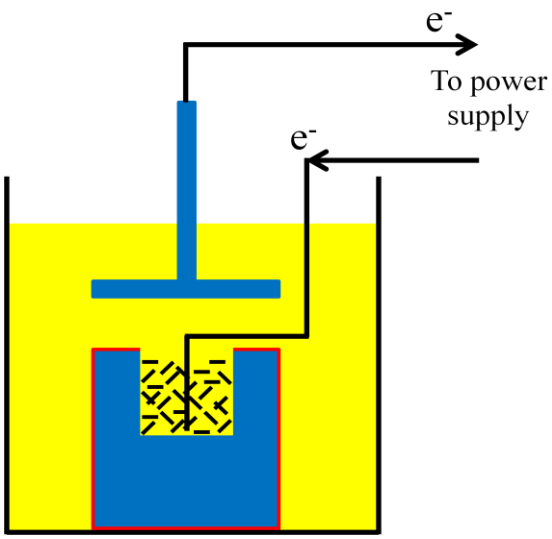

Figure 36: Schematic of cathodic electrodeposition apparatus (peroxotungstic acid electrolyte (yellow), graphite electrodes (blue)).

The outer surfaces of the graphite cathode were wrapped in electrical tape to ensure that electrical contact with the electrolyte occurs only within the inner cavity. Coatings produced via cathodic electrodeposition followed by heating in argon at 1200°C for 8 hours are shown in Figure 37:

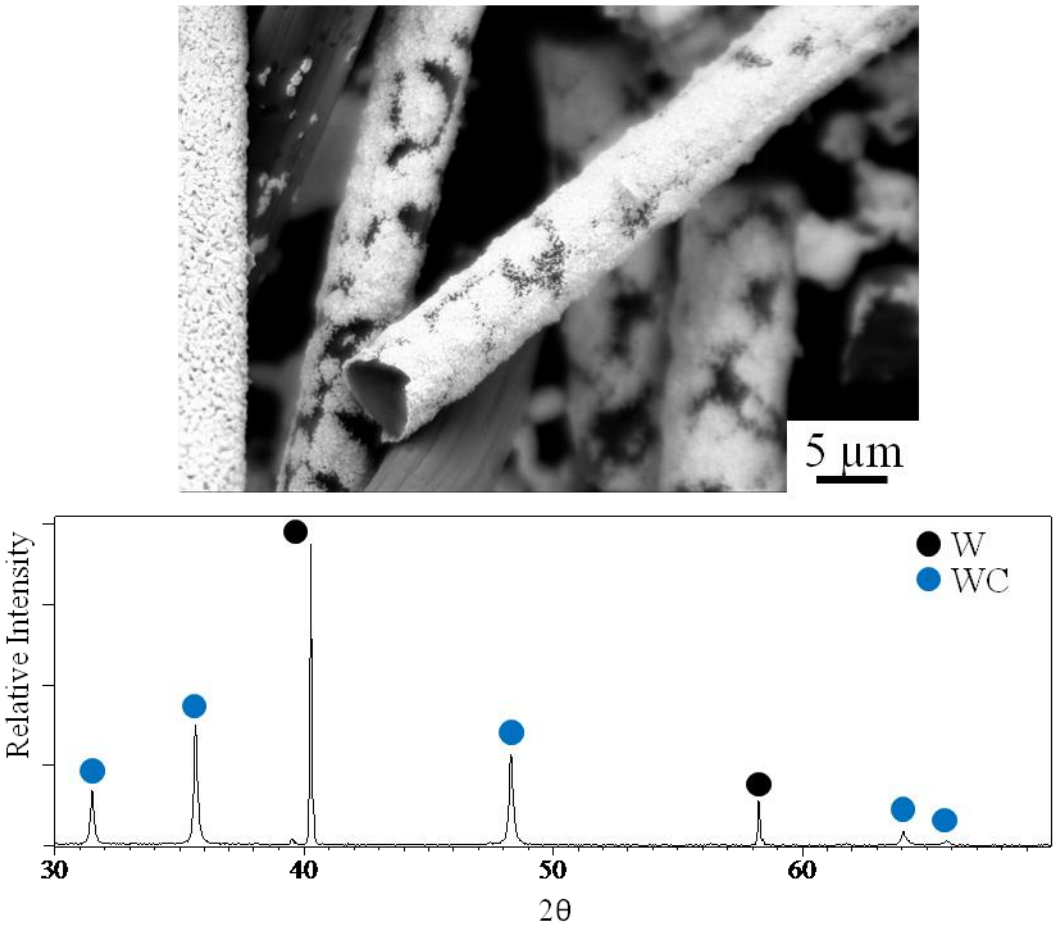

Figure 37: SEM and XRD analyses of carbothermal reduction of electrodeposited WO_3 on carbon fibers after firing at 1200°C for 8 hours in argon (PDF Card No. for W 04-0806, WC 25-1047)

Solid-solid reaction of underlying carbon with electrodeposited WO_3 was limited by the lack of formation of thick, coherent, and continuous coatings on the discontinuous fibers, assumed to be caused by poor electrical contact. Preforms, rather than discontinuous fibers, may provide a conductive template more suitable for this method.

Lastly, gas-solid reactions with tungsten subhalide vapors were investigated in order to directly form WC replicas of carbon templates. Figure 38 shows fibers produced via reaction with *in-situ* generated WCl_2(g):

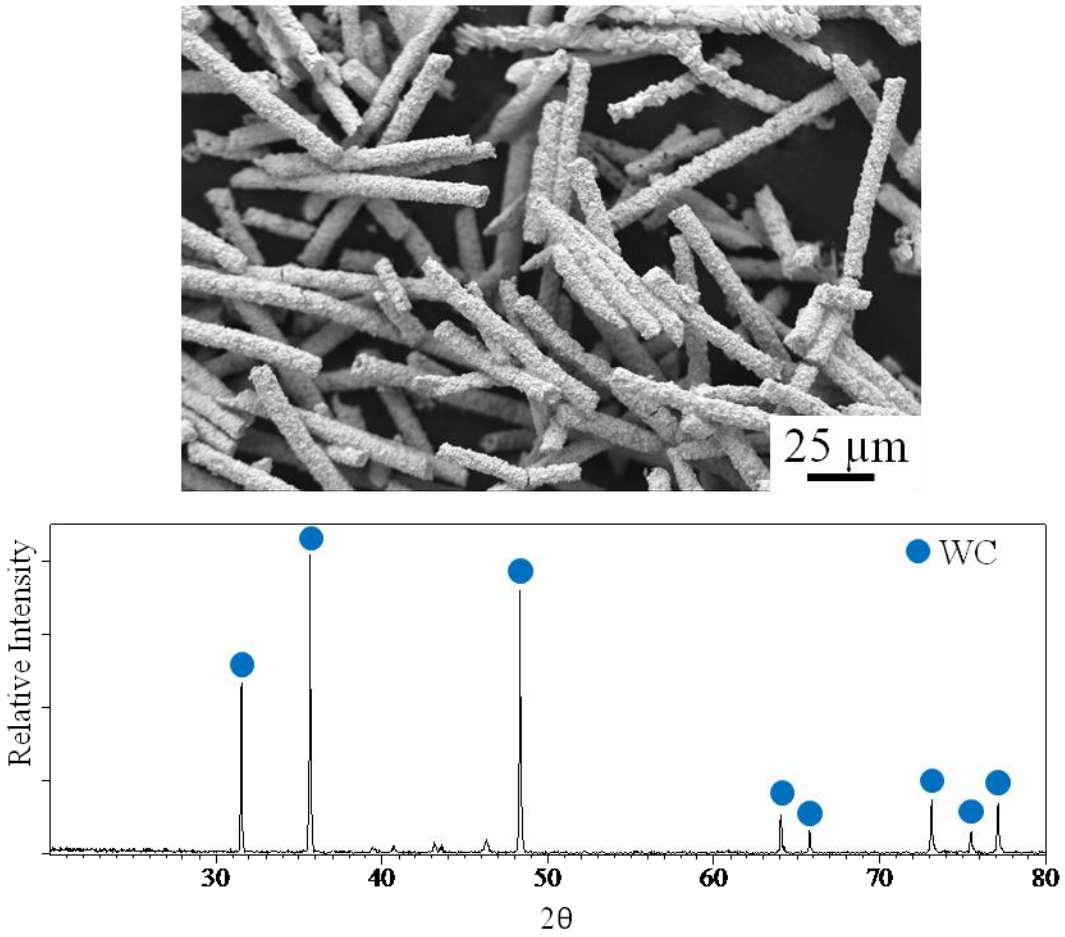

Figure 38: SEM and XRD analyses of reaction of carbon fibers with vapors produced by the displacement reaction between $CuCl_2$ and W at 1400°C for 7 hours (PDF Card No. 25-1047)

Gas-solid reaction with the vapors generated by the displacement between $CuCl_2$ and W was thought to proceed via the following reactions to directly produce carbide replicas:

$$CuCl_2 + W \leftrightarrow WCl_2(g) + Cu \quad (2.4)$$

$$2WCl_2(g) + C \leftrightarrow WC + WCl_4(g) \quad (2.5)$$

Three MgO crucibles (99.4% purity, 20 mm diameter x 20 mm height, Ozark Technical Ceramics, Webb City MO) were stacked atop each other with slits cut in the bottom of the middle and top crucibles. The stacked crucibles were sealed to each other with high temperature ceramic adhesive (Compound 571, Aremco Products Inc., Valley Cottage NY). $CuCl_2$ was kept within the bottom crucible, tungsten powder in the middle crucible

and carbon fibers in the top crucible. $CuCl_2$ vapors passed through the slit of the middle crucible, reacted with W according to reaction (2.4) with the product vapors passing through the slit of the top crucible and reacting with the carbon fibers. Although such reaction routes proved successful, they suffered from scalability issues associated with the high volatility of $CuCl_2$ and the formation of a diffusion barrier of Cu around reacting W particles. The reaction stoichiometry of (2.5) is especially noteworthy, as a volume expansion of +129.3% occurs, allowing for a porous carbon preform (e.g., a preform with 78.2 vol. % porosity) to be densified via reaction in order to form a WC replica suitable for DCP infiltration (e.g., a preform with 50.0 vol. % porosity). Future work might look into alternative methods to generate and deliver WCl_2(g).

As a result of the shortcomings of these techniques, a novel gas-solid displacement reaction using low-cost, *in-situ* generated metal oxyhalide vapors to reactively convert carbon templates directly to metal or metal carbide replicas has been developed. This chapter details an initial study of this gas-solid displacement reaction to produce porous tungsten replicas and shows as proof of concept the subsequent gas phase carbidization to produce porous tungsten carbide replicas for application to the DCP process.

2.3. *Experimental Procedures*

2.3.1. Conversion of Carbon Templates

Tungsten replicas were produced within a vertically oriented fixed bed reactor consisting of a fused silica tube (99.99% purity, 25 mm OD x 22 mm ID x 1 m length, Chemglass Life Sciences, Vineland NJ) housed within a mullite process tube (> 75%

mullite, 75 mm OD x 70 mm ID x 1.2m length, Coorstek, Golden CO) lined with graphite foil (96% carbon content, 0.38 mm thickness, Graftech Intl. Holdings Inc., Cleveland OH). Tubes were sealed with aluminum endcaps with Viton and Teflon o-rings and ferrules, respectively. Carbon templates were placed atop a frit within the uniform hot zone of a SiC-element resistance element furnace, as depicted schematically in Figure 39:

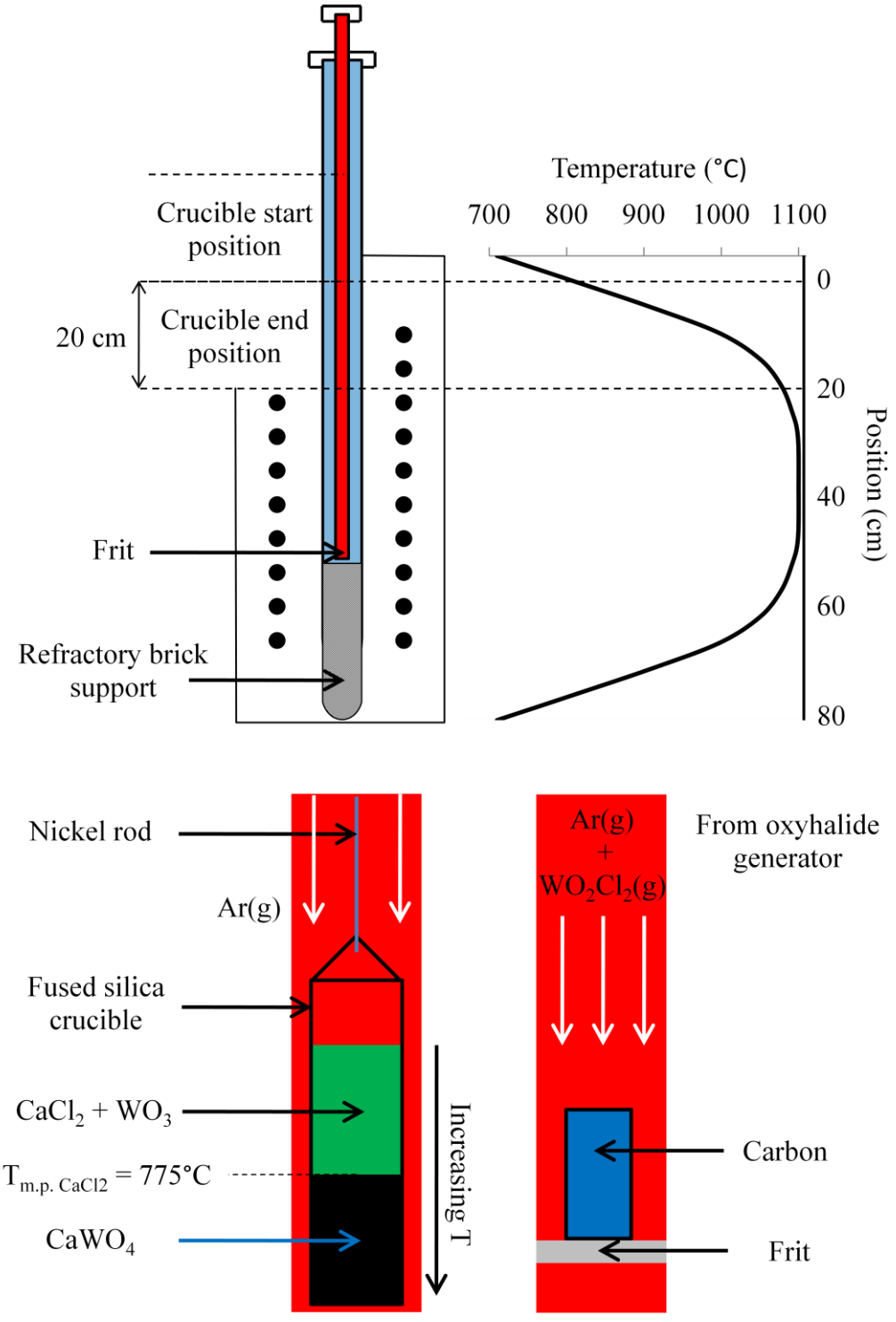

Figure 39: (Top) Furnace schematic and temperature profile (fused silica tube (red), mullite tube (blue), graphite foil liner not shown; (Bottom) Sections of the interior of the fused silica tube showing metal oxyhalide generator crucible (left) and carbon sitting atop frit (right).

The temperature profile above the uniform hot zone of the furnace used for carbon conversion trials is shown at a hot zone temperature of 1100°C. The fused silica crucible (99.99% purity, 18 mm OD x 150 mm length, Chemglass Life Sciences, Vineland NJ) packed with reactant powders was held 200 mm above the hot zone during heating and lowered to a final position such that the top of the crucible reached an equilibrium temperature of 850°C, thus ensuring that all $CaCl_2$ within the crucible melted (the melting point of $CaCl_2$ is 775°C[28]).

A powder mixture of $CaCl_2$ (anhydrous, 96.0% min. purity, Alfa Aesar, Ward Hill MA) and WO_3 (99.9% purity, -325 mesh, Atlantic Equipment Engineers, Bergenfield NJ) in 1:3 molar ratio was dry blended in air for 30 minutes in a high energy ball mill (Spex 8000M, Spex SamplePrep LLC). The weighed amount of $CaCl_2$ was adjusted based on an estimated 3.5 wt. % moisture content, as determined by TGA analysis at a heating rate of 10 K/min. (Figure 40):

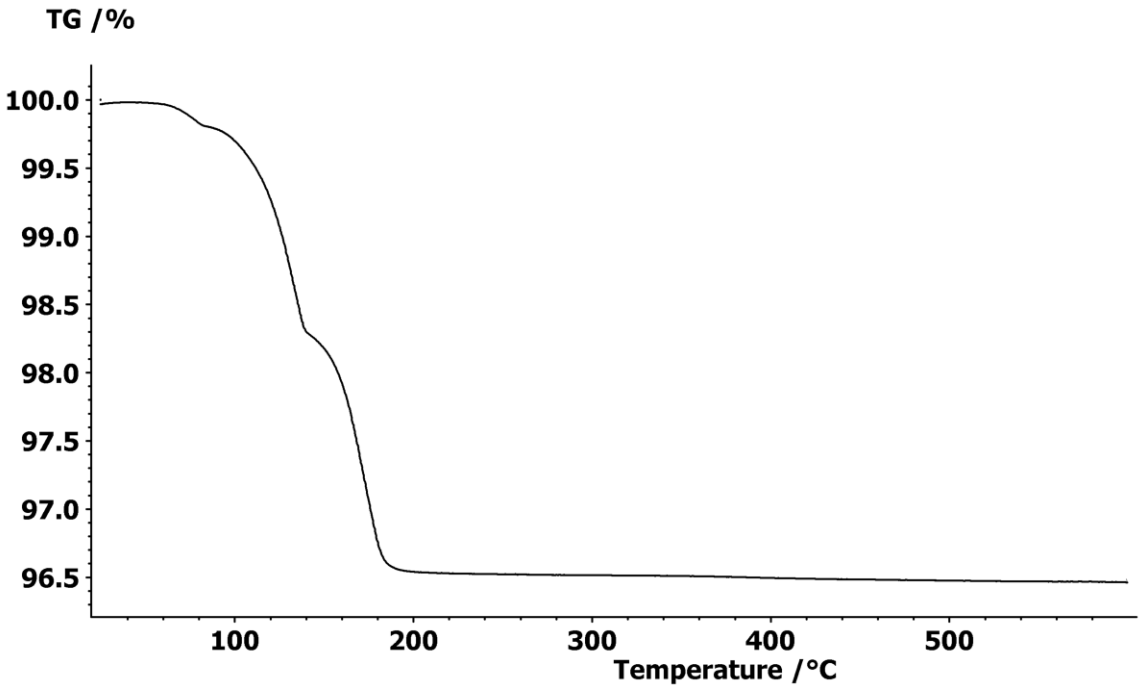

Figure 40: Weight loss of $CaCl_2$ under flowing oxygen-gettered argon

The mixture was suspended above the hot zone with a nickel rod in a fused silica crucible. A protective argon gas flow was maintained at a constant velocity of 0.10 cm/s for conversion of discontinuous, milled, unsized, amorphous carbon fibers (99% carbon content, 7.2 μm diameter x 150 μm average length, 1.75 g/cm^3 density, Panex 30, Zoltek Corp., St. Louis MO) and graphitic foams (99.99% carbon content, 0.90 g/cm^3 density, PocoHTC, Poco Graphite Inc., Decatur TX) and was configured such that the gas passed down the fused silica tube, around the suspended crucible, through the carbon substrate(s) and finally out to the mullite tube. The furnace was heated to 1100°C and the crucible was then lowered into the hot zone through a temperature gradient of 2°C/mm at a rate of 50 mm/hr. over a total distance of 200 mm to induce WO_2Cl_2(g) formation. Chemical yields were determined by static gravimetric measurements of the reactant-containing crucible and the carbon substrates.

Tungsten replicas were carbidized in CO(g) at 1100°C for up to 8 hours to produce WC-bearing replicas. W/WC fibers were blended at 20 vol. % with WC powder (99.9% purity, 5-6 μm average diameter, Global Tungsten & Powders Corp., Towanda, PA), subsequently uniaxially pressed to a peak pressure of 170 MPa and partially-sintered at 1400°C for 4 hours to 7.83 ± 0.01 g/cm^3 density. Partially-sintered WC-fiber bearing preforms were reactively infiltrated by immersion in molten Zr_2Cu contained within an MgO crucible at 1300°C for 1 hour. Upon cooldown, the reactively infiltrated parts were cross-sectioned parallel and perpendicular to the pressing axis for microstructural characterization. The extent of reaction was determined using quantitative XRD analysis using the calibration curve method described previously in Chapter 1.

Reacted carbon templates were characterized as described previously in Chapter 1 using a field emission gun scanning electron microscope equipped with energy dispersive x-ray spectroscopy detector, x-ray diffraction, high resolution transmission electron microscopy and by measurement of weight and bulk dimension changes. Chemical reaction yields estimated by static gravimetric measurements were calculated based upon the assumed stoichiometries of the proposed reactions.

2.3.2. Kinetic Trials

In order to determine the rate limiting kinetic mechanisms of reactive conversion of carbon to porous tungsten, graphite substrates in the shape of square prisms (6.25 ± 0.05 mm x 6.25 ± 0.05 mm x 22.2 ± 0.1 mm) were cut from fine grain isomolded graphite plates (Grade GM-10, 99.95% purity, 1.82 g/cm^3 @ 9% porosity, GraphiteStore.com) and oriented axially along the direction of gas flow atop a quartz frit held in place by means of a quartz pedestal base (Figure 41):

Figure 41: Schematic of graphite substrate (black) and holder (red) atop quartz frit (blue) used for kinetic study (not to scale)

For the purposes of kinetic analyses, it has been assumed that the pore network of the graphite substrate is inaccessible to the $WO_2Cl_2(g)$ reactant throughout the course of reactive conversion. This assumption is valid if the majority of the porosity is initially

closed or becomes closed as a result of reaction, and/or if the rate of diffusion of WO_2Cl_2(g) into this pore network is relatively slow compared to the reaction rate. Further work may be required to analyze the effects of pore structure on the reaction rate.

For a reaction temperature of 1100°C, and a fixed amount of *in-situ* generated reactant gas delivered (20.0 ± 0.5g WO_2Cl_2), experiments were conducted varying the inlet carrier gas velocity from 0.03-0.85 cm/s. Cross sections of reacted specimens cut by low-speed diamond wafering saw, vacuum infiltrated with epoxy, and polished to 6 μm finish were characterized by optical microscopy. The thicknesses of the product layers were measured by taking measurements at pre-set intervals as a function of distance from the leading edge on a montage consisting of high resolution optical images (Figure 42):

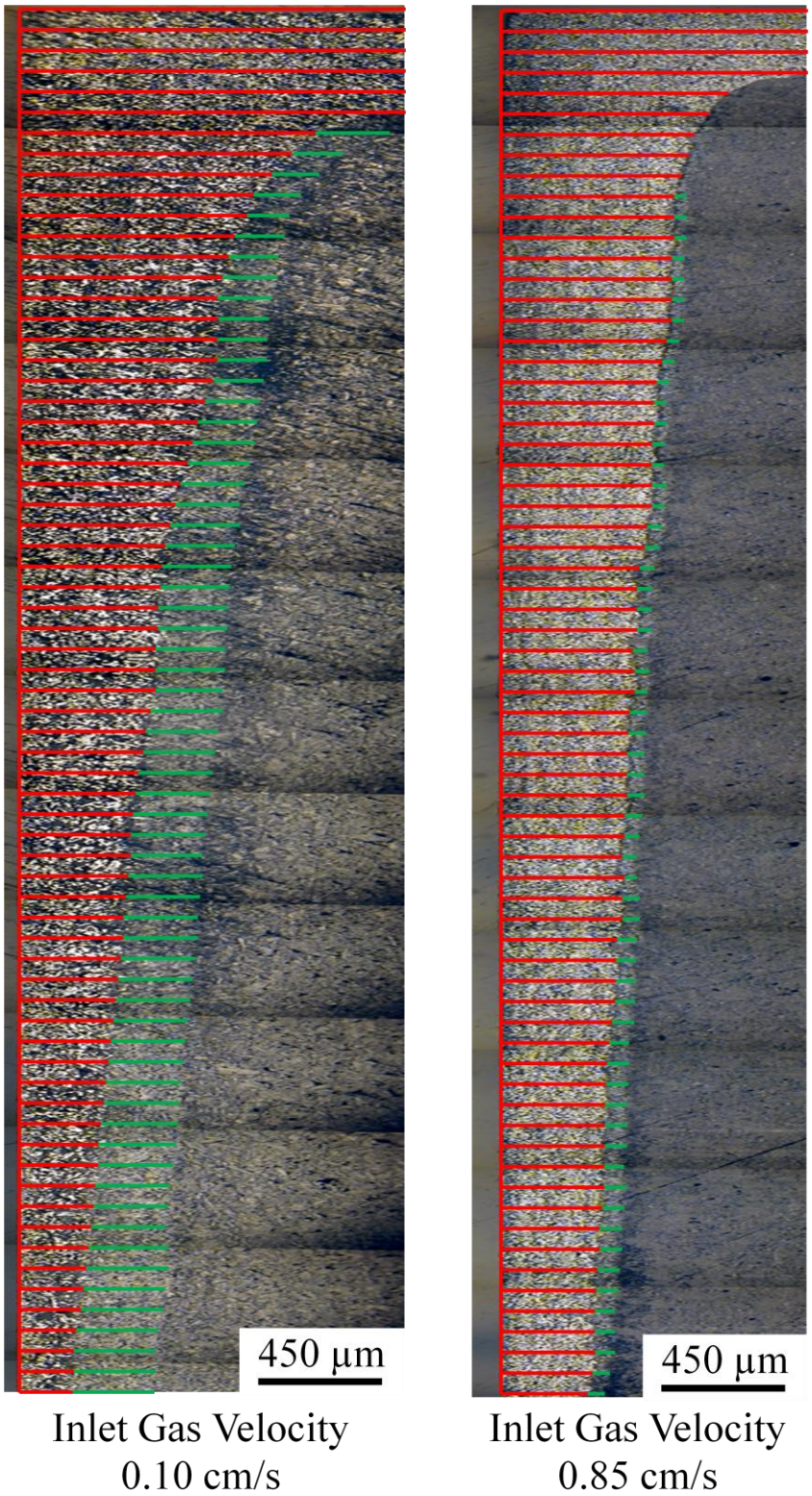

Figure 42: Cross section montage images with superposed thickness measurements of W (red) and WC (green) product layers.

The molar content of product layers formed on specimens reacted at varying inlet gas velocities were determined via a combination of x-ray diffraction analysis and static gravimetric analysis of specimen weight changes. Specimen weight measurements were taken prior to reaction, after reaction, and after complete chemical etching[75] of the W and WC product layers in a 30 vol. % hydrogen peroxide bath at 0°C for 24 hours. The extent of reaction as a function of exposure time to the WO_2Cl_2(g) reactant at 1100°C and a fixed inlet gas velocity of 0.85 cm/s was determined via static thermogravimetric measurement of the weight change of a specimen subjected to sequential identical exposures to WO_2Cl_2(g) reactant.

2.4. *Results*

2.4.1. Porous W/WC Replicas of Carbon Fibers and Graphitic Foam

Static gravimetric measurements of mixtures consisting of 8.0 g $CaCl_2$ (0.069 mol $CaCl_2$, accounting for 3.5 wt. % moisture) and 48.3 g (0.208 mol) WO_3 showed an average weight loss of 20.0 ± 0.5 g. If the weight loss is assumed to consist of the reaction-generated WO_2Cl_2(g) and 3.5 wt. % moisture content from $CaCl_2$, then the average weight loss corresponds to a loss of 0.3 g H_2O(g) and 19.7 g WO_2Cl_2(g) (0.069 mol WO_2Cl_2(g)), consistent with the expected overall weight loss from the reaction (2.6) taken to completion with WO_3 in excess:

$$CaCl_2 + 2WO_3 \leftrightarrow CaWO_4 + WO_2Cl_2(g) \quad (2.6)$$

Thermodynamic calculations (see Table 11) and XRD analysis (Figure 43) of product powders confirm the likelihood of reaction (2.6) as the primary cause of measured weight change:

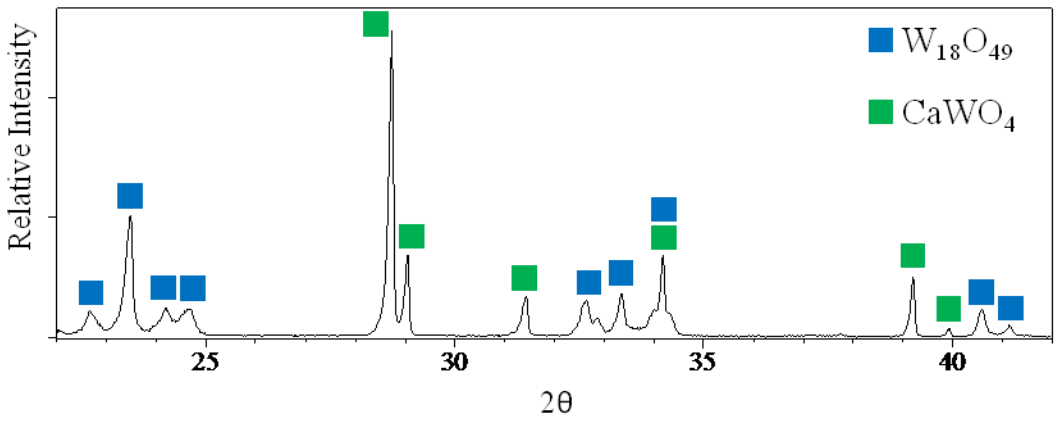

Figure 43: XRD analysis of reaction products after reaction of $CaCl_2$ and WO_3 at 1100°C for 6 hours (PDF Card No. for $W_{18}O_{49}$ 36-0101, $CaWO_4$ 41-1431)

Static thermogravimetric measurements (Figure 44) of the weight loss of the $CaCl_2/WO_3$-containing crucible resulted in the estimation of the average rate of $WO_2Cl_2(g)$ generation as 4.54×10^{-4} mol/min., assuming that weight loss is associated with the stoichiometry of reaction (2.6):

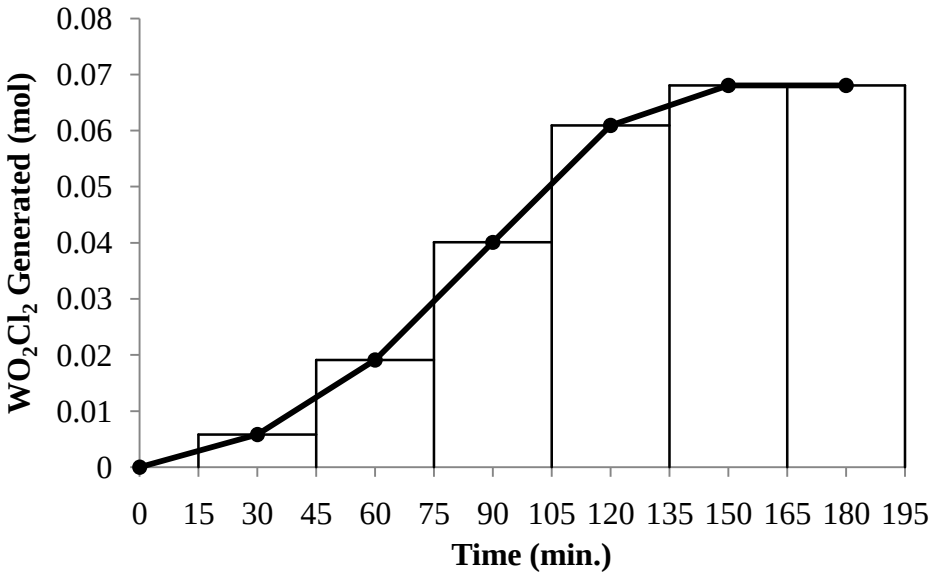

Figure 44: WO_2Cl_2(g) generation versus time, plotted from weight change measurements and assuming the reaction stoichiometry of equation (2.6)

Amorphous carbon fibers used as carbon templates are shown in Figure 45:

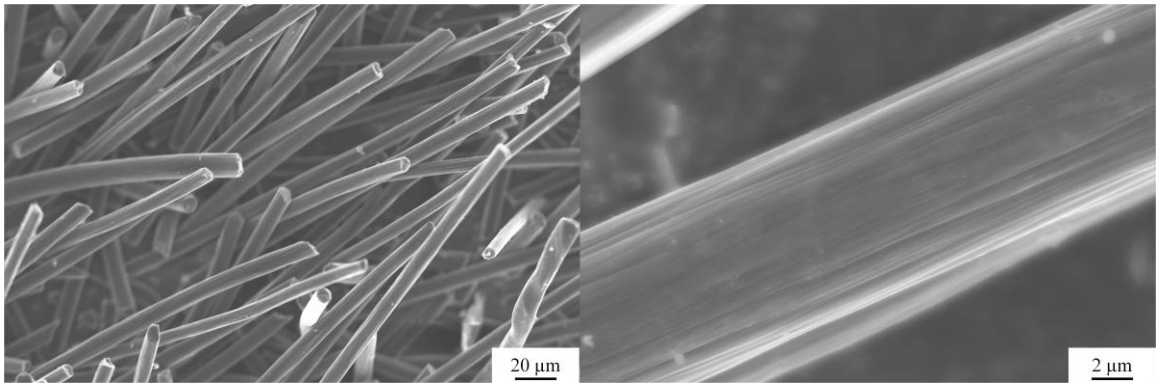

Figure 45: Zoltek Panex 30 milled carbon fibers

Carbon fibers partially reacted with *in situ* generated WO_2Cl_2(g) at 1000°C for 5 hours via reaction (2.7) show the presence of residual carbon with core-shell morphology (Figure 46):

$$4C + 3WO_2Cl_2(g) \leftrightarrow W + 2WOCl_3(g) + 4CO(g) \qquad (2.7)$$

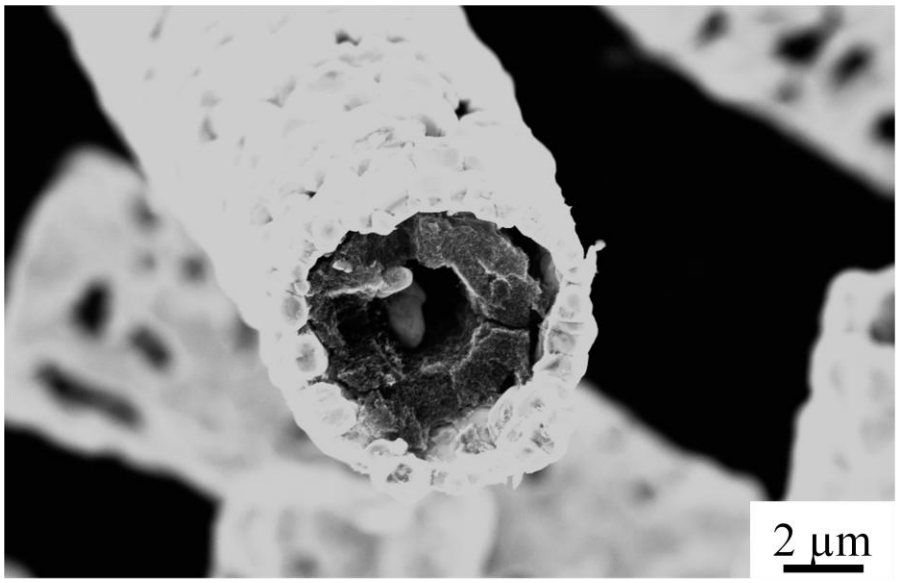

Figure 46: Partially reacted fiber (1000°C for 5 hours) showing carbon core and interior pore

The presence of an interior pore indicates outward diffusion of carbon to form tungsten either at the C/W (coupled with inward W diffusion) or W/gas interface.

Fully-converted fibers are shown in Figure 47:

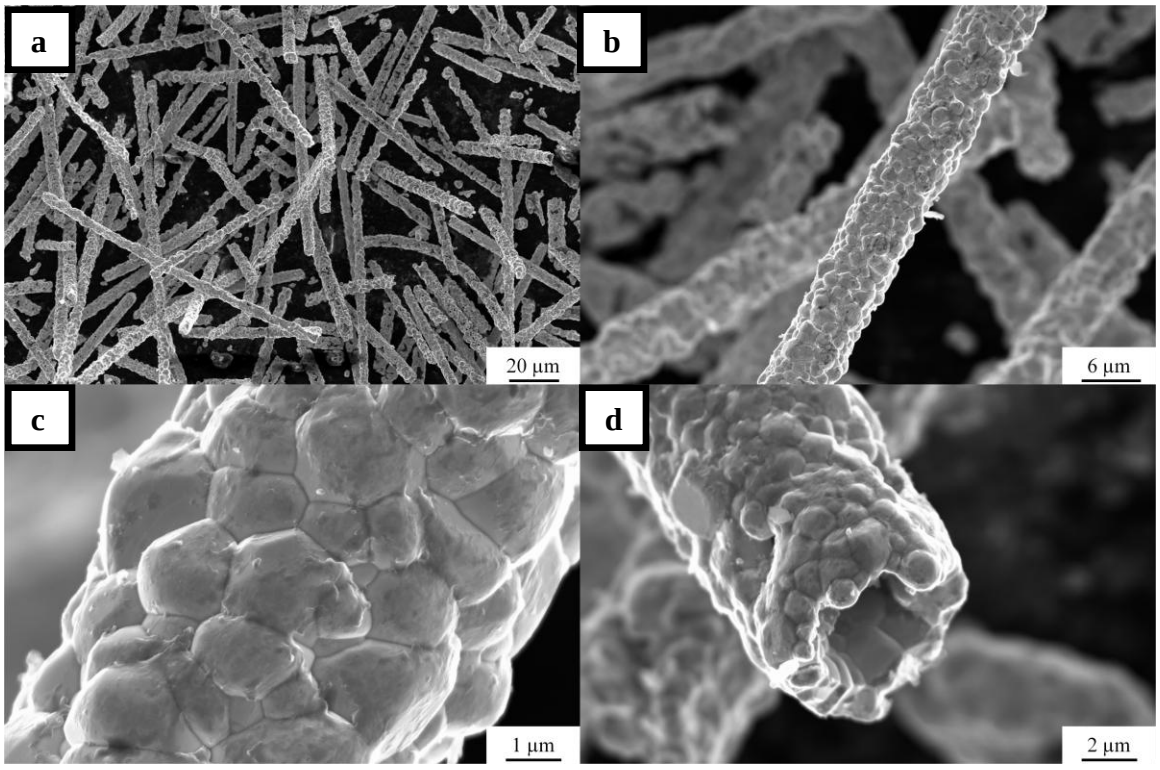

Figure 47: Tungsten fiber replicas via reaction with WO_2Cl_2(g) at 1100°C for 8 hours at an inlet carrier gas velocity of 0.10 cm/s

No residual carbon cores were detected. Fibers displayed both closed and open ends. It is believed that all converted fibers displayed a core-shell morphology as a result of outward carbon diffusion.

Carbidized W fibers are shown in Figure 48:

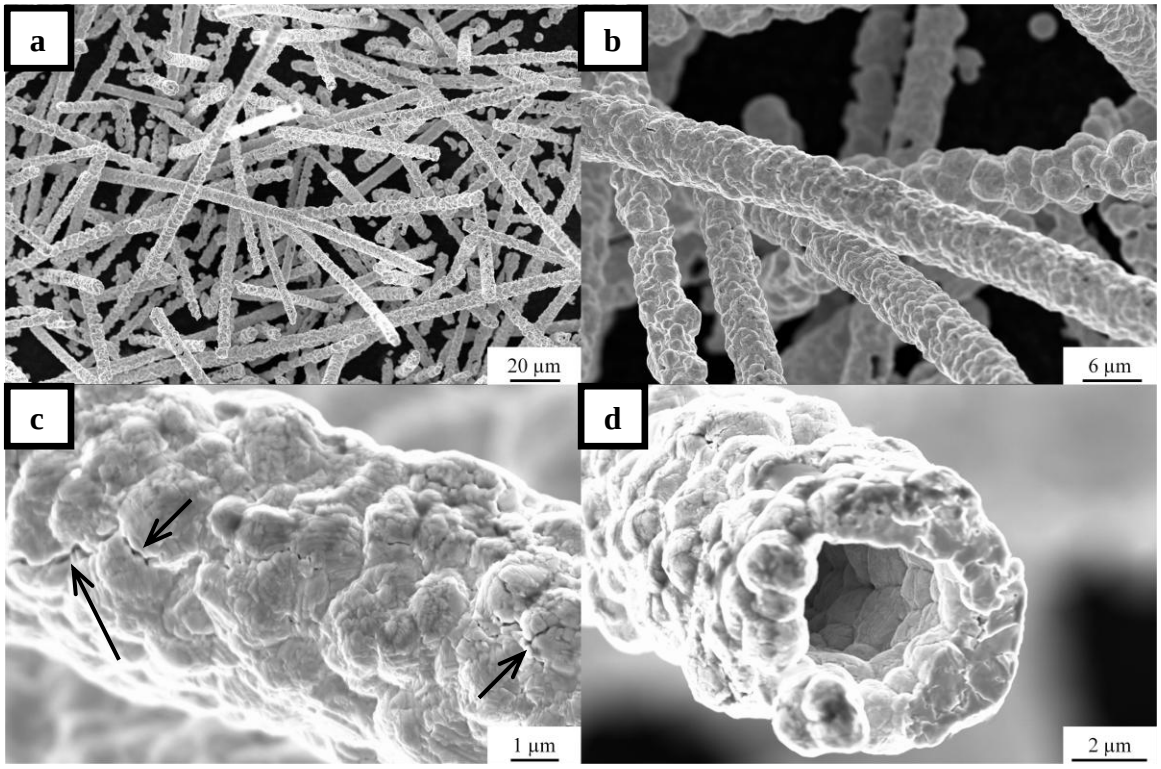

Figure 48: Tungsten carbide fiber replicas after CO(g) treatment of tungsten fiber replicas at 1000°C for 8 hours (microcracks indicated by arrows)

The presence of microcracks (Figure 48c) is likely a result of the solid molar volume change (+35.7%) of reaction:

$$W + 2CO(g) \leftrightarrow WC + CO_2(g) \tag{2.8}$$

XRD analyses confirmed that W (Figure 49) can be converted to WC (Figure 50) by CO(g) treatment:

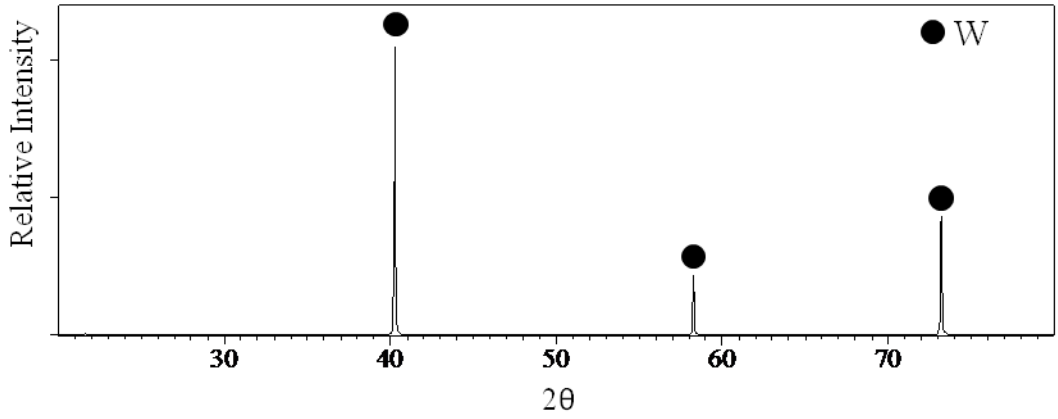

Figure 49: XRD analysis of W fibers (1100°C for 12 hours) (PDF Card No. 04-0806)

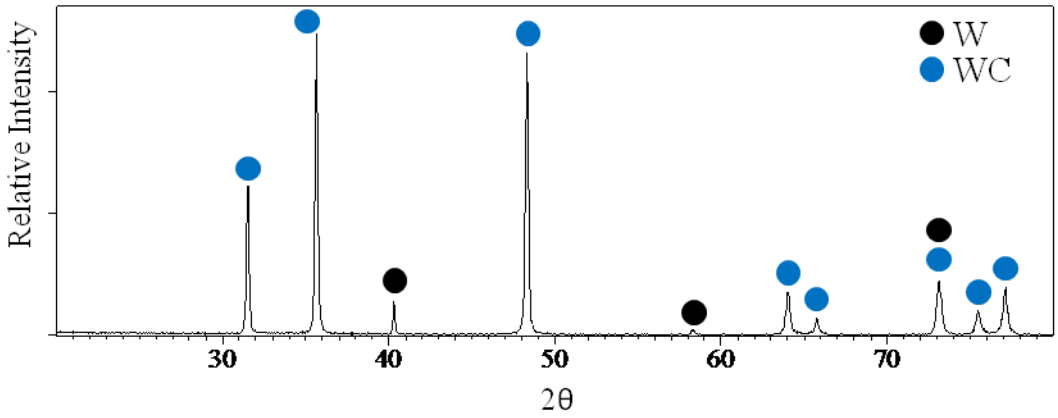

Figure 50: XRD analysis of W fibers after CO(g) treatment (1100°C for 8 hours) (PDF Card No.for W 04-0806, WC 25-1047)

The measured W(110):WC(100) peak area ratio of 0.079 obtained from Figure 50 corresponded to a molar phase content of 12% W and 88% WC using the calibration method described previously. It is unclear if this corresponded to the presence of W in each fiber (i.e. – that homogeneous reaction occurred throughout the sample), or, more likely, that diffusion-limited reaction caused large W grains (not present within the fibers) to be partially carbidized.

Cross sections of WC preforms incorporating WC/W fibers after DCP processing are shown in Figure 51:

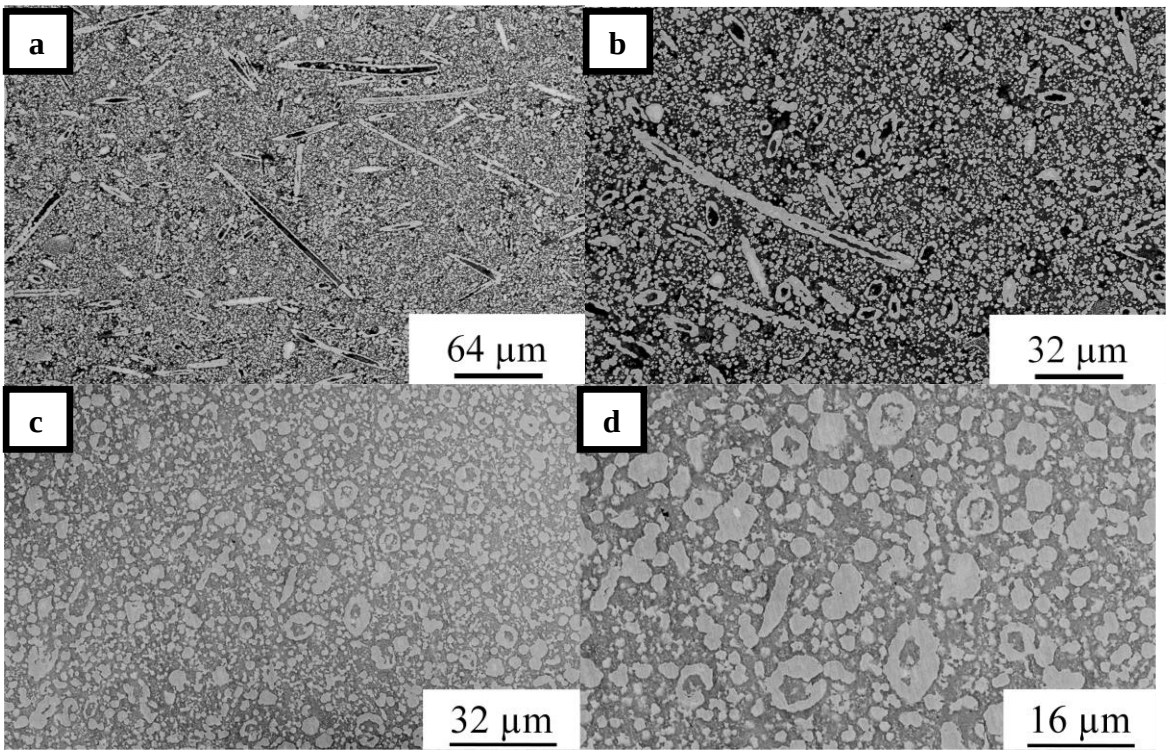

Figure 51: DCP infiltrated pellet (1300°C, 4 hours) with 20 vol. % WC fibers: (a) and (b) parallel to press direction; (c) and (d) perpendicular to press direction

Fibers were found to lie perpendicular to the direction of pressing with random in-plane orientation. Fibers with closed ends were not infiltrated, with the interiors remaining as voids in the final composite microstructure. Since it is known that the reaction between WC and Zr_2Cu is solid-state diffusion limited[76], it can be expected that differential degrees of conversion would arise – the larger diameter fibers taking longer to react than the smaller diameter particles. As a result, preforms containing WC/W fibers were found to be less reacted than for WC powder preforms, as evidenced by XRD analysis (Figure 52):

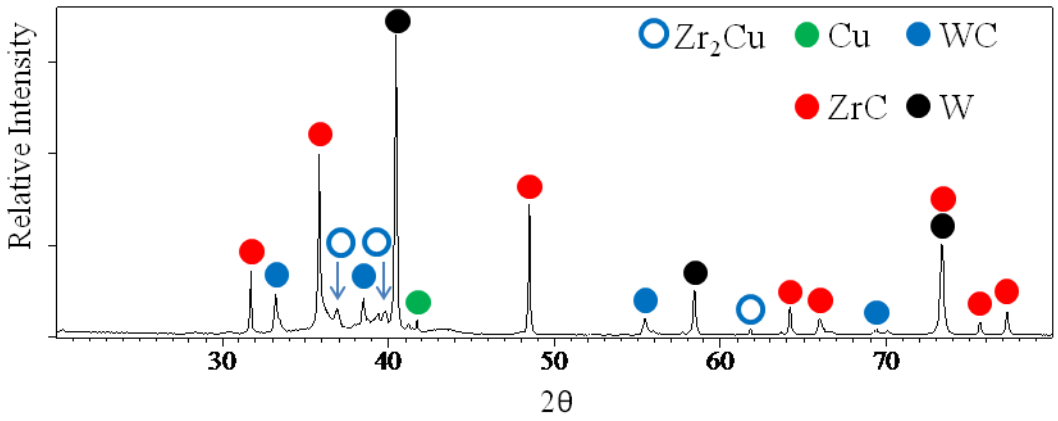

Figure 52: XRD analysis of a cross-section of a DCP infiltrated pellet (1300°C, 4 hours) with 20 vol.% WC fiber replicas (PDF Card No. for W 04-0806, Cu 04-0836, WC 25-1047, ZrC 35-0784, Zr_2Cu 04-004-2397)

On the basis of the measured W(110):WC(100) peak area ratio of 2.3 obtained from Figure 51 and the calibration curve method described previously, a W:WC molar ratio of 3.7 ± 0.3 has been calculated, corresponding to an extent of conversion of 79 ± 1%. However, this value may overestimate the extent of conversion, as some W may have been initially present (see Figure 50).

In addition to fibers, porous graphitic foams were converted into tungsten replicas. The measured exterior dimensions of the W-converted foam were within 1% of those of the graphitic PocoHTC foam, while bulk density (reported as the average and standard deviation of 10 sets of dimensional measurements) increased from 0.37 ± 0.01 g/cm^3 to 1.20 ± 0.01 g/cm^3 after conversion. Taking the theoretical bulk densities[29] of pure graphite as 2.265 g/cm^3 and tungsten as 19.259 g/cm^3 and assuming phase pure specimens, the densities of the foam specimens decreased from 17 ± 1% (for the starting material relative to pure graphite) to 6 ± 1% (for the reaction-product replica relative to pure tungsten). This decrease was consistent with the expected solid volume change upon reaction assuming the stoichiometry of reaction (2.7) ($\Delta V/V_0$ = -55.0%). The

microstructure of the starting foam was preserved after conversion (Figure 53, Figure 54, and Figure 55):

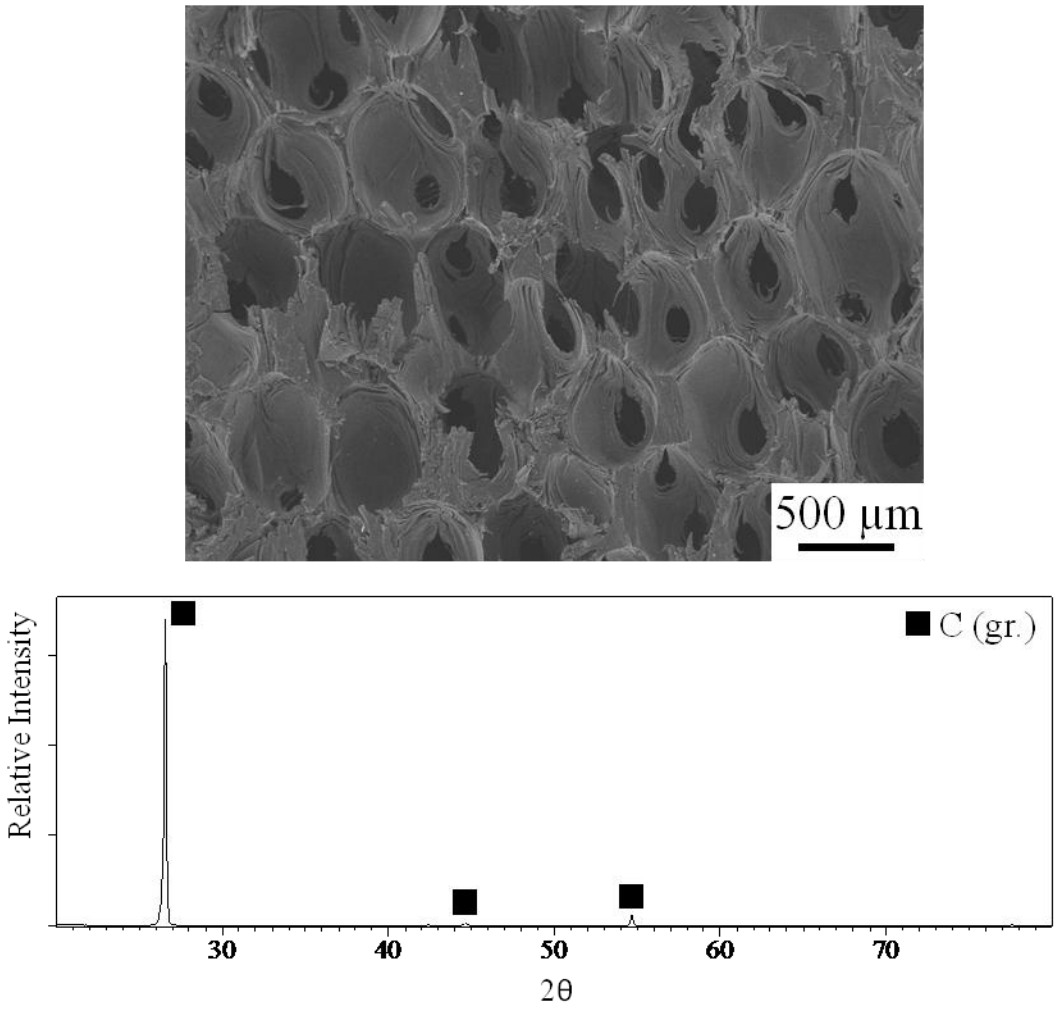

Figure 53: SEM and XRD analyses of starting graphitic PocoHTC foam (PDF Card No. 56-0159)

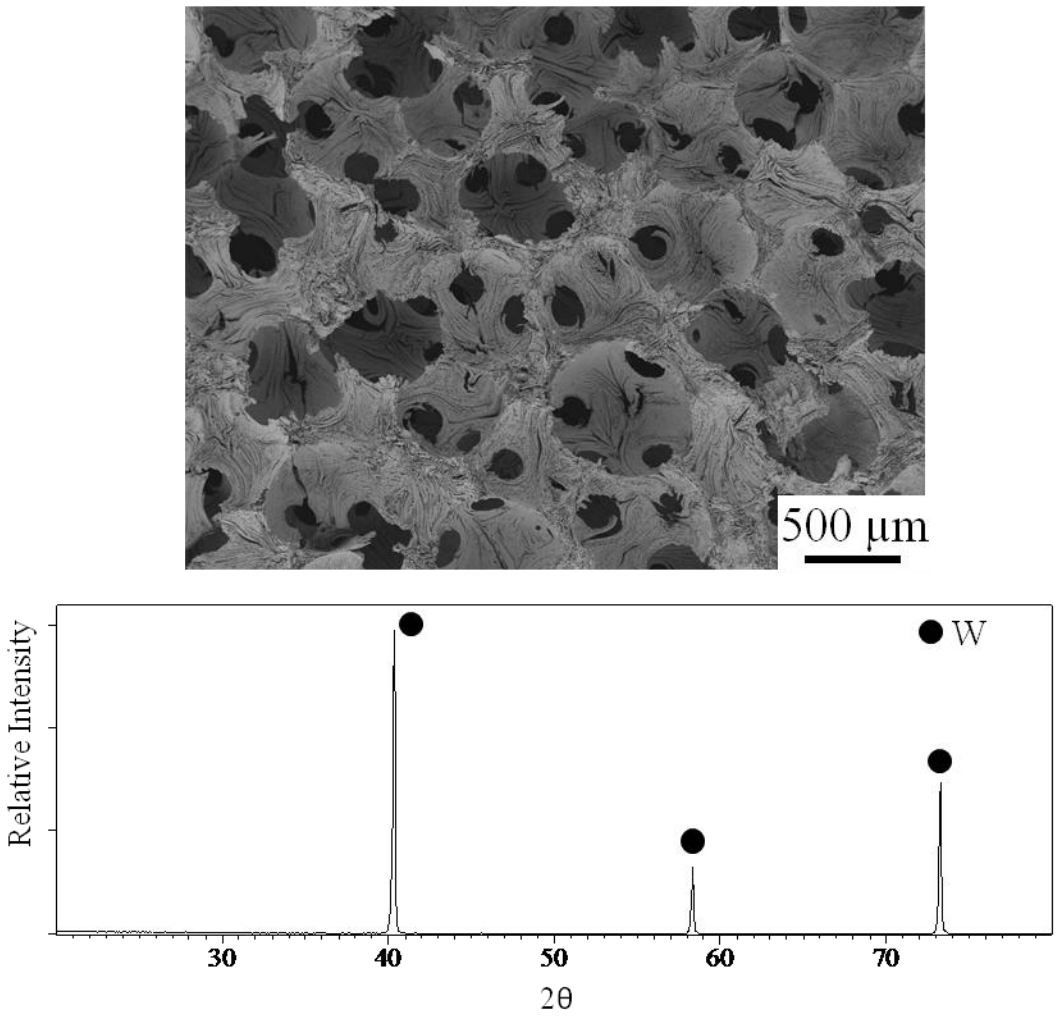

Figure 54: SEM and XRD analyses of W-converted foam replica (1100°C for 8 hours at an inlet carrier gas velocity of 0.10 cm/s) (PDF Card No. 04-0806)

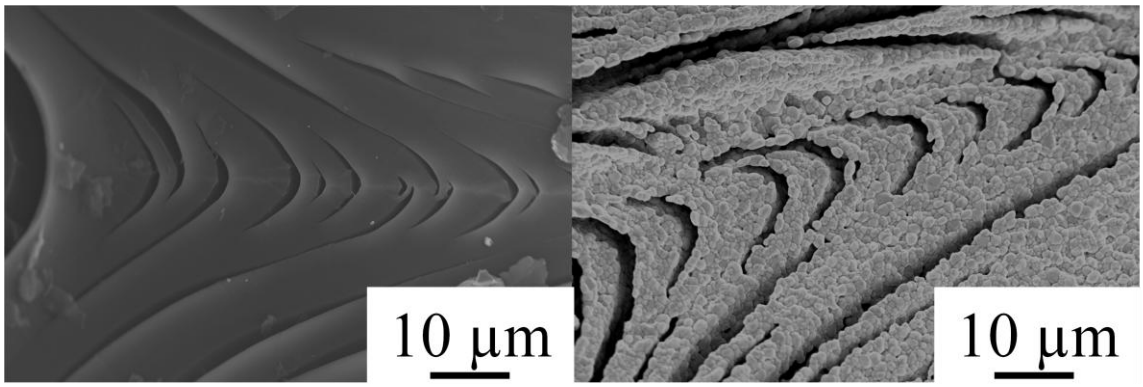

Figure 55: Fine feature preservation of graphitic (left) PocoHTC foam and (right) W-converted foam replica (1100°C for 8 hours at an inlet carrier gas velocity of 0.10 cm/s)

XRD (Figure 54) and HRTEM (Figure 56) analyses indicated that no residual carbon is detectable within the foams:

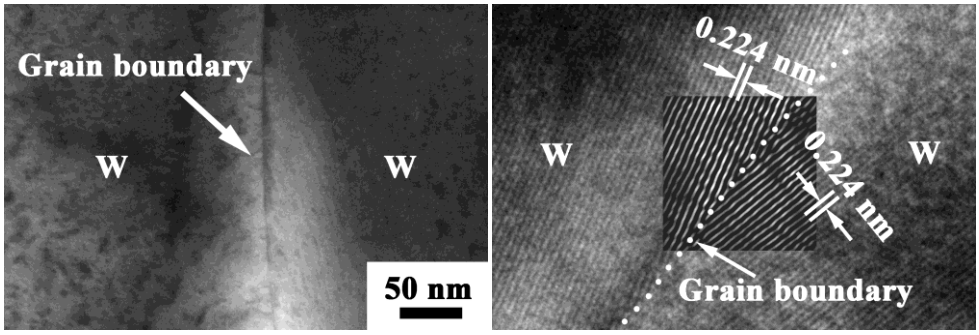

Figure 56: TEM and HRTEM images of W-converted foam replica (1100°C for 8 hours at an inlet carrier gas velocity of 0.10 cm/s) (Courtesy of Dr. Ye Cai)

Examination via SEM revealed that positive replicas were produced at the macroscale (i.e. – when the outward carbon diffusion distance is much less than the feature size) whereas negative replicas were produced at the microscale (i.e. – when the outward carbon diffusion distance is comparable to the feature size).

2.4.2. Reactive Conversion of Dense Graphite Substrates for Kinetic Study

The morphology of partially-reacted dense graphite substrates generated in kinetic studies consisted of a porous outer layer with a relatively dense inner layer (Figure 57):

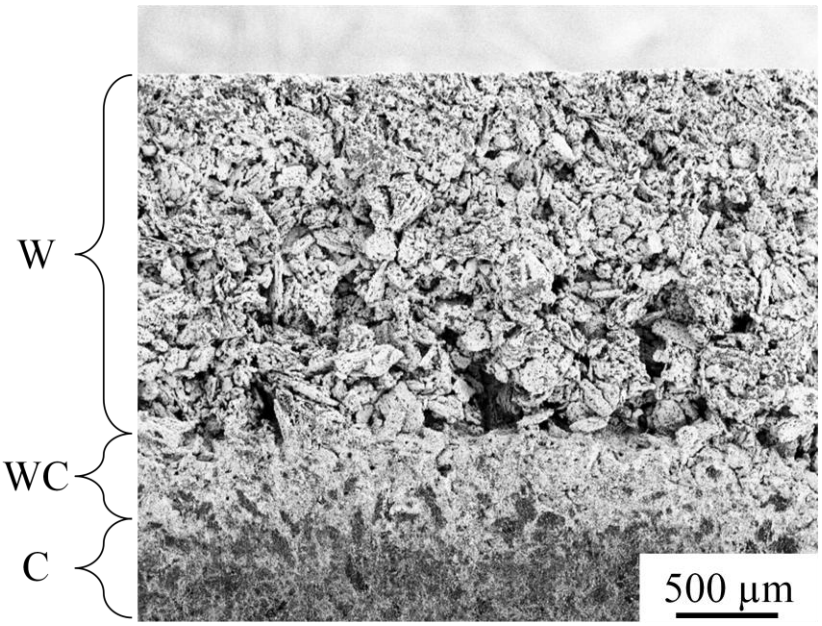

Figure 57: Representative SEM image of a cross-section of a partially reacted graphite substrate (1100°C for 8 hours at an inlet carrier gas velocity of 0.85 cm/s)

EDS analyses (Figure 58) indicated the presence of W in both layers with an increased content of carbon in the inner layer.

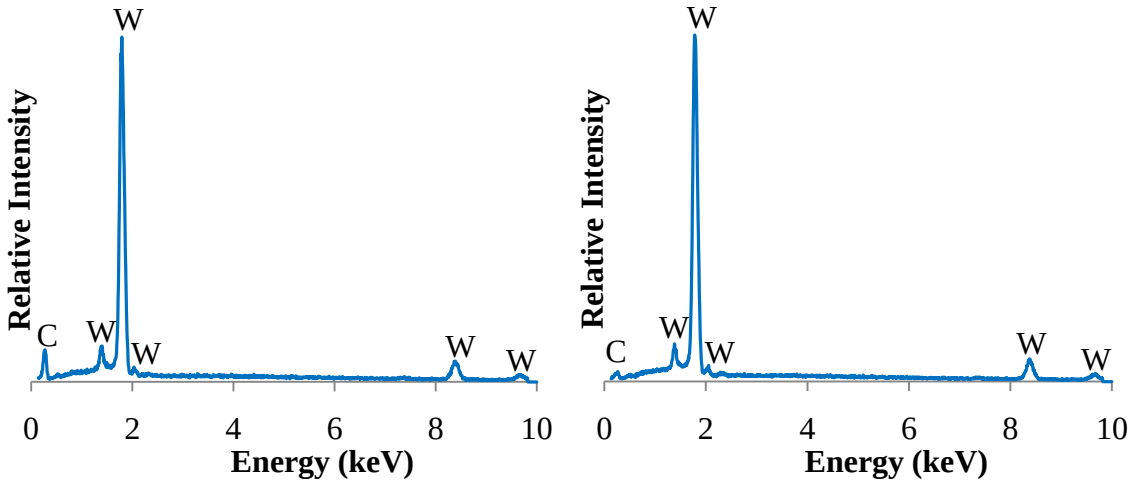

Figure 58: Representative EDS spectra of (left) WC inner layer and (right) W outer layer as seen in Figure 57

XRD analysis of a partially-reacted specimen revealed that, in the region fully-reacted through the thickness, only W was present (Figure 59), whereas, in locations adjacent to unreacted carbon, WC was also observed (Figure 60):

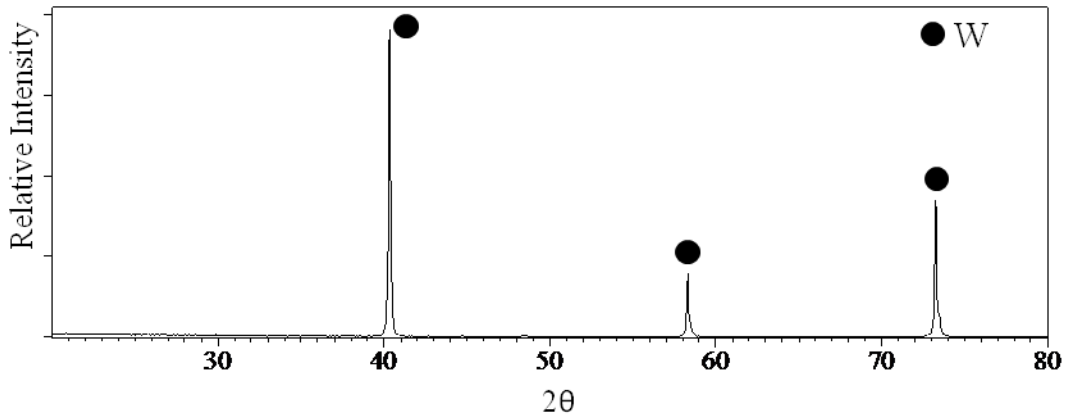

Figure 59: XRD analysis of graphite specimen in fully-reacted region (1100°C for 48 hours at an inlet carrier gas velocity of 0.85 cm/s) (PDF Card No. 04-0806)

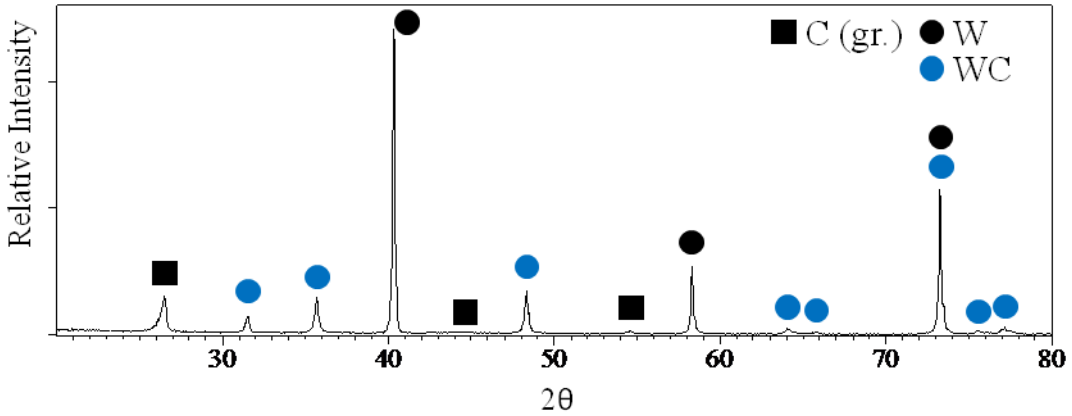

Figure 60: XRD analysis of graphite specimen in partially-reacted region (1100°C for 48 hours at an inlet carrier gas velocity of 0.85 cm/s) (PDF Card No. for W 04-0806, WC 25-1047, C(gr) 56-0159)

Therefore, it was concluded that the outer layer consisted of porous W while the inner layer adjacent to carbon consisted of WC. For a graphite specimen reacted fully through the thickness, the bulk density of the tungsten replica has been measured to be 6.92 ± 0.05 g/cm^3 (36.0 ± 0.2 % relative density), representing the median and range of ten sets

of measurements of the external dimensions and weight of the specimen. Additionally, since WC was not detectable anywhere in the cross-section of the fully-reacted region, it was postulated that WC existed as an intermediate phase during the reactive conversion of carbon under the conditions of the experiment (1100°C for a total of 48 hours at an inlet carrier gas velocity of 0.85 cm/s and average WO_2Cl_2 generation rate of $4.54x10^{-4}$ mol/min.).

Reaction kinetics as measured by cumulative weight change of a specimen at a fixed temperature (1100°C), inlet gas velocity (0.85 cm/s), and rate of WO_2Cl_2(g) generation ($4.54x10^{-4}$ mol/min.) are shown below (Figure 61):

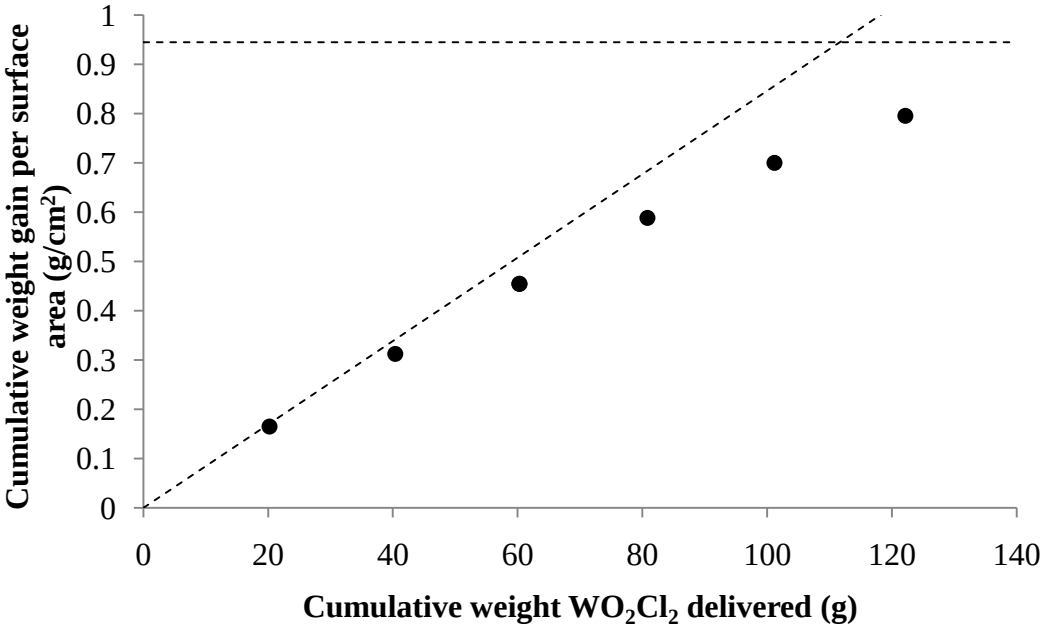

Figure 61: Weight gain kinetics versus theoretical maximum extent of reaction if all reactant gas or reactant substrate is consumed (1100°C at an inlet carrier gas velocity of 0.85 cm/s)

The horizontal dashed line represents the theoretical maximum weight change of the specimen assuming complete conversion by the expected reaction stoichiometry of reaction (2.7). For reference, the final data point in Figure 61 corresponds to 84.4 vol. % conversion of the sample. The diagonal dashed line represents the maximum theoretical

weight change due to reaction as a function of amount of WO_2Cl_2 delivered (i.e., the maximum extent of reaction at 100% theoretical yield).

Throughout reaction, minimal changes in the external dimensions of the carbon substrate were measurable. Width measurements (Figure 62) of a cross-section of a 84.4 mol. % reacted specimen after 48 hours exposure to WO_2Cl_2(g) generated at an average rate of $4.54x10^{-4}$ mol/min. at 1100°C and an inlet carrier gas velocity of 0.85 cm/s confirmed this observation:

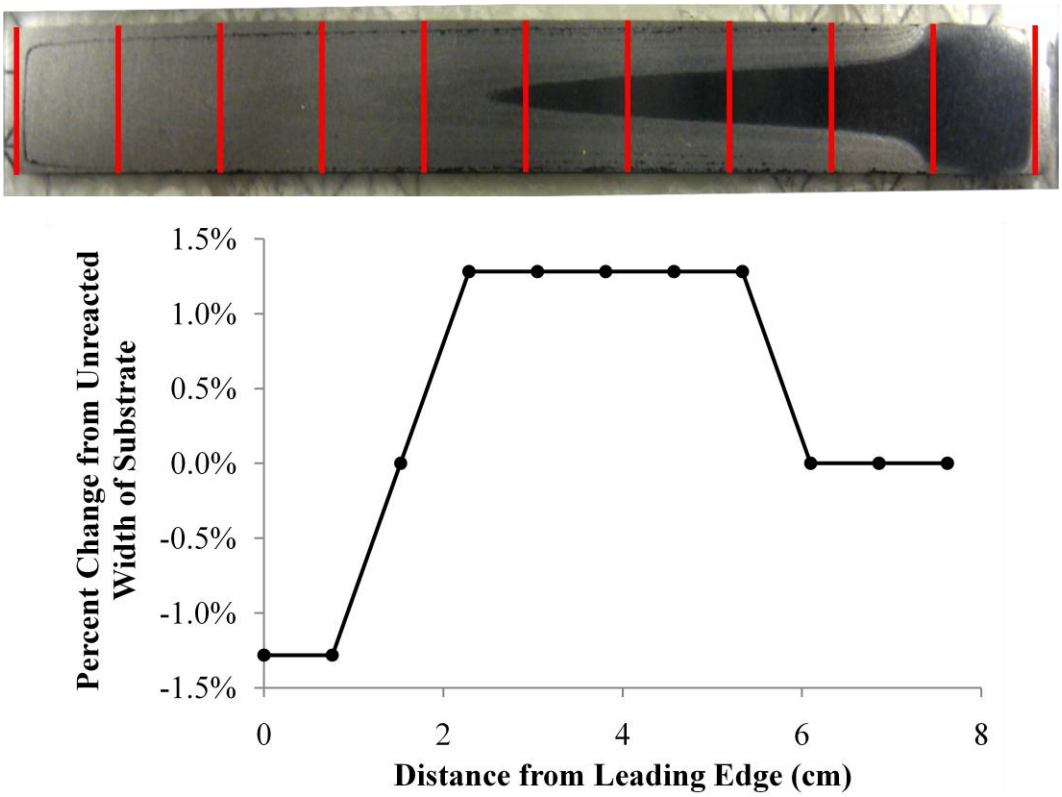

Figure 62: Cross-sectional width measurements of an 84.4 vol. % reacted specimen after 48 hours exposure to WO_2Cl_2(g) generated at an average rate of $4.54x10^{-4}$ mol/min. at 1100°C and an inlet carrier gas velocity of 0.85 cm/s

The reaction kinetics from weight change measurements in Figure 61 have been evaluated by plotting the square of the cumulative weight gain per surface area versus amount of reactant delivered (Figure 63):

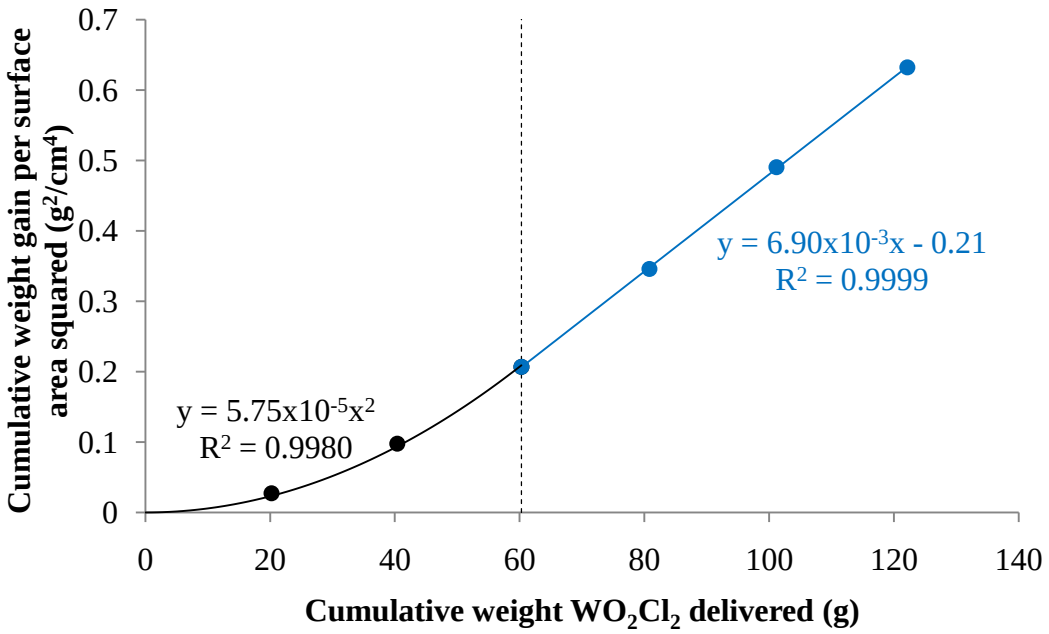

Figure 63: Square of weight gain kinetics showing transition from linear to parabolic kinetics (1100°C at an inlet carrier gas velocity of 0.85 cm/s)

The data appears to fit two kinetic regimes: a linear rate at low extents of reaction and a parabolic rate at larger extents of reaction, the transition occurring nominally at 50 vol. % conversion. It is important to note that the linear regime may have been a result of reactant starvation, as the recorded weight change corresponded to nearly complete yield.

Error bars stemming from measurements of changes of specimen weight and external surface area are too small to be visible in Figure 61 or Figure 63. The data points represent the progress of reaction for a single specimen consecutively exposed to WO_2Cl_2(g) under identical conditions of temperature, WO_2Cl_2(g) generation rate, and inlet carrier gas velocity. The linear and parabolic fits to the data are based on four points each, providing sufficient degrees of freedom to distinguish the trends from logarithmic, exponential, and other polynomial fits. However, a greater number of data points (which could be obtained by consecutive exposures of the specimen to smaller quantities of

WO_2Cl_2) would increase the present author's confidence in the observed transition from linear to parabolic reaction rates.

The weight gain of specimens reacted at inlet carrier gas velocities varying from 0.03 – 0.85 cm/s at 1100°C, and weight loss for the same specimens after complete chemical etching of the product layers, are plotted below (Figure 64):

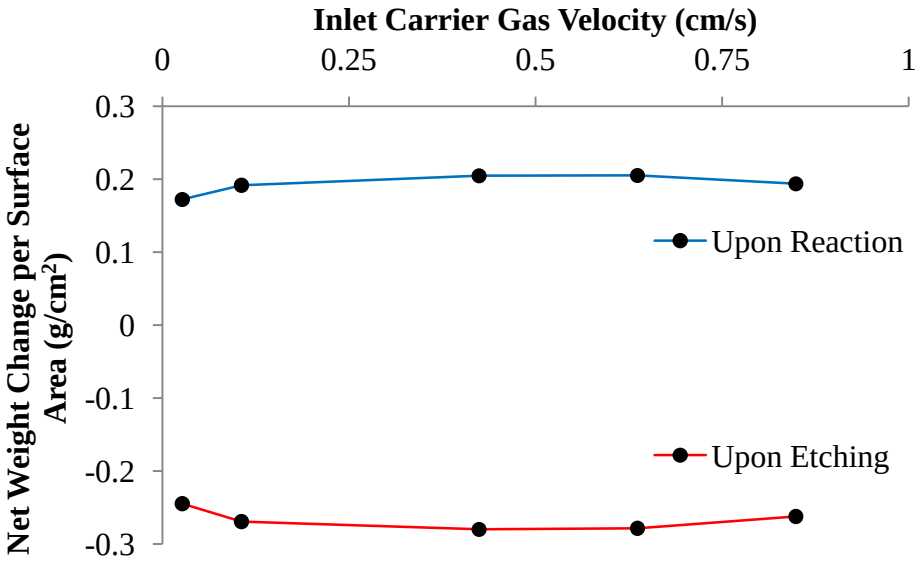

Figure 64: Weight change measurements of specimens after reaction (1100°C at an average WO_2Cl_2(g) generation rate of $4.54x10^{-4}$ mol/min.) and chemical etching as a function of inlet carrier gas velocity

The thicknesses of the W and WC product layers as a function of distance from the leading edge are plotted for inlet gas velocities of 0.10 cm/s and 0.85 cm/s (Figure 65):

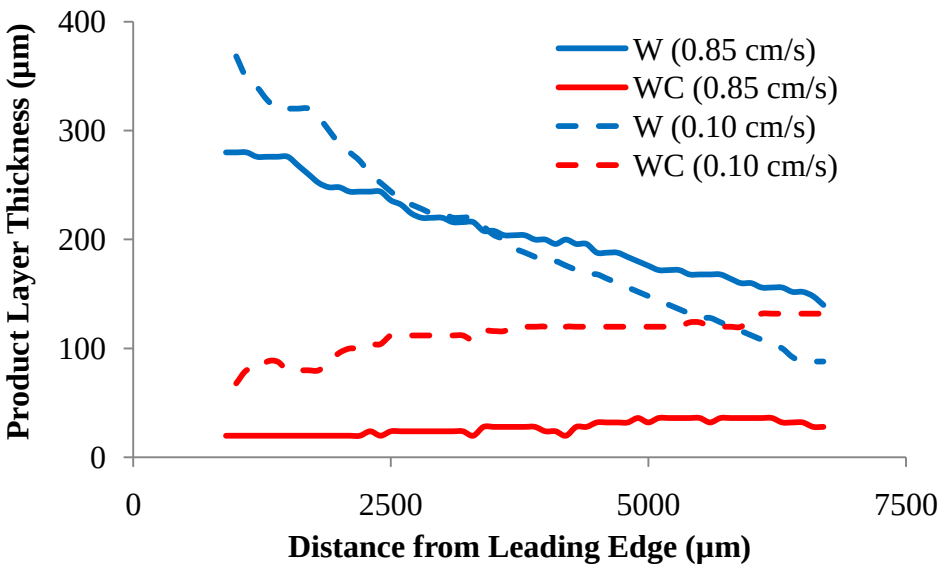

Figure 65: W and WC product layer thicknesses as a function of distance from the leading edge for inlet carrier gas velocities of 0.10 cm/s and 0.85 cm/s

At 0.10 cm/s and 0.85 cm/s inlet carrier gas velocities, the W product layer thickness was found to decrease, while the WC product layer was found to increase, with increasing distance from the leading edge. The WC product layer thickness was considerably less than that of the W layer at an inlet carrier gas velocity of 0.85 cm/s, while at an inlet carrier gas velocity of 0.10 cm/s, the WC product layer became thicker than that of W at a distance of approximately 5.8 mm from the leading edge. At all positions, the W:WC product layer thickness ratio was considerably higher at an inlet carrier gas velocity of 0.85 cm/s versus 0.10 cm/s.

2.5. *Discussion*

2.5.1. Thermodynamic Description of Gas-Solid Reactions

Metal replicas of carbon templates were thought to form via the following overall net reaction scheme:

$$\beta C + MO_u X_v(g) \leftrightarrow (1-\varepsilon)M + \varepsilon MO_y X_z(g) + \beta CO_r(g) \quad (2.9)$$

where M is a metal, X is a halide and assuming $y < u$ and substituting $\beta=(uz\text{-}vy)/(rz)$ and $\varepsilon=(v/z)$. For example, the fabrication of tungsten replicas may proceed via the reaction (2.7) where the standard Gibbs free energy change of reaction is -35.454 kJ per mol WO_2Cl_2(g) reacted at 1100°C and 2.36 bar pressure, which corresponds to the expected system pressure set by the inlet carrier gas pressure[70,77].

Data used for thermodynamic calculations have been reported with respect to a reference state of 1 bar pressure, which can be modified to account for the change in pressure according to the relation[78]:

$$\left.\frac{\partial G}{\partial P}\right|_T = \not{V} \quad (2.10)$$

where $\not{V}$ is molar volume. For condensed phases, the change in molar volume with pressure is small and so for condensed phases the standard Gibbs free energy of formation can be approximated to be constant with respect to pressure. For ideal gases, the molar volume varies with temperature and pressure according to the ideal gas law. Thus, the standard Gibbs free energy of formation for ideal gases varies with pressure is given by:

$$\Delta G_f^*(T, P_2) = \Delta G_f^0(T, 1\ bar) + RTln\left(\frac{P_2}{1\ bar}\right) \quad (2.11)$$

where ΔG^*_f refers to the standard Gibbs free energy change of formation at arbitrary pressure P_2 and ΔG^0_f refers to the standard Gibbs free energy change of formation at 1 bar pressure (as typically reported in thermochemical databases). For reactions between pure condensed phases and ideal gases, the standard Gibbs free energy change of reaction can therefore be calculated by[78]:

$$\Delta G^{*}_{rxn}(T, P_2) = \Delta G^{0}_{rxn}(T, 1\ bar) + \Lambda RT ln\left(\frac{P_2}{1\ bar}\right) \quad (2.12)$$

where Λ is the net change in number of moles of ideal gas due to reaction. Thus, for a reaction that results in a net increase in moles of gas ($\Lambda > 0$), the standard Gibbs free energy change of reaction increases with increasing pressure (i.e., the reaction becomes less favorable, in accordance with Le'Chatlier's principle).

The reaction between C and WO_2Cl_2(g) to produce W and $WOCl_3$(g) is more favorable than other reactions to produce W, as shown by the standard Gibbs free energy change of the following reactions (Table 10):

Table 10: Standard Gibbs free energy change for reactions between C and WO_2Cl_2(g) to produce W and/or W-bearing vapors at 1100°C and 2.36 bar pressure

Reaction	$\Delta G^{0}_{rxn\ @\ 1100C,\ 2.36\ bar}$ (kJ per mole WO_2Cl_2(g) reacted)
$4C + 3WO_2Cl_2(g) \rightarrow W + 2WCl_3O(g) + 4CO(g)$	-35.454
$4C + 2WO_2Cl_2(g) \rightarrow W + WCl_4(g) + 4CO(g)$	-10.245
$2C + WO_2Cl_2(g) \rightarrow WCl_2(g) + 2CO(g)$	-2.778
$3C + 2WO_2Cl_2(g) \rightarrow W + WOCl_4(g) + 3CO(g)$	49.913
$6C + 3WO_2Cl_2(g) \rightarrow 2W + WCl_6(g) + 6CO(g)$	60.917
$10C + 5WO_2Cl_2(g) \rightarrow 3W + 2WCl_5(g) + 10CO(g)$	63.504
$C + WO_2Cl_2(g) \rightarrow WCl_2O(g) + CO(g)$	110.836

These reactions have an interesting historical significance (see Appendix C). The first successful attempt to manufacture tungsten lamp filaments has been reported to have utilized a similar reaction to convert carbon lamp filaments into W by action of WO_2Cl_2(g) in a reducing atmosphere[79]; however, these efforts could not attain significant extents of conversion beyond a core-shell morphology around carbon filaments reported to be nominally 45 μm in diameter[80]. Complete conversion in the present case is likely made possible due to the high activities of WO_2Cl_2 in the gas stream produced by reaction (2.4) (see Table 11) that increases the favorability of reaction (2.7).

Table 11: Thermodynamic analysis of reactions of $CaCl_2$ with WO_3 to produce $CaWO_4$ and W-bearing vapors

Reaction	$\Delta G^0_{rxn\ @\ 800°C,\ 2.36\ bar}$ (kJ per mol W-bearing gas produced)	Equilibrium Activity of W-bearing Gas Product
$CaCl_2 + 2\ WO_3 \rightarrow CaWO_4 + WO_2Cl_2(g)$	-49.063	$2.45x10^{2}$
$1.5\ CaCl_2 + 2.5\ WO_3 \rightarrow 1.5\ CaWO_4 + WOCl_3(g) + 0.25\ O_2(g)$	26.767	$1.20x10^{-1}$
$2\ CaCl_2 + 3\ WO_3 \rightarrow 2\ CaWO_4 + WOCl_4(g)$	85.340	$7.01x10^{-5}$
$2\ CaCl_2 + 3\ WO_3 \rightarrow 2\ CaWO_4 + WCl_4(g) + 0.5\ O_2(g)$	214.314	$1.40x10^{-7}$
$3\ CaCl_2 + 4\ WO_3 \rightarrow 3\ CaWO_4 + WCl_6(g)$	173.183	$3.71x10^{-9}$
$CaCl_2 + 2\ WO_3 \rightarrow CaWO_4 + WCl_2O(g) + 0.5\ O_2(g)$	314.093	$8.06x10^{-11}$
$CaCl_2 + 2\ WO_3 \rightarrow CaWO_4 + WCl_2(g) + O_2(g)$	449.890	$1.12x10^{-11}$
$0.5\ CaCl_2 + 1.5\ WO_3 \rightarrow 0.5\ CaWO_4 + WO_2Cl(g) + 0.25\ O_2(g)$	311.405	$9.83x10^{-13}$
$0.5\ CaCl_2 + 1.5\ WO_3 \rightarrow 0.5\ CaWO_4 + WOCl(g) + 0.75\ O_2(g)$	599.255	$2.42x10^{-17}$

To facilitate scalability, a low-cost method to generate metal oxyhalides has been utilized following the overall reaction scheme:

$$(v/2)RX_2 + (1 + v/\alpha)MO_y \leftrightarrow (v/\alpha)R_{\alpha/2}MO_{1+y} + MO_uX_v(g) \qquad (2.13)$$

where R is preferably an alkaline earth metal, X is a halide, and substituting $\alpha = v/(y-u)$. For example, the generation of tungsten dioxide dichloride vapors from a mixture of $CaCl_2$ and WO_3 proceeds via the reaction (2.4).

This process represents a significant improvement over existing high-yield methods to produce $WO_2Cl_2(g)$, such as the reaction of WCl_6 with WO_3 in a sealed silica tube[81] or the reaction of $WOCl_4$ with hexamethyldisiloxane refluxed in petroleum ether[82]. Unlike tungsten halides and oxyhalides, $CaCl_2$ and WO_3 are low cost, non-volatile reagents that do not decompose by reaction with oxygen or moisture in air (i.e., while hydrates of these compounds may form, they do not readily decompose into oxides or

carbonates). Additionally, the thermodynamic selectivity of WO_2Cl_2(g) production (see Table 11) eliminates the need for vapor phase distillation of reaction products. Recent investigations into the electroreduction of tungsten-containing ore in molten salts[83,84] have recognized the thermodynamic favorability of this reaction, but, to the present author's knowledge, this is the first time it has been utilized to purposefully generate the volatile gas for use as a reactant.

Tungsten is not the only possible condensed reaction product between C and WO_2Cl_2(g), as the formation of WC can also be favorable via the following reaction:

$$5C + 3WO_2Cl_2(g) \leftrightarrow WC + 2WOCl_3(g) + 4CO(g) \tag{2.14}$$

where the standard Gibbs free energy change of reaction is -47.141 kJ per mol WO_2Cl_2(g) reacted at 1100°C and 2.36 bar pressure[28,77].

The relative stability of W and WC can be represented by the reaction:

$$4WC + 3WO_2Cl_2(g) \leftrightarrow 5W + 2WOCl_3(g) + 4CO(g) \tag{2.15}$$

having an equilibrium constant represented by:

$$K_C = \frac{a_W^5 a_{WOCl3}^2 a_{CO}^4}{a_{WC}^4 a_{WO2Cl2}^3} = \frac{16 a_{WOCl3}^6}{a_{WO2Cl2}^3} \tag{2.16}$$

where gases are assumed to be ideal and condensed phases are in equilibrium and in their pure, solid reference states such that $a_W = a_{WC} = 1$ and assuming $WOCl_3$(g) and CO(g) are generated solely by reactions (2.9) and (2.10) such that $a_{CO} = 2a_{WOCl3}$. The stability thresholds for the reaction of C in an atmosphere containing WO_2Cl_2(g) and $WOCl_3$(g) to produce W and WC at 1100°C is shown graphically below (Figure 66):

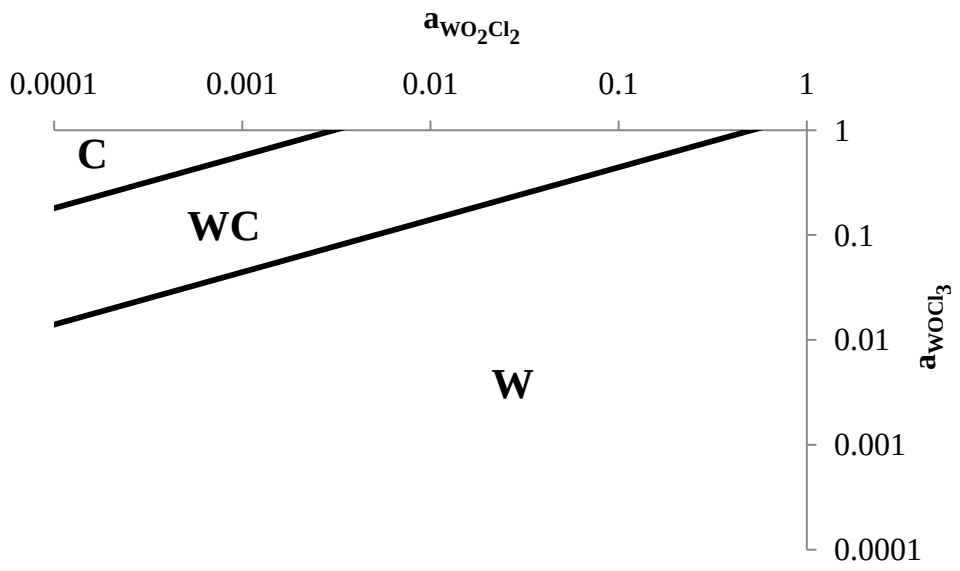

Figure 66: WC/W stability threshold in a reactive atmosphere containing WO_2Cl_2(g) and $WOCl_3$(g) at 1100°C

As the local activity of WO_2Cl_2(g) increases, so too does the $WOCl_3$(g) activity threshold for which WC is stable. This is in accordance with Le'Chatlier's principle, which predicts that an increase in WO_2Cl_2(g) activity relative to $WOCl_3$(g) activity would drive reaction (2.15) away from WC and towards W. Therefore, for a system in which the activities of these gases vary, thermodynamics predicts a shift in the relative stability of W and WC reaction products.

For an open-flow reactor where the rate of consumption of reactant is faster than the rate of supply, the local activity of WO_2Cl_2(g) at the gas/solid interface continually decreases while the local activity of $WOCl_3$(g) increases. Therefore, as the reactive gas stream consisting initially of Ar(g) and WO_2Cl_2(g) flows past the sample, a transition from W to WC as the stable reaction product with distance from the leading edge is possible.

Such a transition has also been observed in the composition of the reaction scale as a function of inlet gas velocity. The composition of the product layer has been determined in the following manner. Assuming that:

- the product layer consists entirely of W and WC such that $Y_{WC} + Y_W = 1$, where Y_k is the mole fraction of phase k in the product layer,
- etching fully dissolves all W and WC, and
- reactions (2.7) and (2.14) dominate W and WC formation such that the reaction stoichiometry (Σ), as defined by:

$$\Sigma = \frac{n_{C,CO}}{n_W + n_{WC}} \tag{2.17}$$

  is fixed at $\Sigma = 4$,

then, the composition of the product layers can be determined in the following way. Let Δm_{rxn} and Δm_{etch} be the weight change of the specimen upon reaction and upon etching, respectively, and are given by the following expressions:

$$\Delta m_{rxn} = m_W + m_{W,WC} - m_{C,CO(g)} \tag{2.18}$$

$$\Delta m_{etch} = m_W + m_{WC} \tag{2.19}$$

where m_k is the mass gain as phase k, $m_{C,CO(g)}$ is the mass loss of carbon from the sample as CO(g) and $m_{W,WC}$ is the mass gain of W as WC (the carbon in WC, being from the substrate, does not incur a change in mass). Substituting molar quantities yields:

$$\begin{aligned} \Delta m_{rxn} &= n_W AW_W + n_{WC} AW_W - n_{C,CO(g)} AW_C \\ &= (n_W + n_{WC}) AW_W - n_{C,CO(g)} AW_C \end{aligned} \tag{2.20}$$

$$\Delta m_{etch} = n_W AW_W + n_{WC}(AW_W + AW_c) = (n_W + n_{WC}) AW_W + n_{WC} AW_C \tag{2.21}$$

where AW_j is the atomic weight of element j and n_k is the number of moles of phase k. Taking the ratio of (2.20) and (2.21), and dividing out the terms $AW_W(n_W + n_{WC})$ and AW_C yields the following simplified expression:

$$\frac{\Delta m_{rxn}}{\Delta m_{etch}} = \frac{1 - \frac{AW_C}{AW_W}\Sigma}{1 + \frac{AW_C}{AW_W}Y_{WC}} \tag{2.22}$$

From Y_{WC} obtained via equation (2.22), the total number of moles of WC can also be readily calculated by modification of expression (2.21):

$$n_{WC} = \frac{\Delta m_{etch} Y_{WC}}{AW_W + AW_c Y_{WC}} \tag{2.23}$$

Such calculations have been performed on reacted samples as a function of flow rate (Figure 67 and Figure 68):

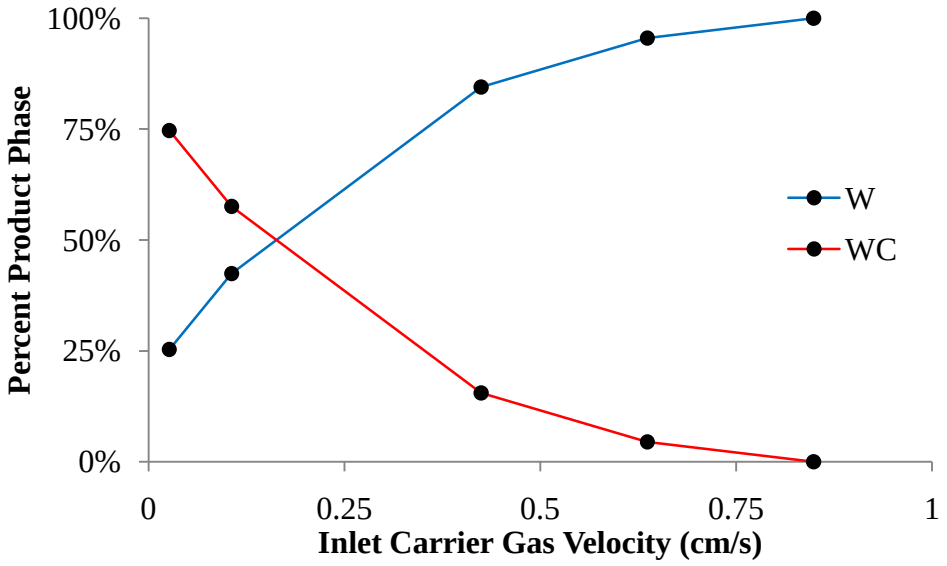

Figure 67: Mole fractions W and WC in product layer assuming reaction stoichiometry of 4:1.

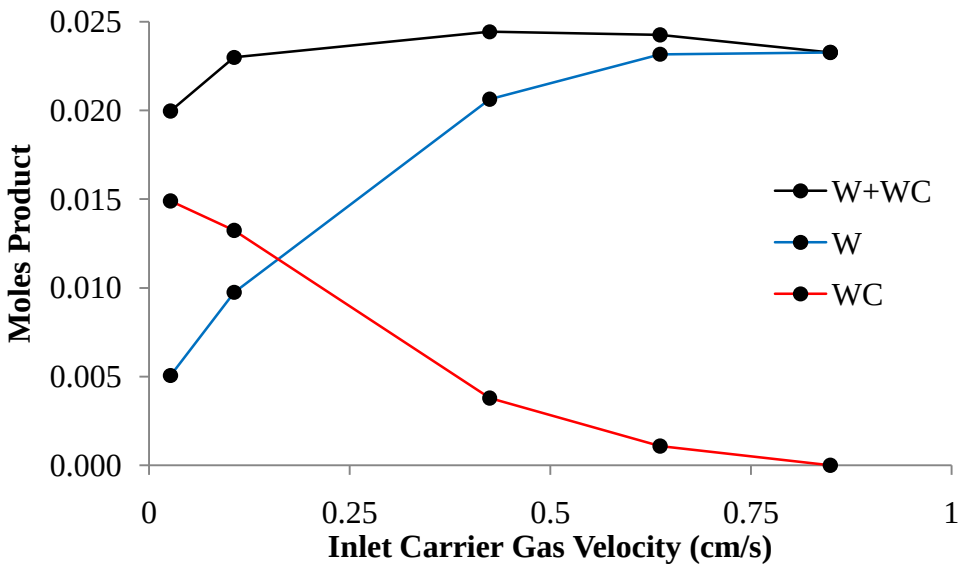

Figure 68: Moles W and WC in product layer assuming reaction stoichiometry of 4:1.

The observed trend is in agreement with thermodynamic and kinetic predictions. Consider an ideal gas mixture consisting of pure ideal gases in an open flow system at constant pressure and temperature where the time derivative of the ideal gas law is:

$$\frac{d}{dt}(PV) = P\dot{V} = \frac{d}{dt}(nRT) = \dot{n}RT \tag{2.24}$$

$$p_j\dot{V} = \dot{n}_j RT \tag{2.25}$$

where the activity of specie *j* in the gas phase is given by:

$$a_j = \frac{\dot{n}_j}{\dot{n}_{total}} \tag{2.26}$$

Then, for a two-component mixture consisting of Ar carrier gas and *in-situ* generated WO_2Cl_2(g) (i.e., the initial state of the reactive gas stream prior to reaction), the relationship between inlet gas velocity and WO_2Cl_2 activity is given by:

$$a_{WO2Cl2,i} = \frac{\dot{n}_{WO2Cl2,i}}{\dot{n}_{WO2Cl2,i} + \dot{n}_{Ar,inlet}} \tag{2.27}$$

where the inlet Ar carrier gas molar flowrate is given by:

$$\dot{n}_{Ar,inlet} = \left(\frac{P\dot{V}}{RT}\right)_{Ar,inlet} = A_{reactor}\left(\frac{Pu}{RT}\right)_{Ar,inlet} \quad (2.28)$$

where u is inlet carrier gas velocity and $A_{reactor}$ is the cross-sectional area of the reactor normal to the direction of flow. Thus, as inlet carrier gas velocity increases, $WO_2Cl_2(g)$ activity decreases (or, in other words, the concentration of WO_2Cl_2 is diluted by flowing greater amounts of Ar over the reactant crucible).

In order to predict the relative stabilities of W and WC reaction products, the local activities of $WO_2Cl_2(g)$ and $WOCl_3(g)$ must be modeled. Consider the following steps that must occur in order for the reaction to proceed (Figure 69):

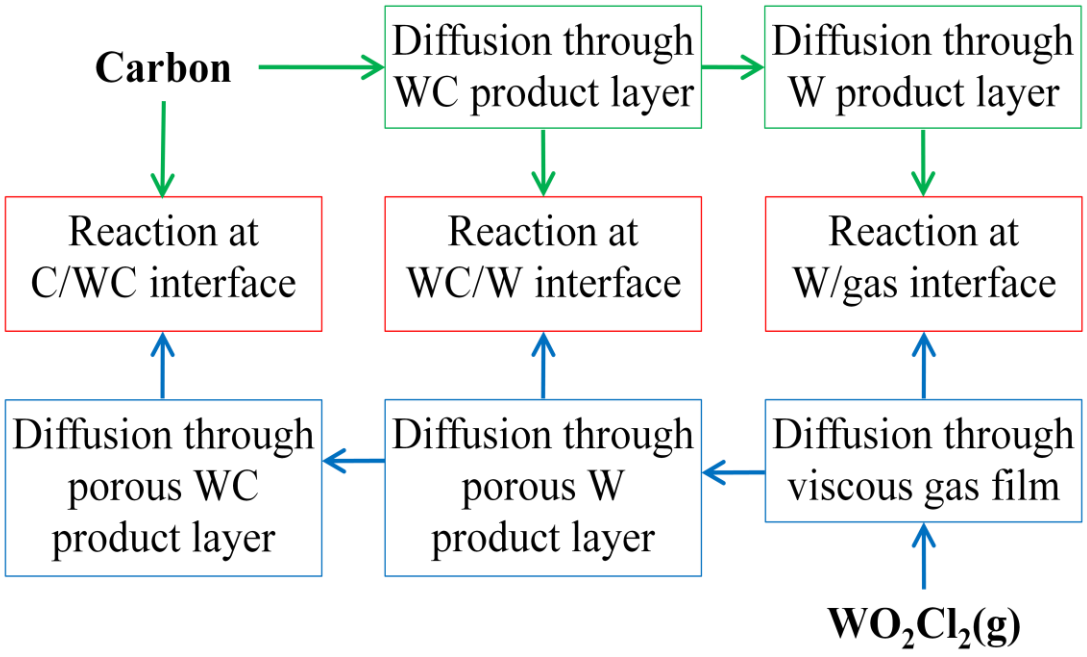

Figure 69: Schematic of possible rate determining steps

Carbon must diffuse outward through the WC and/or W product layers in order to react at either the WC/W interface or the W/gas interface, respectively, while $WO_2Cl_2(g)$ must diffuse through a viscous gas film (that develops as a result of frictional resistance between the substrate and flowing gas stream) and/or porous W product layer and/or

porous WC product layer to react at the W/gas interface, WC/W interface or C/WC interface, respectively. The kinetic rate limiting mechanism is characterized as the fastest parallel path within the slowest serial step. For example, suppose diffusion of C through the WC product layer is slower than either the rate of chemical reaction at the reaction interface or the rate of $WO_2Cl_2(g)$ diffusion and also suppose that C is able to diffuse rapidly along WC grain boundaries relative to through the bulk WC lattice - representing parallel pathways for C diffusion through WC; then C diffusion through the WC product layer along WC grain boundaries would be said to be the rate determining step.

Assuming that the rate-determining step is considerably slower than all other steps, the local equilibrium at the reaction interface can be shown schematically for chemical reaction control, gas phase diffusion control, and solid state diffusion control (Figure 70-Figure 73):

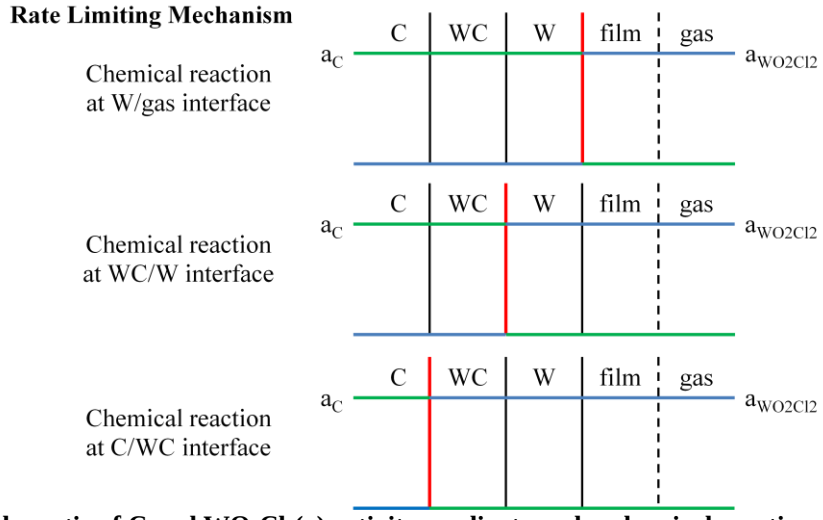

Figure 70: Schematic of C and $WO_2Cl_2(g)$ activity gradients under chemical reaction control

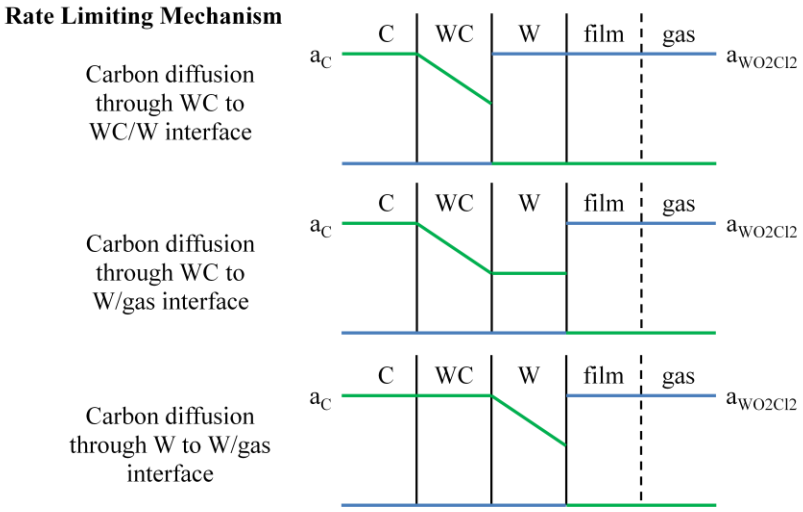

Figure 71: Schematic of C and WO_2Cl_2(g) activity gradients under solid state diffusion control

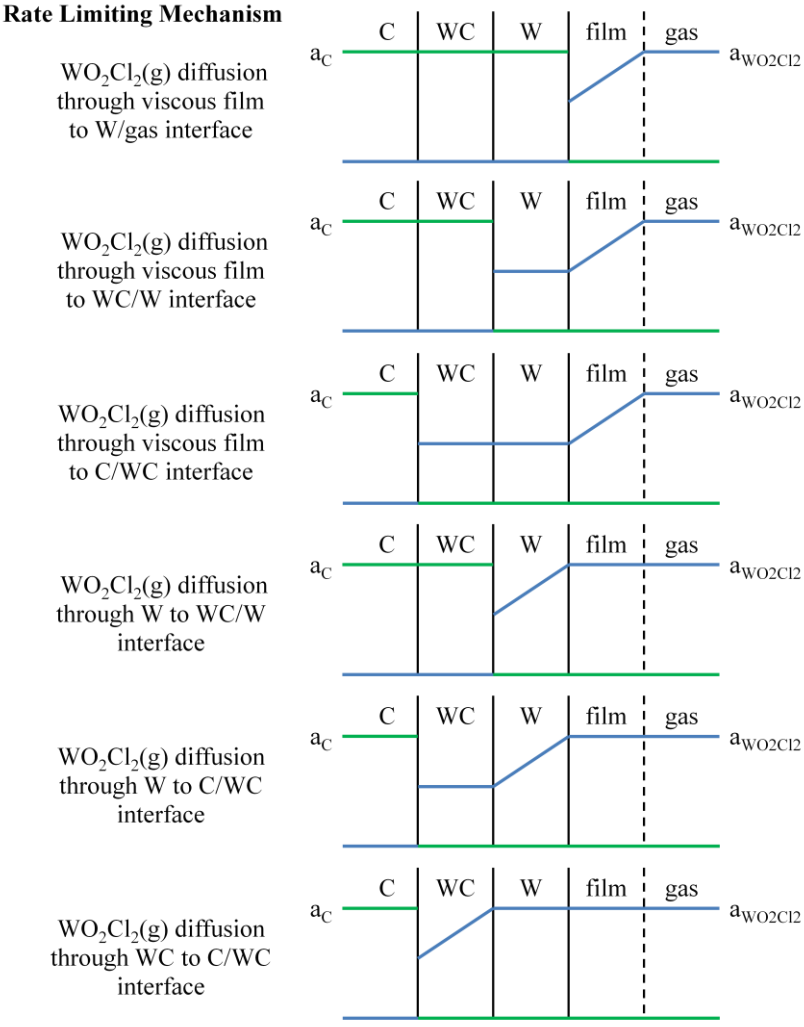

Figure 72: Schematic of C and WO_2Cl_2(g) activity gradients under gas phase diffusion control

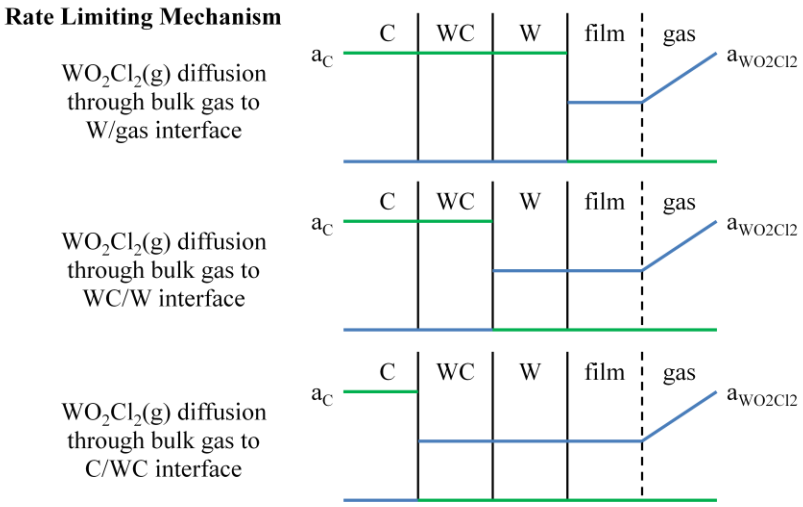

Figure 73: Schematic of C and WO_2Cl_2(g) activity gradients during reactant starvation, a special case of gas phase diffusion control

The activity gradients of reactants and products vary according to the rate limiting mechanism and reaction interface location. A non-zero activity gradient indicates that diffusion of that specie is relatively slow.

Consider the case where no WO_2Cl_2(g) or $WOCl_3$(g) activity gradients exist (which would be consistent with chemical reaction control or solid state diffusion control). As the reactive gas stream flows over the sample, the composition can be modeled to change with extent of reaction in the following way:

$$\dot{n}_{WO2Cl2,X} = \dot{n}_{WO2Cl2,i}(1 - X) \tag{2.29}$$

$$\dot{n}_{WOCl3,X} = \frac{2}{3}\dot{n}_{WO2Cl2,i}(X) \tag{2.30}$$

where $\dot{n}_{j,X}$ is the molar flowrate of species j after extent of reaction X and assuming that initially (at $X = 0$) there is no $WOCl_3$(g) (note: the factor of 2/3 in equation (2.30) results from the stoichiometry of reactions (2.7) and (2.14)). Defining the instantaneous local activities of WO_2Cl_2(g) and $WOCl_3$(g) after extent of reaction X as:

$$a_{WO2Cl2,X} = \frac{\dot{n}_{WO2Cl2,X}}{\dot{n}_{total,X}} \tag{2.31}$$

$$a_{WOCl3,X} = \frac{\dot{n}_{WOCl3,X}}{\dot{n}_{total,X}} \tag{2.32}$$

where $\dot{n}_{total,X}$ is given by:

$$\dot{n}_{total,X} = \dot{n}_{Ar} + \dot{n}_{WO2Cl2,X} + \dot{n}_{WOCl3,X} + \dot{n}_{CO,X} \quad (2.33)$$

Assuming that $WOCl_3$(g) and CO(g) are generated in a 1:2 molar ratio by reactions (2.7) and (2.14), then $\dot{n}_{CO,X} = 2\ \dot{n}_{WOCl3,X}$. Using this relation, and substituting equations (2.29) and (2.30) into (2.33) yields the following simplified expression:

$$\dot{n}_{total,X} = \dot{n}_{Ar} + \dot{n}_{WO2Cl2,i}(1 + X) \quad (2.34)$$

For given Ar(g) and initial WO_2Cl_2(g) molar flow rates (such as those given in Table 12), the extent of reaction *X* at which the instantaneous local activities of WO_2Cl_2(g) and $WOCl_3$(g) satisfy the equilibrium of equation (2.15) at 1100°C and 2.36 bar pressure have been calculated:

Table 12: Calculated extent of reaction corresponding to the W/WC stability threshold at 1100°C and 2.36 bar pressure as a function of inlet carrier gas velocity for a fixed WO_2Cl_2(g) generation rate of 4.54×10^{-4} mol/min.

$u_{Ar,\ inlet}$ (cm/s)	$\dot{n}_{Ar}$ (mole/min.)	$\dot{n}_{WO2Cl2,i}$ (mole/min.)	$a_{WO2Cl2,i}$	X	$a_{WO2Cl2,X}$	$a_{WOCl3,X}$
0.85	1.57×10^{-2}	4.54×10^{-4}	2.81×10^{-2}	0.99	3.90×10^{-4}	1.80×10^{-2}
0.64	1.18×10^{-2}	4.54×10^{-4}	3.71×10^{-2}	0.98	6.63×10^{-4}	2.34×10^{-2}
0.42	7.85×10^{-3}	4.54×10^{-4}	5.47×10^{-2}	0.97	1.37×10^{-3}	3.37×10^{-2}
0.10	1.96×10^{-3}	4.54×10^{-4}	1.88×10^{-1}	0.93	1.18×10^{-2}	9.88×10^{-2}
0.03	4.91×10^{-4}	4.54×10^{-4}	4.81×10^{-1}	0.86	4.62×10^{-2}	1.96×10^{-1}

The extent of reaction corresponding to the W/WC stability threshold is found to decrease with decreasing inlet carrier gas velocity. While this trend is in agreement with the product layer compositions reported in Figure 67, the magnitude of the predictions is not in agreement. This may indicate that either the calculated activities of WO_2Cl_2(g) and/or $WOCl_3$(g) are inaccurate, or, that the assumption of the model that there exists no WO_2Cl_2(g) or $WOCl_3$(g) activity gradients is invalid (which, if true, would provide evidence that the rate limiting mechanism must involve gas phase diffusion).

2.5.2. Determination of the Rate-Limiting Mechanism

The observed average reaction flux has been calculated to be 4.06×10^{-7} mol C reacted/cm^2s on the basis of the measured constant external surface area of 18.65 cm^2 and an average WO_2Cl_2(g) generation rate of 4.54×10^{-4} mol/min. (i.e. – assuming that complete depletion of WO_2Cl_2(g) occurs due to reaction with carbon upon the entire surface area of the specimen). If complete depletion of WO_2Cl_2(g) occurs upon only partial exposure to the surface area of the specimen, then this idealization would underestimate the true reaction flux (e.g. - this may correspond to the linear regime in Figure 61 where nearly full theoretical yield was observed). On the other hand, if, after exposure of WO_2Cl_2(g) upon the entire surface area of the specimen, the WO_2Cl_2(g) has not been entirely depleted, then this idealization would overestimate the true reaction flux (e.g. – this may correspond to the parabolic regime in Figure 61 where less than full theoretical yield was observed). Since this estimate of the reaction flux may be underestimated in the linear regime and overestimated in the parabolic regime, it is expected that at least the order of magnitude be accurate near the observed transition from linear to parabolic kinetics, which is sufficient for the discussions at hand.

The value of the observed average reaction flux has been compared to the calculated flux for solid state diffusion of carbon through WC and gas phase diffusion of WO_2Cl_2 to gain insight into the location of the reaction interface and the possible rate limiting mechanisms consistent with the observed data. In the absence of precise kinetic data as a function of time, position from the leading edge of the substrate, and local gas phase composition at the reaction interface for the reaction between C and

WO_2Cl_2(g)/$WOCl_3$(g) mixtures, the reaction kinetics have been modeled to a first approximation using the assumption of steady-state diffusion as expressed by Fick's law:

$$J_j = D\nabla C_j = \frac{D}{\delta}\Delta C_j \tag{2.35}$$

where J_j is the flux of species j diffusing through distance δ with effective diffusion coefficient D with a net change in concentration of species j given by ΔC_j. Depending on the rate limiting mechanism, the concentration gradient (in the case of gas phase diffusion) and diffusion distance (in the case of gas or solid state diffusion through a growing product layer) may vary with time and extent of reaction; therefore, for a given case where these parameters vary during the course of reaction, a median value for the expected range of values has been assumed.

In the case of inward WO_2Cl_2(g) diffusion being rate-limiting, the maximum diffusing concentration is given by the ideal gas law, and the local concentration at the reaction interface is assumed to be zero. In the case of outward carbon diffusion being rate limiting, the maximum concentration is given by the molar solubility of carbon in the diffusing material and the local concentration at the reaction interface is again assumed to be zero.

The calculated reactant flux for several possible rate limiting cases is summarized below (Table 13):

Table 13: Calculated reaction flux at 1100°C and an inlet carrier gas velocity of 0.85 cm/s for several possible rate limiting diffusional mechanisms

Diffusing species	Diffusing medium	Diffusion distance δ (cm)	Diffusing concentration C_j (mol/cm^3)	Diffusion coefficient D (cm^2/s)	Reaction Flux (mol C reacted/cm^{2}s)
C	WC	$2x10^{-3}$[a]	0.13[d]	$1x10^{-11}$[86]	$7.1x10^{-10}$
WO_2Cl_2	Ar	0.22[b]	$2.90x10^{-7}$[e]	0.46[f]	$8.1x10^{-7}$[g]
WO_2Cl_2	Ar	0.32[c]	$2.90x10^{-7}$[e]	0.46[f]	$5.5x10^{-7}$[g]
WO_2Cl_2	Ar	$2x10^{-3}$[a]	$2.90x10^{-7}$[e]	0.46[f]	$8.9x10^{-5}$[g]

[a] Based on minimum thickness observed in Figure 65.
[b] Calculated thickness of viscous gas layer, see Appendix B
[c] The diffusion distance varies with extent of reaction from zero in the unreacted state to a value corresponding to the half-thickness of the substrate (for two-sided reaction and diffusion) in the fully reacted state. For time-invariant steady-state calculations, an average diffusion distance corresponding to the median value of these extremes (half the specimen half-thickness) has been assumed.
[d] Assuming 1 at. % solubility of C in WC
[e] The maximum WO_2Cl_2 diffusing concentration varies with position along the substrate from the initial free-stream concentration in the unreacted state to zero in the fully reacted state. For time-invariant steady-state calculations, an average maximum diffusing concentration corresponding to the median value of these extremes (half the initial free-stream concentration) has been assumed.
[f] Calculated using Chapman-Enskog theory, see Appendix B
[g] Assuming a 4:3 C:WO_2Cl_2(g) molar reaction stoichiometry, see reaction (2.7)

The first case considered in Table 13 is C diffusion through a WC layer of 20 µm thickness (representative of the minimum observed thickness for a specimen at nominally 20 mol. % extent of reaction at an inlet carrier gas velocity of 0.85 cm/s, as seen in Figure 65). The maximum concentration of C in WC has been conservatively estimated to be 1 at. % on the basis of the W-C phase diagram[85]. At 1100°C, a diffusion coefficient of $1x10^{-11}$ cm^2/s for bulk diffusion of carbon through WC has been reported[86] (a value of $3x10^{-20}$ cm^2/s for grain boundary diffusion is reported in the same work, indicating that vacancy diffusion through the bulk is considerably faster). The calculated rate of reactant flux for the case of carbon diffusion through even a 20 µm thick WC product layer has been found to be merely $7.1x10^{-10}$ mol/cm^{2}s – over five hundred times slower than the

observed rate. This suggests that short-circuit diffusion paths (such as a high density of edge dislocations or significant cracking) must exist for carbon to diffuse through the WC layer to reach, at a minimum, the observed reaction rate. An alternative explanation would be that carbon does not diffuse outward through the WC product layer at all, but, rather, that WO_2Cl_2 can readily permeate the WC layer to react with carbon at the C/WC interface. This can only happen if the WC layer has significant cracking and/or pore channels. However, if this can occur it would explain the absence of Kirkendall pore development on the interior of the reacting specimen even up to complete conversion (whereas a Kirkendall pore is clearly visible in partially reacted (Figure 46) and fully converted (Figure 47) carbon fibers).

As summarized in Table 13, the magnitude of the averaged time-invariant steady-state WO_2Cl_2(g) flux from gas phase limited diffusion over a range of diffusion distances from 0.22 cm (see note (b) in Table 13) to 0.32 cm (see note (c) in Table 13) has been found to be in reasonable agreement with the observed reaction flux of 4.06×10^{-7} mol C reacted/cm^2s. However, diffusion over a distance corresponding to the median WC product layer thickness has been found to overestimate the reaction flux by a factor of over two hundred and is therefore not likely to be rate limiting.

While the magnitude of the calculated reaction flux for diffusion of WO_2Cl_2(g) through the viscous gas layer was consistent with the observed reaction flux, it has been shown to be inconsistent with the observed data when modeling the expected rate of change of reaction rate with extent of reaction. Consider that the reaction rate (τ) for diffusion limited processes can be expressed as the flux (J_j) multiplied by the area (A_J) to which the flux diffuses:

$$\tau_{diff.} = J_j A_J \tag{2.36}$$

Substitution of (2.34) into (2.35) yields:

$$\tau_{diff.} = \frac{DA_j}{\delta}\Delta C_j \tag{2.37}$$

which can be re-arranged into terms that are vary and are invariant with respect to extent of reaction:

$$\tau_{diff.} = D\Delta C_j\left(\frac{A_j}{\delta}\right) = F\left(\frac{A_j}{\delta}\right) \tag{2.38}$$

where F represents the gathered invariant terms. The change in reaction rate is given by:

$$\Delta\tau_{diff.} = F * \Delta\left(\frac{A_j}{\delta_j}\right) \tag{2.39}$$

which is more conveniently expressed as the relative change in reaction rate:

$$\frac{\Delta\tau_{diff.}}{\tau_{diff.}} = \frac{\Delta\left(\frac{A_j}{\delta_j}\right)}{\frac{A_j}{\delta_j}} \tag{2.40}$$

which no longer depends on the invariant term *F* and is expressed solely in terms of geometrical parameters.

Similarly, the relative change in the observed reaction rate for chemical reaction limited kinetics (the magnitude of which could not be modeled *a priori*) can be expressed in terms of geometrical parameters:

$$\tau_{rxn} = GA_j \tag{2.41}$$

where *G* represents the rate law for the chemical reaction occurring at the interface, assumed to be invariant with extent of reaction. Then, the change and relative change of reaction rate for chemical reaction limited kinetics are given by:

$$\Delta\tau_{rxn} = G\Delta A_j \tag{2.42}$$

$$\frac{\Delta\tau_{rxn}}{\tau_{rxn}} = \frac{\Delta A_j}{A_j} \tag{2.43}$$

The directions of the changes in reaction interfacial area and diffusion distance with extent of reaction are observed or modeled to vary in the following ways:

Table 14: Directions of the changes of interfacial area and diffusion distance with extent of reaction

Reaction Interface	ΔA_j	**Diffusion Distance**	$\Delta\delta_j$
C/WC	-	WC	?
WC/W	-	W	+
W/gas	+	Viscous gas film	0

The growth of a W and/or WC product layers is accompanied by recession of the WC/W and C/WC interfaces which requires that the WC/W and C/WC interfacial areas decrease. Since the W product layer is porous, the W/gas interfacial area increases as the product layer grows. The thickness of the WC product layer varies with position, but its variation with respect to extent of reaction is unknown. Lastly, the thickness of the viscous gas film over the substrate has been modeled to be a constant value (see Appendix B).

Suppose that the geometry of the reacting specimen can be represented by a square prismatic shrinking-core for a specimen of unchanging external dimensions (Figure 74):

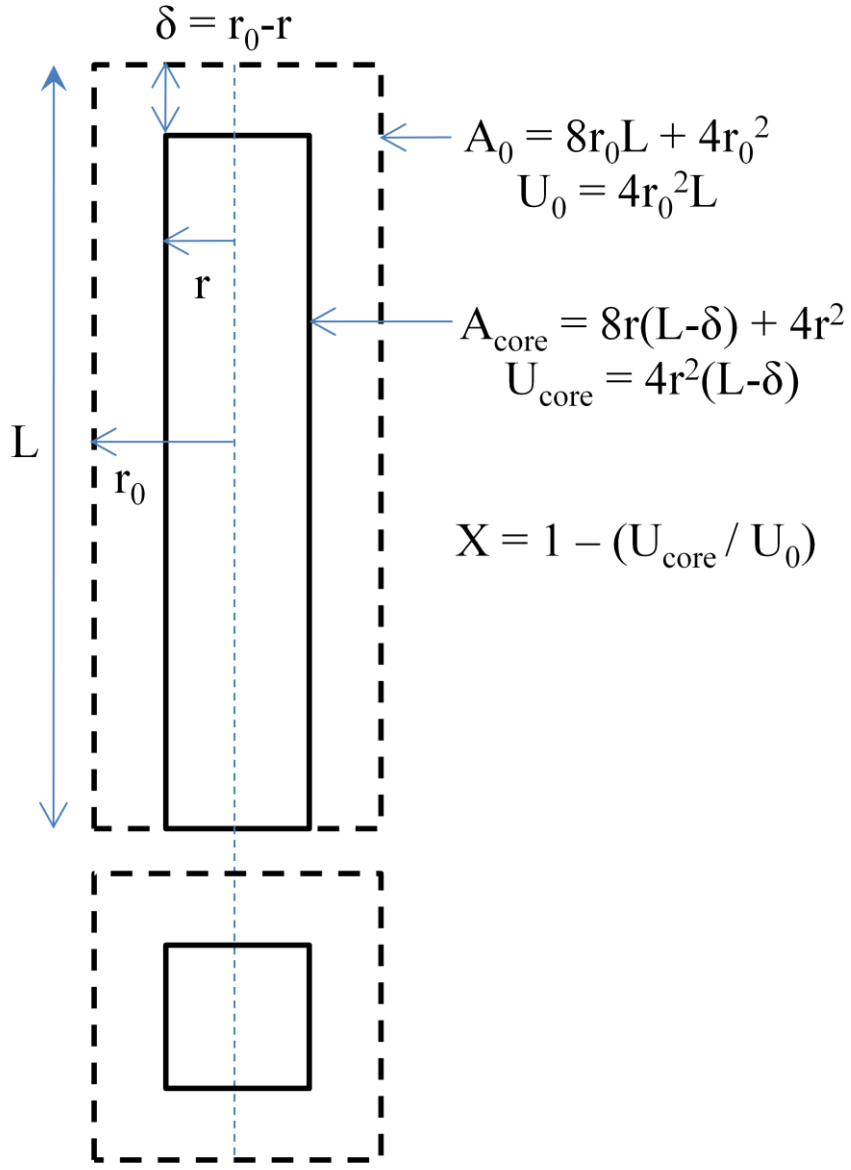

Figure 74: Square prismatic geometric model for reaction of substrate

where *L* is the length of the specimen, *r* is an average effective position of the WC/W interface and r_0 is the original effective position of the W/gas interface, taken as the half-thickness of the specimen, *U* is volume, and *A* is area. (If the WC product layer thickness is assumed small compared to the W product layer thickness, as has been observed for up to 20 vol. % conversion at a gas inlet velocity of 0.85 cm/s, then the effective position of the C/WC interface is approximated by the effective position of the WC/W interface.) To

a first approximation, this model represents the progress of reaction of a relatively dense graphite specimen as shown in Figure 62.

The relative changes in the C/WC and/or WC/W interfacial areas (shown as A_{core} in Figure 74 and corresponding to chemical reaction control at the C/WC and/or WC/W interfaces) and relative changes in the ratios of C/WC and/or WC/W interfacial areas to effective diffusion distance (shown as A_{core} and δ in Figure 74 and corresponding to WO_2Cl_2 diffusion to the C/WC and/or WC/W interfaces) as a function of volume percent reacted have been calculated on the basis of this shrinking core model. That is, for the geometry shown in Figure 74, the relative change in the interfacial area of the shrinking core to the original external surface area and the relative change in the ratio of the interfacial area of the shrinking core to the diffusion distance δ, have been calculated for 1-50 vol. % reaction (corresponding to the linear reaction regime in Figure 63) and 50-85 vol. % reaction (corresponding to the parabolic reaction regime in Figure 63) (i.e. – the original area and diffusion distance against which relative changes are evaluated correspond to 1 vol. % reaction in the linear regime and 50 vol. % reaction in the parabolic regime). The results of such calculations have been plotted and compared to the observed data (Figure 75 and Figure 76):

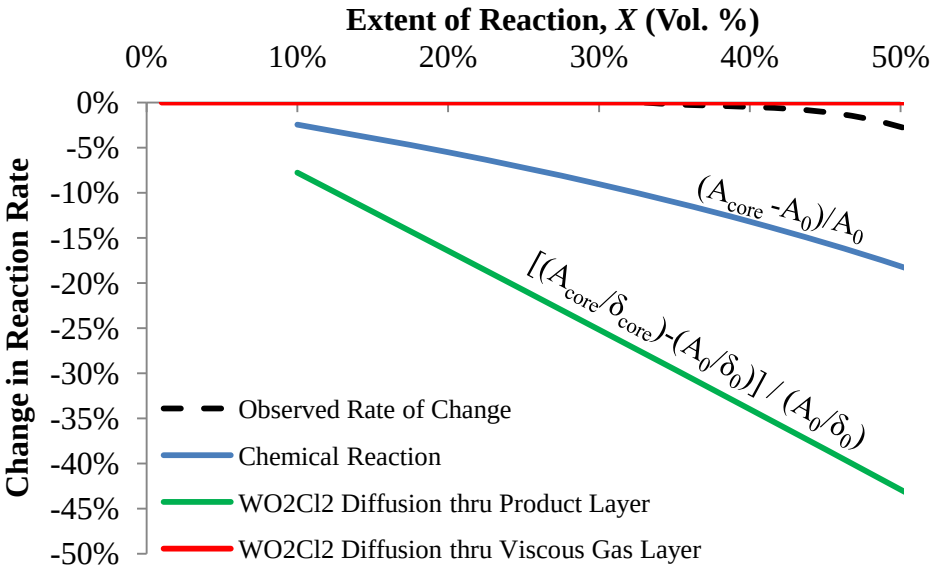

Figure 75: Shrinking core model in the apparent linear regime at < 50 vol. % extent of reaction, normalized to A_0, δ_0 at 1 vol. % reaction

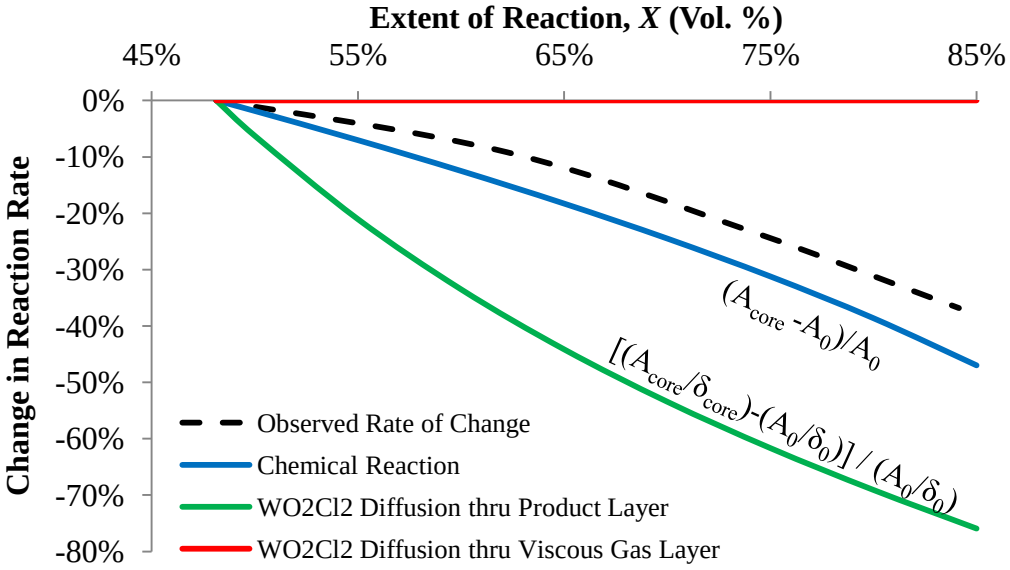

Figure 76: Shrinking core model in the parabolic regime at > 50 vol. % extent of reaction, normalized to A_0, δ_0 at 50 vol. % reaction

Rate-limiting mechanisms involving the W/gas interface have not been quantified in Figure 75 and Figure 76 due to lack of information on the change in interfacial surface area with extent of reaction. Nonetheless, it is clear that this interfacial area increases with extent of reaction and as a result one would predict an increase in reaction rate

regardless of the rate-limiting mechanism if reaction occurs at this interface. Therefore, it is unlikely that any process occurring at the W/gas interface is rate determining.

For the possible rate-limiting case of gas phase diffusion through a viscous gas layer, the area to which WO_2Cl_2(g) diffuses (the external surface area of the reacting specimen) is unchanging as is the distance through which the gas diffuses (see Appendix B); thus, the relative change in reaction rate caused by this rate-limiting mechanism would be expected to remain constant throughout reaction. This trend is consistent with the observed data in the linear regime, though inconsistent in the parabolic regime. Therefore, in the parabolic regime, it is unlikely that WO_2Cl_2(g) diffusion through the viscous gas layer is rate-limiting.

The modeled rate of change of reaction rate with extent of reaction for chemical reaction control and WO_2Cl_2(g) diffusion control through the growing product layer have been shown to be inconsistent with the apparent linear reaction kinetics. Therefore, it is concluded that the rate-limiting step in the linear regime for extents of reaction up to 50 vol. % is likely to be either mass transport to the boundary layer (i.e. - reactant starvation is limiting the observed kinetic rate and causing an *apparent* linearity) or WO_2Cl_2(g) diffusion through a viscous gas layer of constant thickness.

Two possible rate-determining mechanisms have been identified whose relative change in reaction rates with extent of reaction and whose calculated diffusional fluxes are not inconsistent with the parabolic regime for extents of reaction between 50 and 85 vol. % reacted: gas phase diffusion of WO_2Cl_2 through a growing permeable product layer(s) to the C/WC interface, and a chemical reaction at the C/WC interface. While it cannot be definitively eliminated as a possible rate-limiting mechanism, diffusion of

carbon through a WC layer via short-circuit pathways seems unlikely for two reasons: first, the magnitude of the calculated flux for carbon through WC is several orders of magnitude slower than the observed reaction rate, and, second, there was an absence of observed Kirkendall pores for specimens reacted through the thickness.

It is not entirely clear that the development of Kirkendall pores in reacting amorphous carbon fibers, and their absence in reacting isotropic graphite, can be entirely attributed to the disparity in the sizes of the structures being converted (fibers are 7.2 μm in diameter, while graphite has been thusfar reacted through specimens of 64 mm thickness). Future studies may seek to determine the effects on reaction rate and product morphology of carbon crystallinity, grain size, and pore structure. The present author would speculate that changes in the reaction rate and product morphology would only be expected if kinetics were rate-limited by an interfacial chemical reaction.

A more detailed examination of this system is required in order to fully understand the reaction kinetics. Especially beneficial would be a more robust reactor design allowing for simultaneous control of inlet gas velocity and WO_2Cl_2 activity, and of large enough dimensions to allow for specimens of varying size and geometry to be reacted. Additionally, specialized equipment such as in-situ thermogravimetric analysis and spectroscopic analysis of the exhaust stream would greatly enhance the study of reaction kinetics; though, design of such systems would need to overcome the many obstacles associated with instrumentation for high temperature corrosive atmospheres.

2.5.3. Implications of the Work

The potential applications for metal or metal carbide replicas of carbon templates vary with the character of the transformed metal or metal carbide. Tungsten, for example,

finds use in extreme environments with high heat fluxes such as in solid fueled rocket motors[87] and nuclear fusion plasma divertors[88]. Other novel applications include reinforcement for bulk metallic glass composite kinetic penetrators[89] and infrared photonic crystals for thermophotovoltaics[90].

In theory, other metals and/or metal carbides can be produced using the proposed reaction scheme. Thermodynamic calculations show the following *in-situ* reactions to produce metal oxyhalides are favorable:

$$3CaCl_2 + 4Nb_2O_5 \leftrightarrow 3CaNb_2O_6 + 2NbOCl_3(g) \quad (2.44)$$
$$CaCl_2 + 2MoO_3 \leftrightarrow CaMoO_4 + MoO_2Cl_2(g) \quad (2.45)$$

The standard Gibbs free energy changes for reactions (2.44) and (2.45) at 1 bar pressure decrease with temperature and are zero at 1080°C and 300°C, respectively[70]. These vapor species can favorably react with carbon to form metal or metal carbides via the following reactions:

$$4C + 4NbOCl_3(g) \leftrightarrow Nb + 3NbCl_4(g) + 4CO(g) \quad (2.46)$$
$$5C + 4NbOCl_3(g) \leftrightarrow NbC + 3NbCl_4(g) + 4CO(g) \quad (2.47)$$
$$4C + 2MoO_2Cl_2(g) \leftrightarrow Mo + MoCl_4(g) + 4CO(g) \quad (2.48)$$
$$5C + 2MoO_2Cl_2(g) \leftrightarrow MoC + MoCl_4(g) + 4CO(g) \quad (2.49)$$

The standard Gibbs free energy changes for reactions (2.46) through (2.49) at 1 bar pressure decrease with temperature and are zero at 1750°C, 1430°C, 620°C and 560°C, respectively[70]. Although no data exists for $CaTa_2O_6$, if a similar reaction to (2.44) is favorable for tantalum species, then the following reactions are also possible:

$$4C + 4TaOCl_3(g) \leftrightarrow Ta + 3TaCl_4(g) + 4CO(g) \quad (2.50)$$
$$5C + 4TaOCl_3(g) \leftrightarrow TaC + 3TaCl_4(g) + 4CO(g) \quad (2.51)$$

The standard Gibbs free energy changes for reactions (2.50) and (2.51) at 1 bar pressure decrease with temperature and are zero at 1680°C and 1390°C, respectively[70].

Indeed, as proof of concept, carbon foams have been successfully converted into Mo replicas in a manner analogous to the process to form W replicas. MoO_3 powder (99.5% purity, Alfa Aesar, Ward Hill MA) replaced WO_3 powder in the experimental setup and procedures described in section 2.3.1 with one modification: a molar ratio of 1:1 $CaCl_2$:MoO_3 powders was used due to concerns associated with having an excess of MoO_3 owing to its significantly greater volatility as compared to WO_3 at temperatures up to 1000°C. Graphitic foam was converted into molybdenum replicas (Figure 77 and Figure 78):

Figure 77: Graphitic PocoHTC foam (left), tungsten replica (middle) and molybdenum replica (right) produced at 1100°C at an inlet gas carrier flow rate of 0.10 cm/s

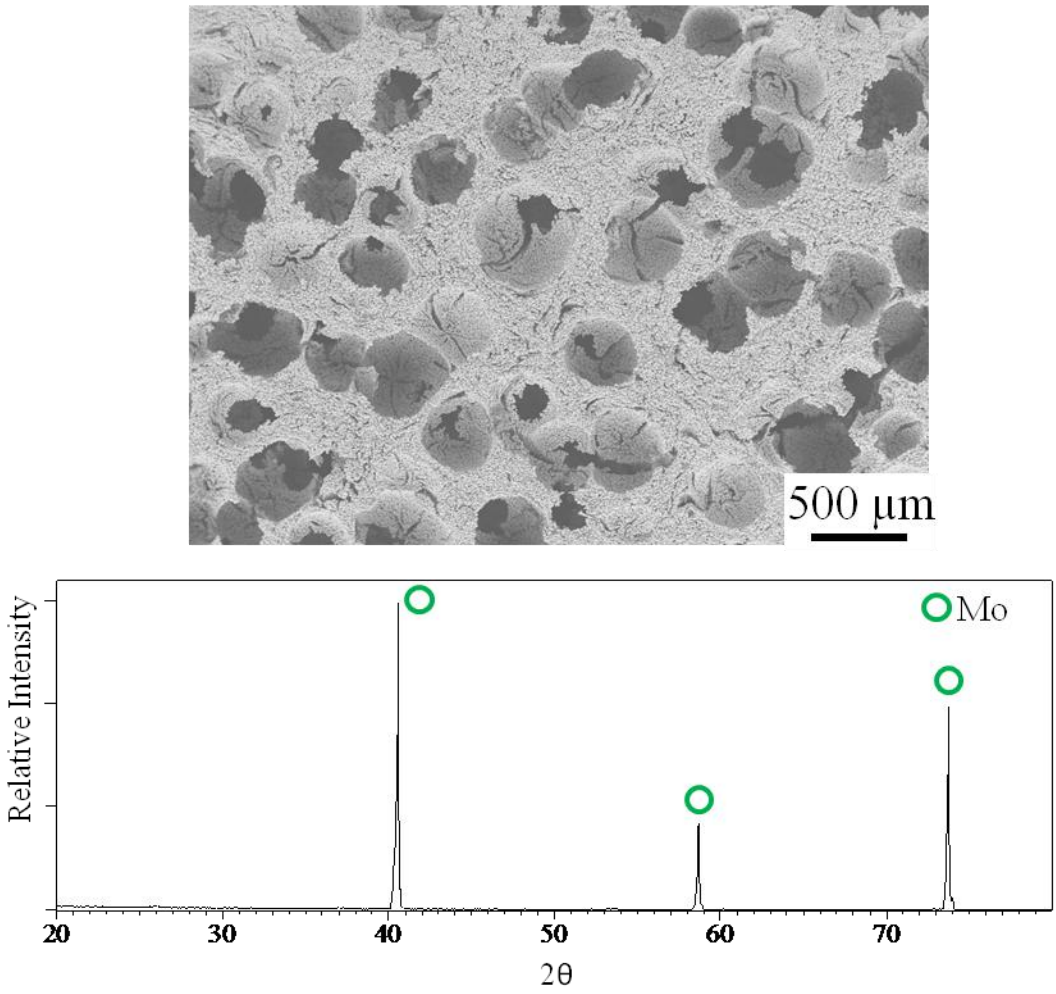

Figure 78: Molybdenum replica of PocoHTC foam (1000°C, 8h at inlet carrier gas velocity of 0.10 cm/s) (PDF Card No. 04-0809)

The fabrication of Nb/NbC and Ta/TaC replicas has not yet been demonstrated and may be a productive future endeavor. Of further future interest might be the direct conversion of carbon into metal/metal carbide composites via simultaneous introduction of multiple gas phase reactants (such as a mixture of MoO_2Cl_2(g) and $NbOCl_3$(g) to produce Mo/NbC composites). A more robust reactant delivery system and reactor design would be required in order to demonstrate that this process has such capabilities.

2.6. *Conclusions*

Carbonaceous templates have been converted into porous tungsten/tungsten carbide replicas with retention of exterior dimensions and microstructural features by reaction with a suitable metal-bearing reactive gas at high activities. The morphology of partially-reacted specimens reveals a highly porous tungsten outer scale atop a more compact tungsten carbide inner scale. The relative thermodynamic stability of these phases has been determined and is in qualitative agreement with the observed ratios in the product layers as a function of gas phase activities. Kinetic studies have been performed to determine the rate limiting mechanism of reaction and have shown that for extents of reaction up to 50 vol. % the reaction kinetics are likely limited by either mass transport of $WO_2Cl_2(g)$ to the specimen (resulting in reactant starvation) or through a viscous gas layer of constant thickness. For extents of reaction greater than 50 vol. % two possible steps are likely to be rate determining: $WO_2Cl_2(g)$ diffusion to the C/WC interface or a chemical reaction at the C/WC interface. Further work is required to fully characterize the complex kinetics for this reaction system.

The most immediate application of this reaction would be for the production of porous WC preforms for the fabrication of ZrC/W-bearing composites via the DCP process. By partially or fully converting an easily shapeable carbon preform into porous WC, greater degrees of control over phase contiguity and microstructure can be introduced than by powder-based preform fabrication methods (e.g., via the introduction of continuous fibers or other aspected structures). The suggested focus for future endeavors should be on the design of a more robust reactor capable of delivering large

quantities of WO_2Cl_2(g) at controlled activities and with controlled admixtures of CO(g) or $WOCl_3$(g) in order to shift the equilibrium position towards WC stability.

2.7. *References*

[40] Dickerson, M.B. et al. "Near net-shape, ultra-high melting, recession-resistant ZrC/W-based rocket nozzle liners vis the displacive compensation of porosity (DCP) method," *J. Mat. Sci.*, **39**, 6005-6015, (2004).

[41] Lipke, D.W., Zhang, Y., Liu, Y., Church, B.C. and Sandhage, K.H. "Near net-shape/net-dimension ZrC/W-based composites with complex geometries via rapid prototyping and Displacive Compensation of Porosity," *J. Euro. Ceram. Soc.*, **30**(11), 2265-2277 (2010).

[42] Becher, P.F. "Microstructural design of toughened ceramics," *J. Am. Ceram. Soc.*, **74**(2), 255-269 (1991).

[43] Faber, K.T. and Evans, A.G. "Crack deflection processes - I. Theory," *Acta Metall.*, **31**(4), 565-576 (1983).

[44] Evans, A.G. and Marshall, D.B. "The mechanical-behavior of ceramic matrix composites," *Acta Metall.*, **37**(10), 2567-2583 (1989).

[45] Faber, K.T. and Evans, A.G. "Crack deflection processes - II. Experiment," *Acta Metall.*, **31**(4), 577-584 (1983).

[46] Agrawal, P. and Sun, C.T. "Fracture in metal-ceramic composites," *Comp. Sci. Tech.*, **64**, 1167-1178 (2004).

[47] Raddatz, O., Schneider, G.A., Mackens, W., Voss, H. and Claussen, N. "Bridging stresses and R-curves in ceramic/metal composites," *J. Euro. Ceram. Soc.*, **20**, 2261-2273 (2000).

[48] Honjo, K. and Shindo, A. "Carbon fibers with duplex metal carbide coating and methods for manufacture thereof" US Patent 4405685 (Sept. 20, 1983).

[49] Bouix, et al. "Process for coating carbon fibers with a carbide, and carbon fibers thus coated" US Patent 4859503 (Aug. 22, 1989). Continued in part by US Patent 4921725 (May 1, 1990).

[50] Lennartz, J.W. "Fluidized bed reactor and method for forming a metal carbide coating on a substrate containing graphite or carbon" US Patent 5498442 (Mar. 12, 1996).

[51] Hamling, B.H. "Process for producing metal carbide fibers, textiles and shapes" US Patent 3403008 (Sept. 24, 1968). Continued in part by US Patent 4162301 (July 24, 1979).

[52] Gilbert, T.R., Soman, R.S., and Li, J. "Method of forming a carbide on a carbon substrate" US Patent 5141773 (Aug. 25, 1992). Continued in part by US Patent 5238711 (Aug. 24, 1993).

[53] Preiss, H., Meyer, B. and Olschewski, C. "Preparation of molybdenum and tungsten carbides from solution derived precursors," *J. Mater. Sci.*, **33**, 713-722 (1998).

[54] Kurokawa, Y., Kobayashi, S., Suzuki, M., Shimazaki, M. and Takahashi, M. "Preparation of refractory carbide fibers by thermal decomposition of transition metal (Ti, Zr, Hf, Nb, Ta) alkoxide-cellulose precursor gel fibers," *J. Mater. Res.*, **13**(3), 760-765(1998).

[55] Gadiou, R., Serverin, S., Gibot, P. and Vix-Guterl, C. "The synthesis of SiC and TiC protective coatings for carbon fibers by the reactive replica process," *J. Euro. Ceram. Soc.*, **28**, 2265-2274 (2008).

[56] Li, X. et al. "Preparation of a titanium carbide coating on carbon fiber using a molten salt method," *Carbon*, **46**, 305-309 (2008).

[57] Nieh, T.G. and Vidoz, A.E. "Carbide coatings on graphite fibers by liquid metal transfer agent method," *J. Am. Ceram. Soc.*, **65**(5), 227-230 (1982).

[58] Himbeault, D.D., Varin, R.A. and Piekarski, K. "Coating of graphite fibers with tungsten carbide using solid and liquid copper as a transfer medium," *Met. Trans.*, **19A**, 2109-2113 (1988).

[59] Givargizov, E.I. "Fundamental aspects of VLS growth," *J. Crys. Growth*, **31**, 20-30 (1975).

[60] Guha, S., Kyriacou, C., Withers, J., Loutfy, R. and Dowding, R. "A low cost synthesis technique for tungsten whiskers of <100> orientation," *Mater. Manu. Proc.*, **9**(6), 1061-1086 (1994).

[61] Wang, S. et al. "Formation and growth mechanism of tungsten oxide microtubules," *Chem. Phys. Lett.*, **427**, 350-355 (2006).

[62] Bamberger, C.E. "The pseudomorphic conversion of acicular crystals of sodium tungsten bronze into WC/W," *J. Mater. Sci. Lett.*, **13**, 1742-1745 (1994).

[63] Byrne, C.E. & Nagle, D.C. Carbonization of wood for advanced materials applications. *Carbon*, **35**(2), 259-266 (1997).

[64] Greil, P. Biomorphic ceramics from lignocellulosics. *J. Euro. Ceram. Soc.*, **21**(2), 105-118 (2001).

[65] Zakhidov, A.A., et al. Carbon structures with three-dimensional periodicity at optical wavelengths. *Science*, **282**, 897-901 (1998).

[66] Adelhelm, P., et al. Generation of hierarchical meso- and macroporous carbon from mesophase pitch by spinodal decomposition using polymer templates. *Adv. Mat.*, **19**, 4012-4017 (2007).

[67] Besmann, T.M., Sheldon, B.W., Lowden, R.A. & Stinton, D.P. Vapor-phase fabrication and properties of continuous-filament ceramic composites. *Science*, **253**, 1104-1109 (1991).

[68] Ledoux, M., Guille J., Pham-Huu, C. and Marin, S. "Production of heavy metal carbides of high specific surface area" US Patent 5391524 (Feb. 21, 1995).

[69] Paccaud, O. and Derre, A. "Silicon carbide coating by reactive pack cementation - Part I: Silicon carbide/silica interaction," *Chem. Vap. Dep.*, **6**(1), 33-40, (2000).

[70] Barin, I. *Thermochemical data of pure substances.* Wiley-VCH (2004).

[71] Levin, E.M., Robbins, C.R. and McMurdie, H.F (eds.). *Phase Diagrams for Ceramists: Volume I – Oxides and Salts*. Materials Park, OH: American Ceramic Society (1981).

[72] Levin, E. M. "System B_2O_3-WO_3," *J. Am. Ceram. Soc.*, **48**(9), 491-492 (1965).

[73] Meulencamp, E.A. "Mechanism of WO_3 electrodeposition from peroxy-tungstate solution," *J. Electrochem. Soc.*, **144**(5), 1664-1671 (1997).

[74] Turkdogan, E.T., Grieveson, P. and Darken, L.S. "Enhancement of diffusion-limited rates of volatilization of metals," *J. Phys. Chem.*, **67**, 1647-1654 (1963).

[75] Nakajima, H., Kudo, T. and Mizuno, N. "Reaction of metal, carbide, and nitride of tungsten with hydrogen peroxide characterized by 183W nuclear magnetic resonance and raman spectroscopy," *Chem. Mater.*, **11**, 691-697 (1999).

[76] Grzesik, Z., Dickerson, M.B. and Sandhage, K.H. "Incongruent reduction of tungsten carbide by a zirconium-copper melt," *J. Mater. Res.*, **18**(9), 2135-2140 (2003).

[77] Landolt-Bornstein database: *Thermodynamic Properties of Inorganic Material.* Berlin-Heidelberg: Springer-Verlag, 1999.

[78] NIST-JANAF Thermochemical Tables, Malcolm W. Chase Jr. (ed.). *J. Phys. Chem. Ref. Data Monograph 9*. Gaithersburg, MD: National Institute of Standards and Technology, 1998.

[79] Just, A. and Hanaman, F. Process for manufacture of incandescent bodies for electric lamps. U.S. Patent 855060. Filed July 6, 1905. Issued May 28, 1907.

[80] Howell, J.W. and Schroeder, H. *History of the Incandescent Lamp*. Schenectady, NY: The Maqua Co., 1927.

[81] Crouch, P.C., Fowles, G.W.A. & Walton, R.A. The high yield synthesis of the tungsten (VI) oxyhalides $WOCl_4$, $WOBr_4$ and WO_2Cl_2 and some observations on tungsten (VI) bromide and tungsten (V) chloride. *J. Inorg. Nucl. Chem.*, **32**, 329-333 (1970).

[82] Gibson, V.C., Kee, T.P. & Shaw, A. New, improved synthesis of the group 6 oxyhalides, $W(O)Cl_4$, $W(O)_2Cl_2$, and $Mo(O)_2Cl_2$. *Polyhedron*, **7**(7), 579-580, (1988).

[83] Bhagat, R., Jackson, M., Inman, D., and Dashwood, R. Production of Ti-W alloys from mixed oxide precursors via the FFC Cambridge process. *J. Electrochem. Soc.*, **156**(1), E1-E7 (2009).

[84] Erdogan, M. and Karakaya, I. "Electrochemical reduction of tungsten compounds to produce tungsten powder," *Metal. Mater. Trans. B.*, published online April, 2010.

[85] Rudy, E. and Hoffman, J.R. "Phase equilibria in the region of the cubic carbide phases in the tungsten-carbon system," *Planseeber. Pulvermet.*, **15**(3) 174-178 (1967).

[86] Treheux, D., Dubois, J. and Fantozzi, G. "Bulk and grain boundary diffusion of 14C in tungsten hemicarbide," *Ceram. Inter.*, **7**(4), 142-148 (1981).

[87] Thakre, P. & Yang, V. Chemical erosion of refractory-metal nozzle inserts in solid-propellant rocket motors. *J. Propul. Power*, **25**(1), 40-50, (2009).

[88] Sharafat, S., et al. Ultra-low pressure drop helium-cooled porous-tungsten PFC. *Fusion Sci. & Tech.*, **52**, 559-565 (2007).

[89] Dandliker, R.B., Conner, R.D. & Johnson, W.L. Melt infiltration casting of bulk metallic-glass matrix composites. *J. Mater. Res.*, **13**(10), 2896-2901 (1998).

[90] Fleming, J.G., Lin, S.Y., El-Kady, I., Biswas, R. & Ho, K.M. All-metallic three-dimensional photonic crystals with a large infrared bandgap. *Nature*, **417**, 52-55 (2002).

CHAPTER 3: Intragranular Metal/Ceramic Micro/Nanocomposites via Internal Reduction of Non-Oxide Solid Solution Ceramics

3.1. *Summary*

Processing techniques to form bulk nanocomposite materials are often limited by the requirement to synthesize nanocrystalline feedstocks that must subsequently be consolidated. Reactive processing techniques may yield nanostructures *in-situ*, avoiding this limiting factor and bypassing the associated health concerns of handling nanopowders. A novel reactive processing technique has been demonstrated to form intragranular metal/ceramic micro/nanocomposites via the internal reduction of non-oxide solid solution ceramics. The selective reduction of one component of the solid solution ceramic results in the precipitation of metal grains that can exhibit dimensions less than 100 nm if the processing temperature is sufficiently low, so that diffusion of the metal atoms through the ceramic matrix is limited and if there exists limited mutual solid solubility of the precipitated metal in the matrix phase. This chapter details the fabrication of ZrC/W-bearing intragranular micro/nanocomposites via the internal reduction of $Zr_yW_{1-y}C$ solid solutions.

3.2. *Introduction*

Composite materials, consisting of two or more distinct phases, are the subject of intense research and development owing to their potential to surpass the performance of traditional monolithic materials in a variety of demanding engineering applications. For example, as discussed in the previous chapters, solid rocket motors demand nozzle

materials resistant to ultra-high temperature thermal shock and ablative erosion for which neither monolithic ceramics nor refractory metals satisfy both requirements.

Nanostructured materials, in which the characteristic phase size is less than 100 nanometers, also hold the promise of improving material performance owing to the unique phenomena associated with very large surface area-to-volume ratios resulting in a large fraction of atoms or ions residing in grain boundary positions[91,92]. By assuming the grain boundary interface has a finite effective thickness (e.g., 1-2 nanometers) the volume fraction of grain boundary atoms can be estimated[92]:

> "Assuming the grains have the shape of spheres or cubes, the volume fraction of interfaces in the nanocrystalline material may be estimated as 3D/d (where D is the average interface thickness and d is the average grain diameter). Thus, the volume fraction of interfaces can be as much as 50% for 5 nm grains, 30% for 10 nm grains, and about 3% for 100 nm grains."

As the fraction of atoms in grain boundaries increases, the properties of the nanostructured material begin to reflect those of the grain boundaries rather than the bulk properties of the material. Improvements in ductility, fracture toughness, strength, hardness, creep and fatigue resistance have been reported for nanostructured metals and ceramics, although the physical mechanisms continue to be investigated[91,92,93,94,95,96].

Nanocomposite materials have the potential to combine the properties of nanostructures (i.e., having behavior dominated by high energy surface/interface atoms) with the benefits of joining dissimilar phases to form new composite materials whose combined properties exceed those of its constituents. Nanostructured composites are generally classified into three types[97]: nanoparticles embedded within micrograins (intra-granular micro/nanocomposites), nanoparticles as inclusions between micrograins (inter-

granular micro/nanocomposites) and composites consisting entirely of nanograins (nano/nanocomposites).

Development of appropriate processing conditions (i.e., temperature, pressure, and time) allowing for final stage sintering while simultaneously inhibiting grain growth to produce dense nanostructured engineering materials is challenging and may limit the service and processing temperatures of nanostructured engineering materials. Bulk nanocrystalline materials have been fully densified with retention of nanostructure by careful control over the sintering of nanocrystalline feedstocks[98,99]. Nanostructured composites of the nano/nano-type, such as platinum/barium hexa-aluminate[100] and hafnia/mesoporous silica[101], have been fabricated using solution processing and have shown resistance to coarsening up to 1200°C and 1500°C, respectively. Nanostructured composites of the intra- and inter-granular types have also been reported, including oxide/refractory metal compositions such as alumina/tungsten[102] and yttria-stabilized zirconia/molybdenum[103], produced by hot pressing nanocrystalline powders at temperatures up to 1600°C. A number of other techniques have been used to prepare metal and ceramic intra- and inter-granular nanocomposites[104,105], including chemical vapor deposition, sol gel synthesis, combustion/pyrolysis synthesis, and spray coating followed by consolidation via pressureless sintering, reaction sintering, hot isostatic pressing or hot pressing.

Most of these techniques, especially those used to produce ceramic matrix nanocomposites, have in common the need to synthesize nanocrystalline feedstocks prior to consolidation to form dense nanocomposites. Nanopowders require great care in their handling due to associated health concerns[106,107,108] as well as the increased oxygen and

moisture sensitivity of non-passivated powders. *In-situ* processing techniques to form nanostructured composites without nanocrystalline feedstocks can avoid these materials handling problems.

A novel, *in-situ* reactive infiltration method has been developed with the potential to produce dense, near-net shape, high temperature stable metal/ceramic intragranular micro/nanocomposites. This chapter describes the preliminary results of the reactive processing to form ZrC/W intragranular micro/nanocomposites.

3.3. *Experimental Procedures*

3.3.1. Reactive Infiltration of Solid-Solutionized Porous Ceramics

ZrC powder (Cerac Z-1034, -325 mesh, ~10 μm diameter, 99.5% purity) and WC powder (Buffalo Tungsten WC1, 1-2 μm diameter, 99.9% purity) were used as-received. ZrC powder was stored under argon to minimize oxidation. Comminution of ZrC powder was carried out in a Spex 8000M (Spec SamplePrep LLC, Metuchen NJ) high energy ball mill within a 5.70 cm inner diameter x 6.35 cm interior length tungsten carbide grinding vial with 9.5 mm tungsten carbide balls as grinding media. In a typical milling procedure, 20.00 g ZrC powder was weighed with a digital balance and added to two tungsten carbide balls (nominally 6.25 g each) within the tungsten carbide grinding jar. To this, 5.00 mL tetrachloroethylene (Sigma Aldritch, ACS reagent grade >99%, St. Louis, MO) was added and the grinding vial closed to hand-tightness. The vial assembly was then sealed within a vacuum bag (FoodSaver, Jarden Consumer Solutions, Boca Raton FL). This assembly was milled for six hours after which the tetrachloroethylene covering fluid

within the disassembled grinding vial was allowed to evaporate in a fume hood overnight in air.

Milled (or unmilled) ZrC powder was dry blended with WC powder in weighed proportions using polyethylene jar and media for one hour in the Spex 8000M mill. The blended powder mixture was then uniaxially cold pressed to a maximum pressure of 750 MPa within a hardened steel die. Powder compacts were simultaneously solid-solutionized and sintered in a graphite furnace under oxygen-gettered argon (Oxy-gon Industries, Epsom, NH) to a peak temperature of 2250°C for one hour.

Solid-solutionized powder compacts were reactively infiltrated with $Zr_{14}Cu_{51}$ at 1300°C for up to 24 hours. As previously described in chapter 1, $Zr_{14}Cu_{51}$ ingots were prepared via arc-melting and placed atop compacts within 2.5 cm diameter x 3.2 cm length MgO crucibles (Ozark Technical Ceramics, Webb City MO). Upon cooling, the crucibles were mechanically detached from the solidified melt encasing the reactively infiltrated porous ceramic.

3.3.2. Materials Characterization

Microstructural morphology and phase identification of starting materials, sintered preforms, and *in-situ* reactively processed micro/nanocomposites was conducted using a field emission scanning electron microscope (LEO 1530, Carl Zeiss, Cambridge, UK) equipped with backscattered (BSE) and secondary electron (SE) detectors and energy dispersive x-ray spectrometer (EDS) (INCA, Oxford Instruments, Bucks, UK), a high resolution transmission electron microscope (JEOL 4000EX, JEOL Ltd., Tokyo, Japan) with selected area electron diffraction (SAED) and an x-ray diffractometer (XRD) (X'Pert Alpha-1 Diffractometer, PANalytical, Almelo, The Netherlands) equipped with

monochromator using Cu Kα1 radiation. Surface area characterization was conducted by nitrogen adsorption analysis (Autosorb-1, Quantachrome, Boynton Beach, FL). Solidified melts encasing the reactively infiltrated porous ceramic were cross-sectioned using a low-speed diamond saw (MTI Corp., Richmond, CA) and polished to 1 µm finish with diamond impregnated cloth on a variable speed polishing wheel (Buehler, Lake Bluff, IL) for SEM observation or ion milled (Gatan Model 600, Pleasanton, CA) for HRTEM observation.

3.4. *Results*

XRD spectra of milled ZrC powder, as-received WC powder and uniaxially cold-pressed compacts consisting nominally of 60 mol. % ZrC and 40 mol.% WC solid-solutionized at 2250°C for 1 hour are shown below (Figure 79, Figure 80, and Figure 81):

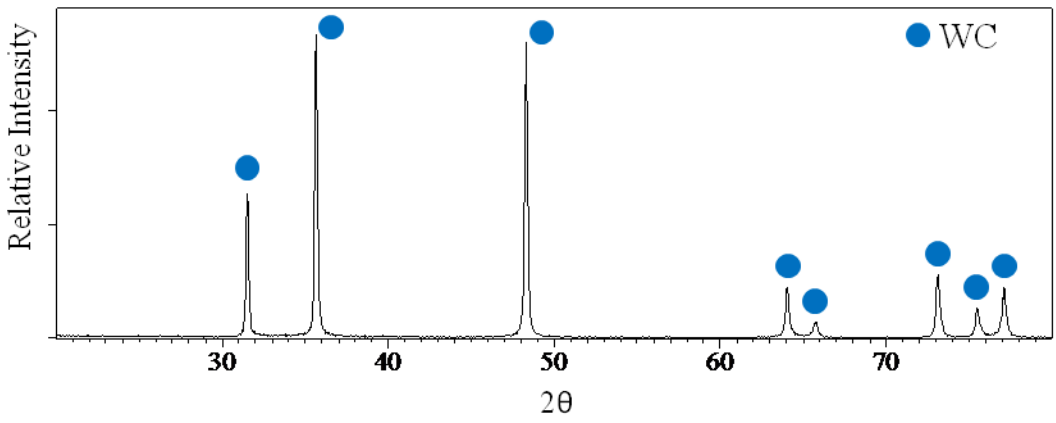

Figure 79: XRD analysis of WC starting material (PDF Card No. 25-1047)

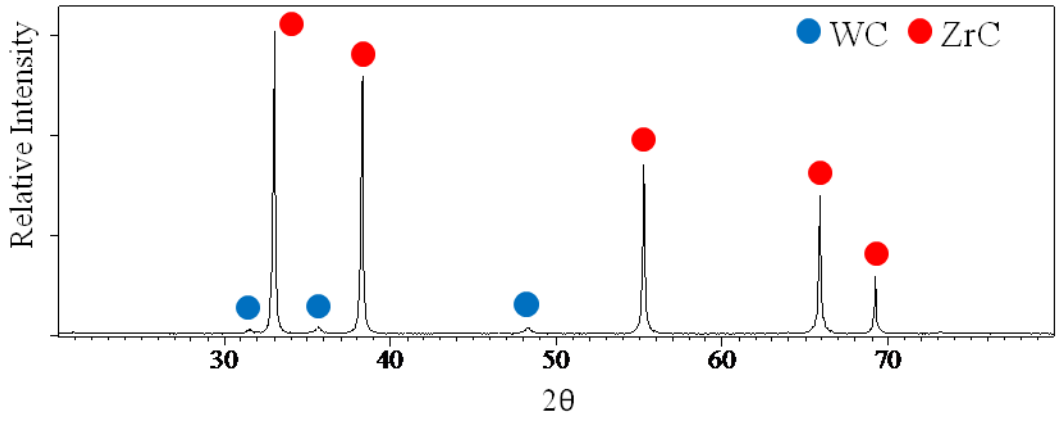

Figure 80: XRD analysis of milled ZrC powder (PDF Card No. 35-0784) with WC contamination from milling media (PDF Card No. 04-0806)

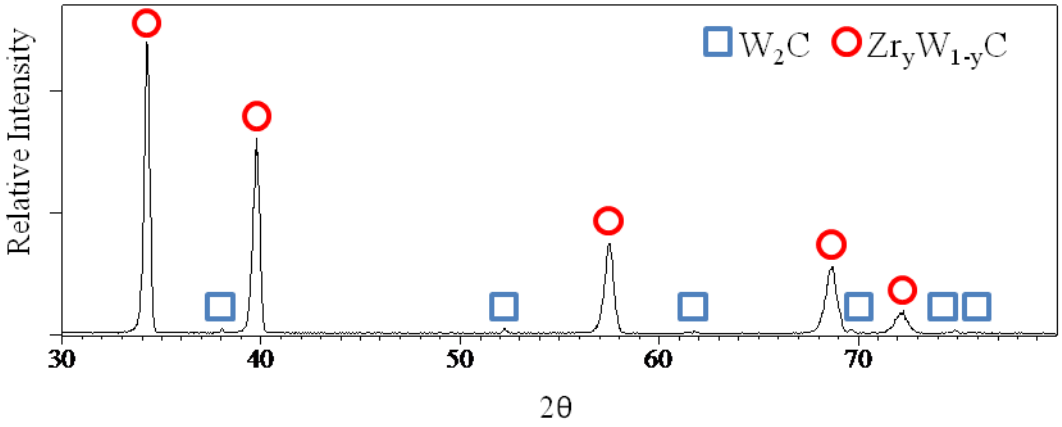

Figure 81: XRD analysis of 60 mol.% ZrC, 40 mol.% WC solid solution after 2250°C for 1 hour (W_2C PDF Card No. 35-0776)

Milled ZrC powder exhibits minor amounts of WC contamination from wear of the grinding vial and media. Weight change measurements indicated that up to 5 wt.% WC contamination resulted from the milling procedure. Nitrogen absorption measurements indicated a BET surface area per mass of 0.92 m^2/g for the as-received powder compared to 3.84 m^2/g after milling. Assuming spherical particles, the increase in BET surface area per mass corresponded to a 76% reduction in average particle radius.

Prior work[109] characterizing the ZrC-WC solid solution has shown that the system consists of cubic symmetry (until approximately 96 mol. % WC where it becomes hexagonal)[110,111,112,113] with a lattice parameter (b) that varies with WC content according to the following equation:

$$b_{Zr_yW_{1-y}C} = 0.4693 - 0.0390(1-y) \quad [nm] \tag{3.1}$$

Thus, the crystallographic interplanar spacings as determined from XRD spectra can be used to estimate the average composition of the solid solution. The lattice parameter for cubic symmetries is readily calculated for indexed crystallographic planes by:

$$d_{hkl} = \frac{b}{(h^2 + k^2 + l^2)} \tag{3.2}$$

The calculated average lattice parameter from the observed reflections is shown below (Table 15):

Table 15: Calculated lattice parameter for nominally $Zr_{0.60}W_{0.40}C$ heat treated at 2250°C for 1 hour

h	k	l	d (nm)	b (nm)
1	1	1	0.261	0.452
2	0	0	0.227	0.454
2	2	0	0.160	0.453
3	1	1	0.137	0.454
2	2	2	0.131	0.454
			Average	0.453
			Standard Deviation	0.001

The d-spacings and lattice parameters have been reported to three significant figures, as the pattern fitting was performed without an internal standard. (A deviation in calculated lattice parameter of 0.001 nm corresponds to an error of 0.1 degrees 2θ using Cu Kα1 radiation for the (111) peak, likely in excess of the true error.) The calculated lattice parameter corresponds to a composition of 42 ± 3 mol. % WC in solid solution, in close agreement with the estimated overall composition.

Immersion of this solid solution in $Zr_{14}Cu_{51}$ at 1300°C for 24 hours resulted in complete reaction to form W and ZrC, as shown by XRD of a polished cross-section (Figure 82):

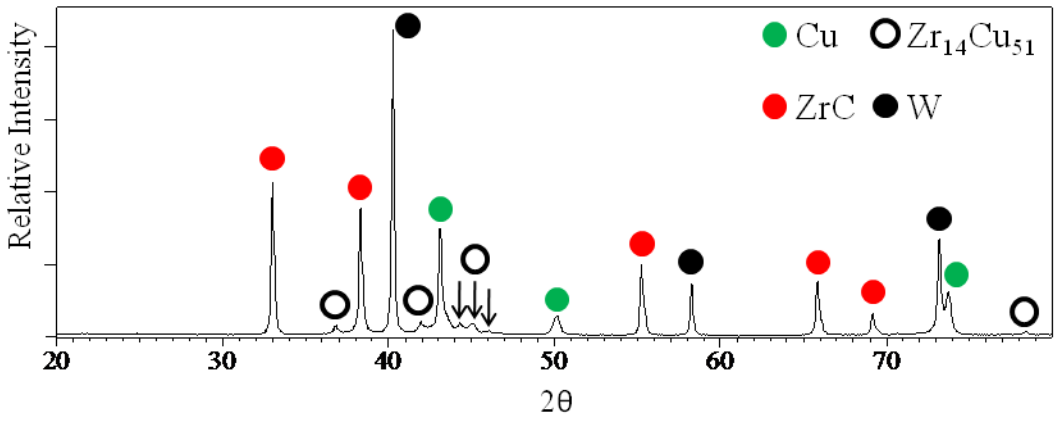

Figure 82: XRD analysis of $Zr_{0.58}W_{0.42}C$ immersed in $Zr_{14}Cu_{51}$ (1300°C for 24 hours) (PDF Card No. for W 04-0806, Cu 04-0836, ZrC 56-0159, $Zr_{14}Cu_{51}$ 42-1185)

The observed microstructure of the reactively infiltrated specimen is shown below (Figure 83):

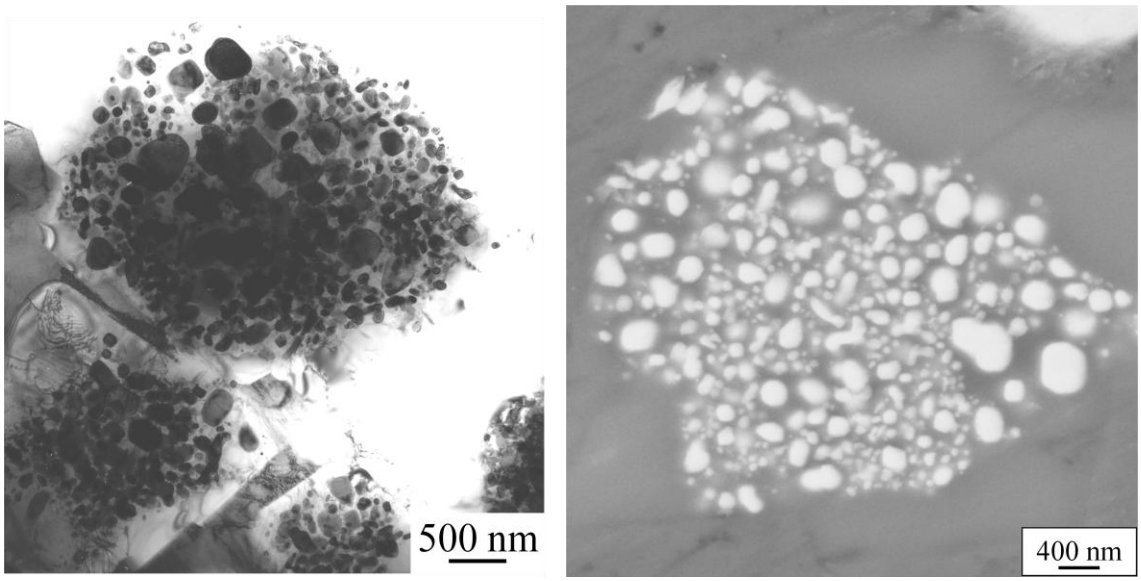

Figure 83: TEM and BSE images of reactively infiltrated $Zr_{0.58}W_{0.42}C$ (1300°C for 24 hours in $Zr_{14}Cu_{51}$) (TEM courtesy of Dr. Ye Cai)

The presence of relatively large precipitates (> 400 nm in diameter) indicates that W must be able to diffuse over at least this distance through the $Zr_yW_{1-y}C$ solid solution and/or ZrC matrix. This suggests that there may exist short-circuit diffusion pathways within the matrix (e.g. – perhaps due to a high density of dislocations). Further characterization via HRTEM is required to determine the mechanism by which W can apparently diffuse rapidly during reaction to produce relatively large precipitates.

TEM/SAED analysis of the ZrC cladding layer and the interior of the particle consisting of W precipitates in a ZrC matrix is shown below (Figure 84):

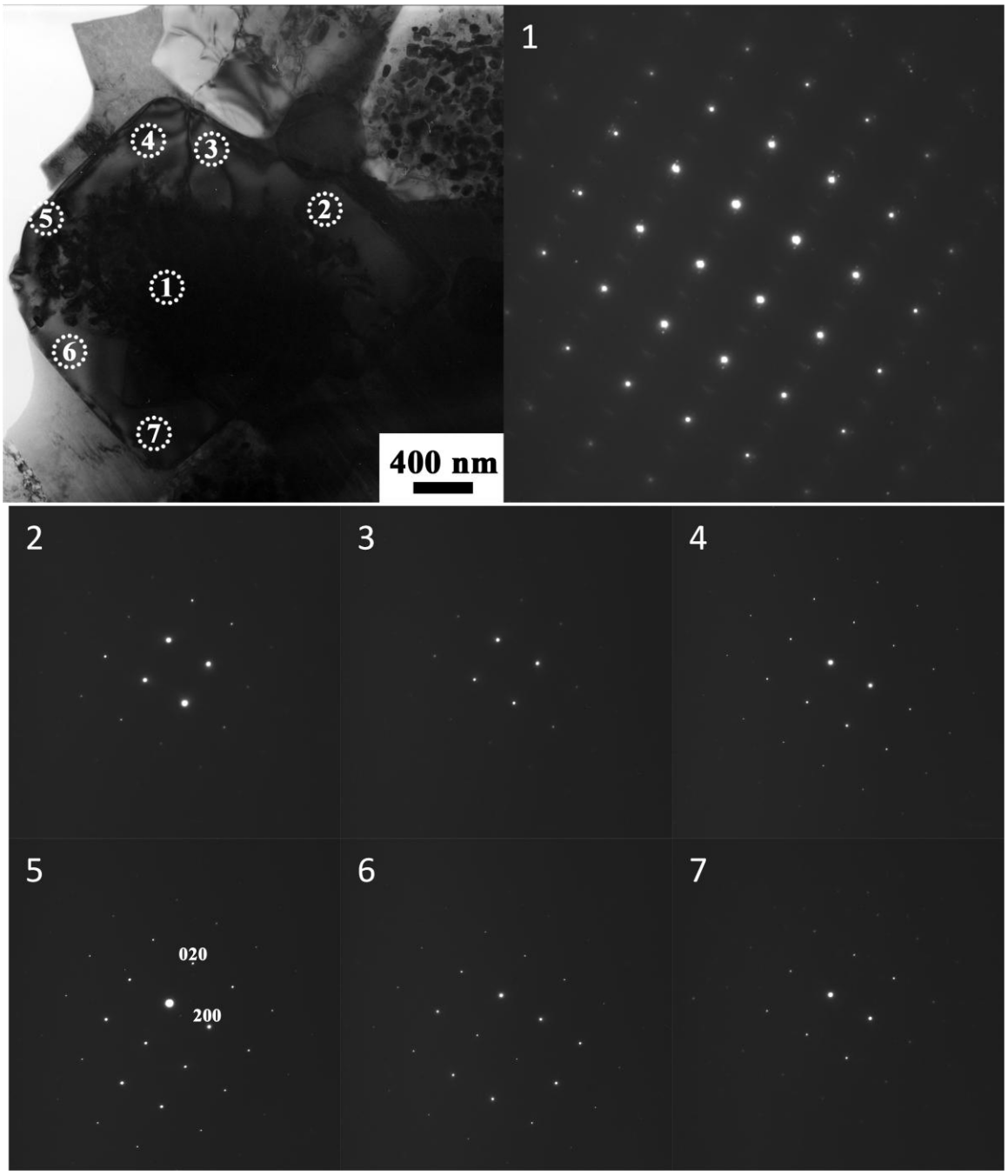

Figure 84: SAED patterns for indicated locations in and around a reacted $Zr_{0.58}W_{0.42}C$ grain showing epitaxy of ZrC layer with inner ZrC matrix (1300°C for 24 hours in $Zr_{14}Cu_{51}$) (TEM/SAED courtesy of Dr. Ye Cai)

Electron diffraction patterns reveal a single crystal ZrC matrix (position 1 in Figure 84). The ZrC layer formed by reaction with the melt at the perimeter of the grain contained no W precipitates and consisted of single crystal ZrC of the same orientation as the interior

matrix, indicating epitaxial growth of the product layer (positions 2 through 7 in Figure 84). Indexing of the observed electron diffraction pattern taken from the interior of the reacted particle (position 1 in Figure 84) showed an orientational relationship between the ZrC matrix and W precipitates (Figure 85):

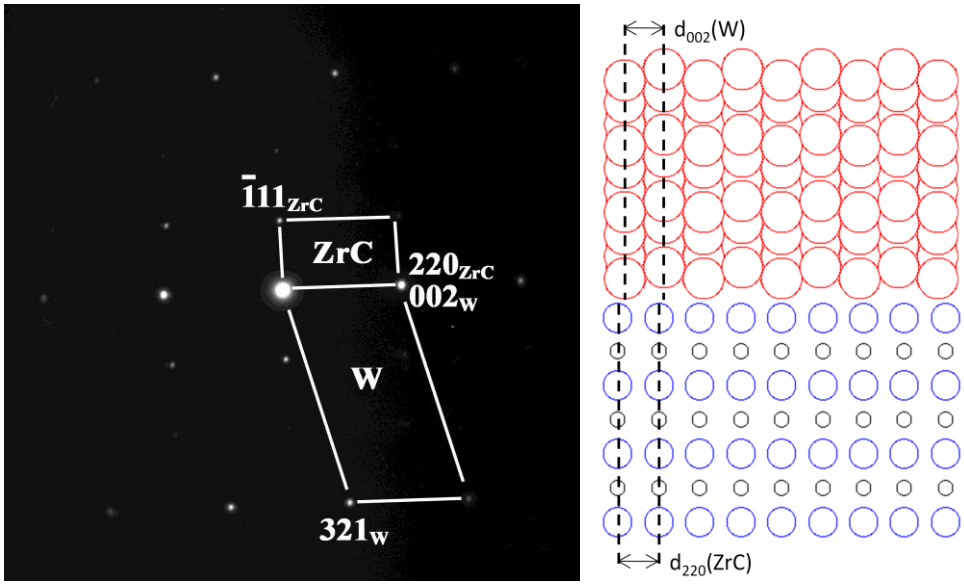

Figure 85: SAED pattern and schematic of orientational relationship between the ZrC matrix and W precipitates in reactively infiltrated $Zr_{0.58}W_{0.42}C$ (1300°C for 24 hours in $Zr_{14}Cu_{51}$) (SAED courtesy of Dr. Ye Cai)

The calculated lattice mismatch at the $(002)_W//(220)_{ZrC}$ interface was 4.65%.

A similarly-prepared sample, consisting of 5 mol. % WC in solid solution with unmilled ZrC powder, was solid solutionized at 2250°C for 4 hours. XRD analysis (Figure 86) revealed asymmetrical peak broadening, indicative of a range of inhomogeneous solid solution compositions present throughout the sample.

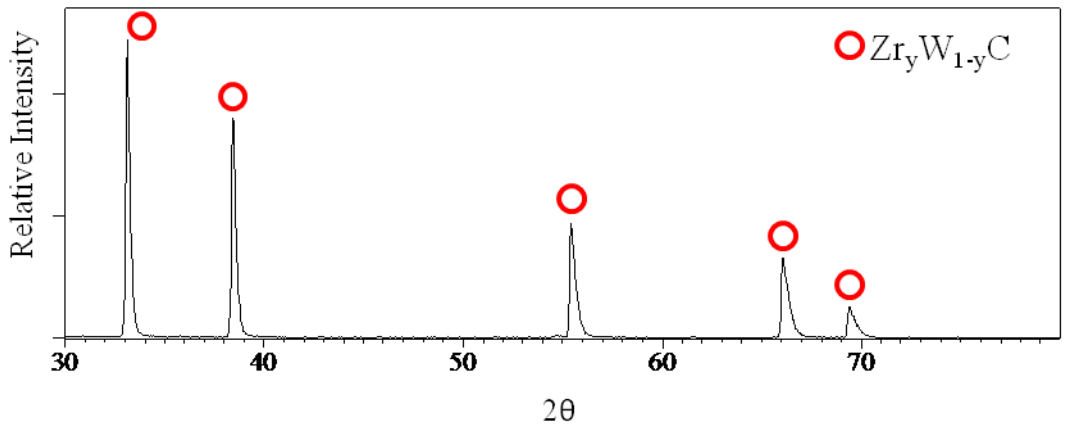

Figure 86: XRD analysis of 95 mol.% ZrC, 5 mol.% WC solid solution after 2250°C for 4 hours

The average solid solution lattice parameter, as determined by the peak position at maximum peak intensity, was calculated in the manner as previously described (Table 16):

Table 16: Calculated lattice parameter for nominally $Zr_{0.95}W_{0.05}C$ heat treated at 2250°C for 4 hours

h	k	l	d (nm)	b (nm)
1	1	1	0.270	0.468
2	0	0	0.234	0.468
2	2	0	0.166	0.470
3	1	1	0.141	0.468
2	2	2	0.135	0.468
			Average	0.468
			Standard Deviation	0.001

The calculated lattice parameter corresponds to a composition of 3 ± 3 mol. % WC in solid solution. The total WC content in solid solution was likely higher than this value, as the broadened shoulders of the XRD pattern corresponded to compositions with smaller lattice parameters, indicating the presence of solid solutions with higher WC contents.

The structure of nanocomposite particles produced by immersion of this solid solution in molten $Zr_{14}Cu_{51}$ at 1300°C for 2 hours is shown below (Figure 87):

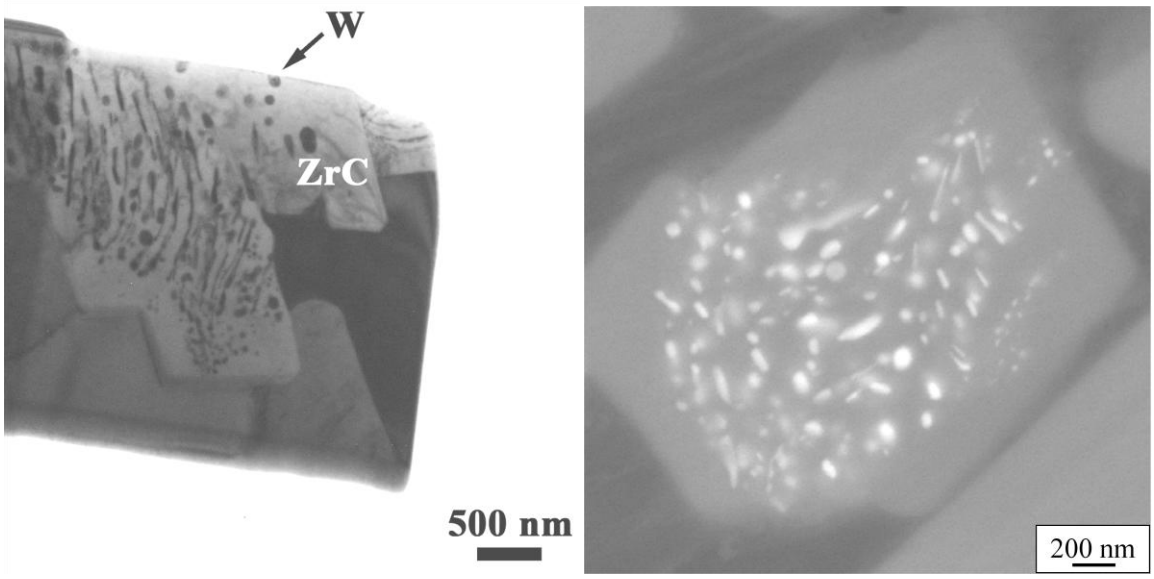

Figure 87: Backscattered electron images of reactively infiltrated $Zr_{0.95}W_{0.05}C$ (1300°C for 2 hours in $Zr_{14}Cu_{51}$) (TEM courtesy of Dr. Ye Cai)

Lamellar structures were observed in addition to nanoparticles, though the composition and mechanism of formation of these structures has yet to be determined. The nanoparticles have been identified as W by SAED analysis and exhibited an orientational relationship with the ZrC matrix (Figure 88):

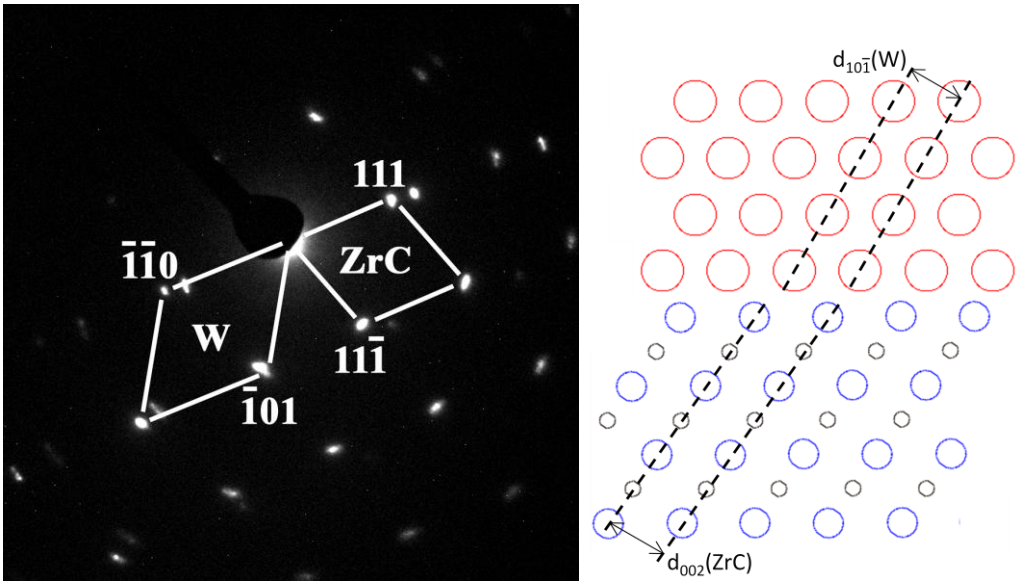

Figure 88: SAED pattern and schematic of orientational relationship between ZrC matrix and W precipitates in reactively infiltrated $Zr_{0.95}W_{0.05}C$ (1300°C for 2 hours in $Zr_{14}Cu_{51}$) (SAED courtesy of Dr. Ye Cai)

The calculated lattice mismatch at the $(10\bar{1})_W//(002)_{ZrC}$ interface was 4.60%.

3.5. *Discussion*

The interaction of a reactive fluid (as a pure gas or liquid, or a mixture or alloy thereof) with solid solution ceramic particles to produce nanoprecipitates can be described by reactions of the following type:

$$A_yM_{1-y}X + (1-y)\{R\} \leftrightarrow yAX + (1-y)M + (1-y)RX \quad (3.3)$$

where M is a metal; X is boron, carbon, nitrogen, or oxygen; $A_yM_{1-y}X$ is a ceramic solid solution; and {R} refers to a reactive metal constituent of the infiltrating fluid. An intragranular metal-reinforced ceramic micro/nanocomposite particle morphology is shown schematically in Figure 89:

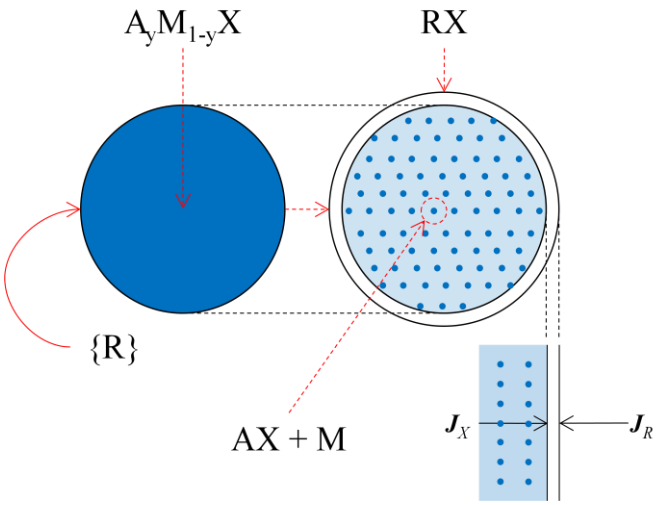

Figure 89: Schematic of internal reduction of solid solution ceramic particle

In order to assure selective reduction and precipitation of nanoparticles of a single metal species, the starting ceramic solid solution should consist of ceramic phases containing metals with dissimilar thermochemical stabilities. For example, at a typical processing

temperature of 1300°C, the standard Gibbs free energy of formation per mole of carbon, boron, nitrogen or oxygen is tabulated below for some common ceramic phases (Table 17):

Table 17: Standard Gibbs free energies of formation at 1300°C for some common ceramic phases

Phase	$\Delta G^0_{f,1300°C}$ (kJ/mol per mol C)	Phase	$\Delta G^0_{f,1300°C}$ (kJ/mol per mol B)
HfC	-201.0	HfB_2	-155.7
ZrC	-180.9	ZrB_2	-145.9
TiC	-165.3	VB	-126.7
TaC	-140.4	TiB_2	-125.5
NbC	-133.1	NbB_2	-118.4
VC	-84.5	MoB	-106.4
YC_2	-70.1	TaB_2	-97.2
LaC_2	-62.4	WB	-74.0
SiC	-59.1	AlB_2	-64.9
Cr_3C_2	-54.5	CrB_2	-41.1
CaC_2	-50.2	MgB_2	-32.1
Al_4C_3	-35.1	CaB_6	-10.7
WC	-34.5	LaB_6	-10.0
MoC	-29.2	SiB_{14}	-5.2

Phase	$\Delta G^0_{f,1300°C}$ (kJ/mol per mol N)	Phase	$\Delta G^0_{f,1300°C}$ (kJ/mol per mol O)
HfN	-227.6	Y_2O_3	-484.7
ZrN	-217.3	CaO	-466.5
TiN	-189.4	La_2O_3	-449.2
AlN	-144.4	HfO_2	-416.7
YN	-140.6	ZrO_2	-402.1
LaN	-133.5	Al_2O_3	-390.6
TaN	-129.7	TiO_2	-330.5
NbN	-87.9	SiO_2	-316.1
VN	-82.2	Ta_2O_5	-274.4
Si_3N_4	-58.0	Nb_2O_5	-245.4
Ca_3N_2	-50.4	Cr_2O_3	-242.8
Cr_2N	-11.4	V_2O_5	-184.8
W_2N	35.8	WO_3	-149.6
Mo_2N	42.325	MoO_3	-128.2

The general trend for chemical stability of these ceramic phases can be estimated by the electronegativity difference of the metal and non-metal elements. Metallic elements can be broadly classified into two types based on their electronegativities: strong metals and weak metals. Strong metals are those that have relatively low electronegativities while weak metals have relatively high electronegativities with respect to bonding non-metals such as boron, carbon, nitrogen or oxygen. The electronegativity difference between the strong metal and non-metal is substantially greater than the difference between the weak metal and non-metal, which can result in a large difference in chemical stability of the strong metal ceramic phase versus the weak metal ceramic phase. Although the original development of the Pauling electronegativity scale was based on the correlation between the enthalpy of formation of gas molecules having single covalent bonds with elemental electronegativities[114,115], numerous studies have further developed the relationship between the nature of chemical bonds and electronegativities[116,117,118,119]. The local environment of an atom in the crystalline state varies significantly from the molecular state; therefore, the electronegativity of atoms in the crystalline state may vary from standard values based on molecular data[118]. Nevertheless, the standard Gibbs free energy of formation of ceramic phases is correlated with electronegativity difference, as evidenced by qualitative trends observed for transition metal ceramics in groups IV-VI (Figure 90-Figure 94):

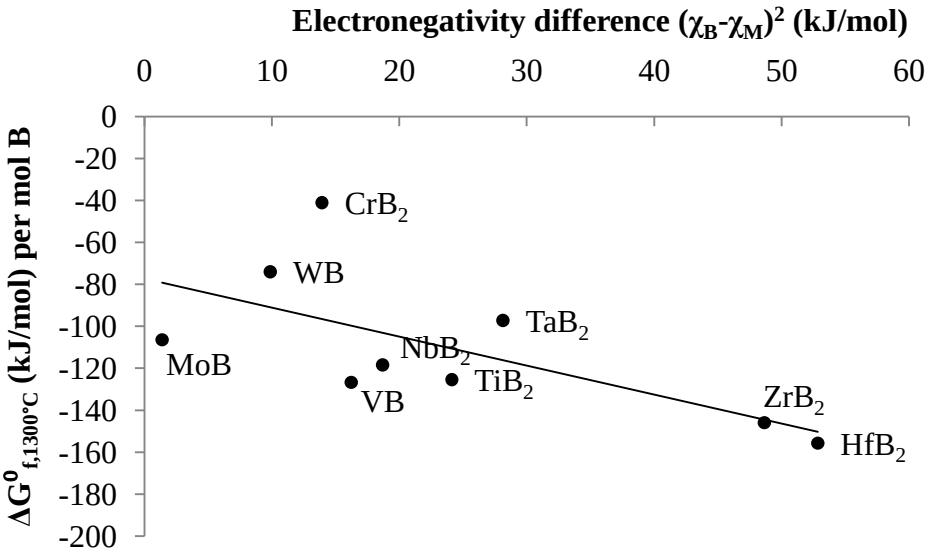

Figure 90: Correlation of phase stability with electronegativity difference for borides

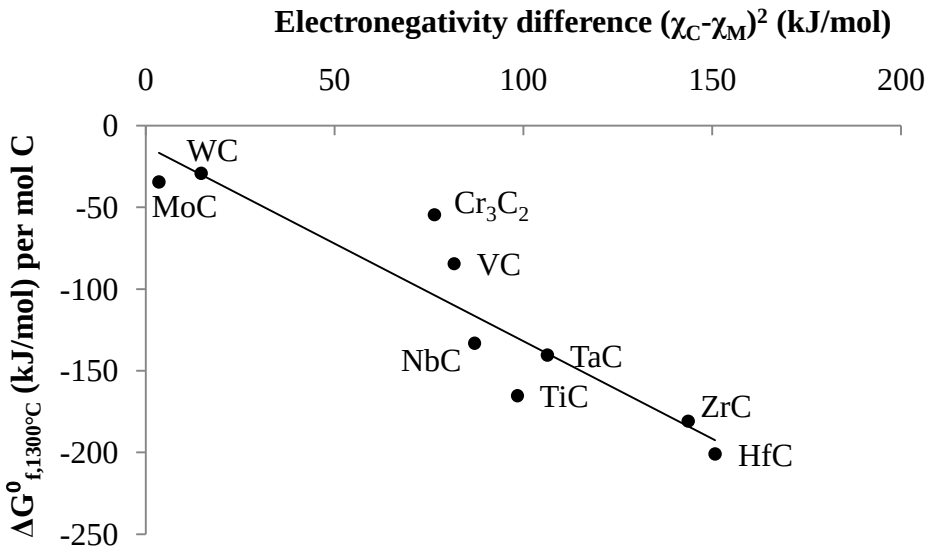

Figure 91: Correlation of phase stability with electronegativity difference for carbides

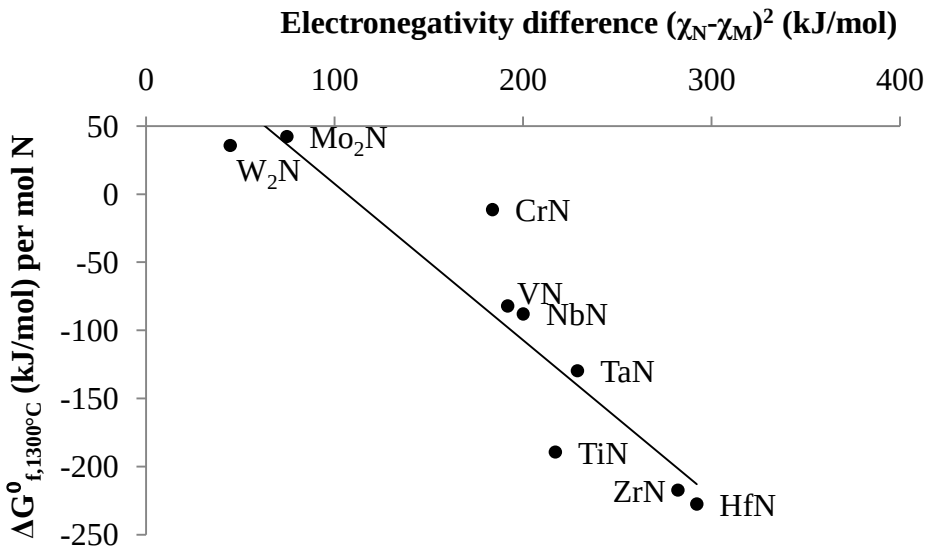

Figure 92: Correlation of phase stability with electronegativity difference for nitrides

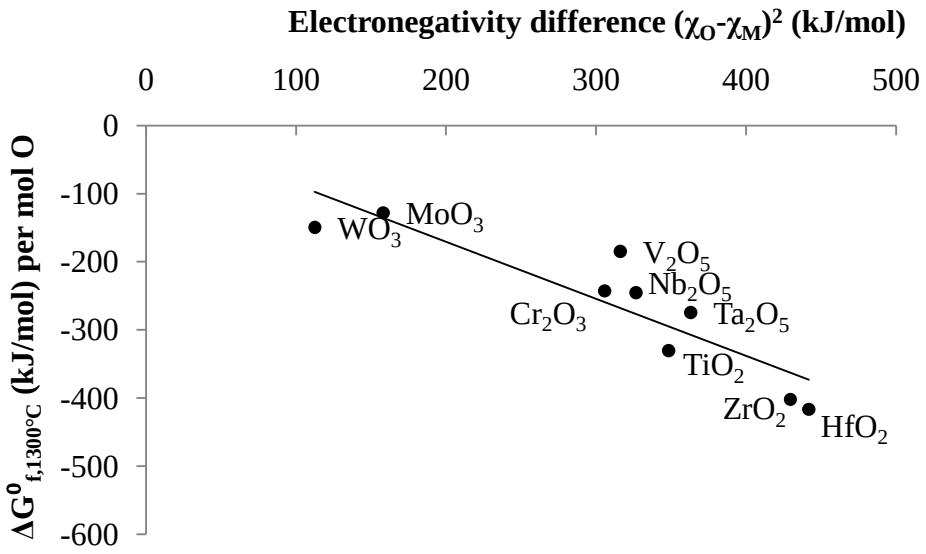

Figure 93: Correlation of phase stability with electronegativity difference for oxides

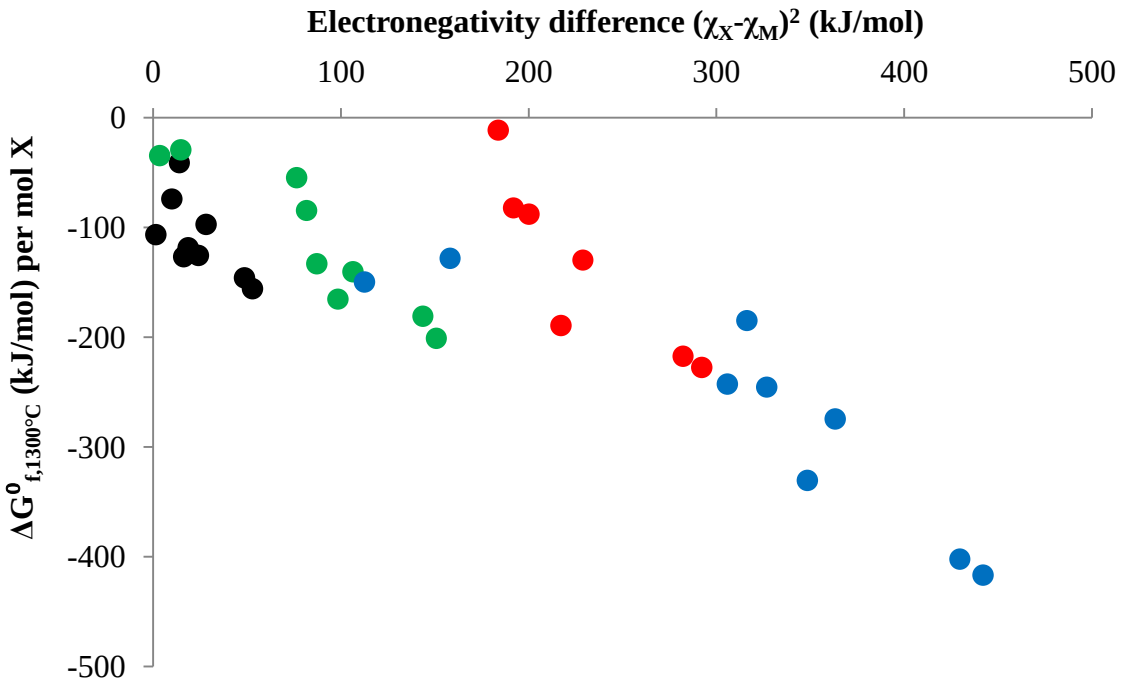

Figure 94: Master plot of correlation of phase stability with electronegativity difference for Group IV-VI transition metal borides (green), carbides (black), nitrides (red) and oxides (blue)

Deviations in correlation of standard Gibbs free energy of ceramic phases with electronegativity difference correspond to variances in the electrochemical environment of the atoms arising from differences in crystal structure, bond coordination, and ionic/covalent character of the bonding. Tungsten, having the second-highest Pauling electronegativity of any d-block transition metal (only gold is higher), has weakly stable carbides, borides and oxides at 1300°C (the nitrides are unstable at high temperatures). Therefore, W-bearing ceramic phases in suitably chosen solid solutions are ideal candidates to be selectively reduced to form W precipitates.

Indeed, tungsten-bearing intragranular micro/nanocomposites have been fabricated via the following reaction:

$$Zr_yW_{1-y}C + (1-y)\{Zr\} \leftrightarrow yZrC + (1-y)W + (1-y)ZrC \qquad (3.4)$$

where ZrC and WC can be formed as complete solid solutions[109,110,111], designated as $Zr_yW_{1-y}C$ in the reaction above, and {Zr} is a liquid alloy of Zr with one or more inert elements (such as Cu) typically chosen to lower the processing temperature (though pure Zr can be used as an infiltrating liquid at process temperatures above its melting point of 1855°C, the solubility of W in Zr at this temperature is approximately 12 at. %, and a eutectic temperature of 1735°C exists for eutectic composition 9 at. % W in Zr[120]). When AX and M have limited mutual solid solubilities, this reaction can generate precipitates whose characteristic length scale is proportional to the distance over which diffusion can occur under the processing conditions. (As discussed in Chapter 1, the solubility of W in ZrC is limited to 7 mol. % at the eutectic temperature of 2800°C and is practically insoluble at lower temperatures[121].)

This process represents an extension of the technique to form metal/oxide intragranular micro/nanocomposites via the internal reduction of oxide solid solutions with hydrogen gas mixtures[122,123,124,125]. The overall reaction scheme can be represented as:

$$A_yM_{1-y}O + (1-y)H_2(g) \leftrightarrow yAO + (1-y)M + (1-y)H_2O(g) \quad (3.5)$$

This reaction is thermodynamically driven principally by the stability of H_2O(g) relative to the metal oxide MO in solid solution. Reaction with H_2(g) is unfavorable for non-oxide ceramics since hydrogen compounds of boron, carbon, and/or nitrogen generally are not of greater thermodynamic stability relative to the unreduced metal borides, carbides, or nitrides. In other words, the following types of reactions are typically unfavorable:

$$2MB + yH_2(g) \leftrightarrow 2M + 2BH_y(g) \quad (3.6)$$
$$2MC + yH_2(g) \leftrightarrow 2M + 2CH_y(g) \quad (3.7)$$

$$2MN + yH_2(g) \leftrightarrow 2M + 2NH_y(g) \quad (3.8)$$

These reactions become even less favorable when the free energy of mixing of the solid solution to reduce metal M is taken into account. The choice of a suitable reacting fluid is essential to thermodynamically drive the reduction of borides, carbides and nitrides to their respective metals. (For a properly chosen combination of strong and weak metals in the solid solution, the choice of a suitable fluid is simplified if one chooses a fluid containing the strong metal as reactive component.)

Upon precipitation of the weak metal, orientational relationships with the single crystal strong metal ceramic-enriched matrix have been observed. Possible orientational relationships between W and ZrC with lattice mismatches less than 10% are tabulated below (Table 18):

Table 18: Low lattice mismatch combinations for W/ZrC interfaces (observed orientational relationships highlighted)

W	ZrC	Lattice Mismatch	Average Planar Density (atoms/nm^2)
(222)	(511)	1.16%	6.38
(321)	(440)	1.93%	5.88
(220)	(331)	3.75%	7.70
(310)	(422)	4.29%	6.86
(110)	(200)	4.60%	16.14
(222)	(422)	4.61%	6.59
(310)	(420)	4.63%	7.22
(211)	(222)	4.63%	9.32
(400)	(440)	4.63%	5.71
(200)	(220)	4.65%	11.41
(220)	(400)	4.66%	8.07
(220)	(420)	6.21%	8.07
(321)	(511)	6.34%	6.16
(310)	(331)	7.06%	7.32
(211)	(311)	8.69%	9.55
(211)	(400)	9.17%	8.62
(222)	(440)	9.20%	6.74
(310)	(511)	9.76%	6.65

The observed W/ZrC orientational relationships from reacted particles shown in Figure 83 and Figure 87 were found to involve the crystallographic planes with the highest average atomic densities. Since highly-packed planes have relatively large in-plane bond densities, it is postulated that interfacial energy is minimized by parallel arrangement of these planes across the grain boundary. Further characterization of W/ZrC grain boundaries is required to develop a statistical description of the frequency of occurrence of each orientational relationship, which is expected to provide a more complete understanding of the relationships between lattice mismatch, average atomic density of the crystallographic planes at the interface, and interfacial energy of the grain boundaries.

3.6. *Conclusions*

A general method for the internal reduction of ceramic solid solutions to produce metal/ceramic intragranular micro/nanocomposites has been proposed and demonstrated for the refractory ZrC/W composite system. Criteria that must be satisfied in order the successfully produce metal/ceramic nanocomposites include:

- A solid solution consisting of ceramic phases with dissimilar thermochemical stabilities must exist,
- A suitable reactive fluid must exist to selectively reduce the solid solution,
- Weak metal precipitates must exhibit limited mutual solid solubility in the strong-metal enriched ceramic matrix,
- The processing temperature must be high enough to enable solid state diffusion of the non-metallic element out of the solid solution particle, and
- The processing temperature must be low enough so as to limit the rate of diffusion of the weak metal atoms in order to limit precipitate grain growth.

Further study is required to determine precipitation pathways and mechanisms. The occurrence of orientational relationships between precipitate and matrix phases, as well as the matrix phase and product layer, also is poorly understood.

Future experiments are also suggested to gain greater control over intragranular micro/nanostructures. One possible method to achieve this goal would involve precipitation of weak metal ceramic nanostructures via annealing supersaturated solid solutions prior to internal reduction. For example, WC nano-platelets have been observed during the annealing of supersaturated $Zr_yW_{1-y}C$[109]. These structures could be reduced *in-*

situ to create highly aspected intragranular metal nanostructures, in addition to metal precipitates formed directly via internal reduction of the solid solution.

The application of this process to the vast number of possible combinations of ceramic solid solutions also merits further study. The internal reduction of boride and nitride solid solutions has yet to be demonstrated. The internal reduction of ternary or higher multicomponent solid solutions has also yet to be demonstrated and may yield interesting behaviors. For example, consider two ternary solid solutions consisting, on the one hand, of two weak metal ceramics and one strong metal ceramic and, on the other hand, one weak metal ceramic and two strong metal ceramics. In the first case, it is unclear how the precipitation of two weak metals would proceed. This case can be further classified on the basis of whether the two weak metals exhibit mutual solubilities and/or can form intermetallic compounds. In the second case, it is unclear how the microstructure of the matrix phase consisting of two strong metal ceramics will evolve (i.e. – if a single crystal solid solution remains stable or if the grain structure becomes more complex).

Lastly, opportunities for further study exist in determining microstructure-property relationships. The effects of volume percent precipitates, precipitate morphology and matrix/precipitate interfacial strength on thermomechanical behavior have yet to be determined.

3.7. *References*

[91] Gleiter, H. "Nanostructured materials: basic concepts and microstructure," *Acta Mater.*, **48**, 1-29 (2000).

[92] Meyers, M.A., Mishra, A. and Benson, D.J. "Mechanical properties of nanocrystalline materials," *Prog. Mater. Sci.*, **51**, 427-556 (2006).

[93] Sternitzke, M. "Review: structural ceramic nanocomposites," *J. Euro. Ceram. Soc.*, **17**, 1061-1082 (1997).

[94] Kumar, K.S., Van Swygenhoven, H. and Suresh, S. "Mechanical behavior of nanocrystalline metals and alloys," *Acta Mater.*, **51**, 5753-5774 (2003).

[95] Dao, M., Lu, L., Asaro, R.J., DeHosson, J.T.M. and Ma, E. "Toward a quantitative understanding of mechanical behavior of nanocrystalline metals," *Acta Mater.*, **55**, 4041-4065 (2007).

[96] Moya, J.S., Lopez-Esteban, S. and Pecharroman, C. "The challenge of ceramic/metal microcomposites and nanocomposites," *Prog. Mater. Sci.*, **52**, 1017-1090 (2007).

[97] Niihara, K. "New design concept of structural ceramics - ceramic nanocomposites," *J. Ceram. Soc. Japan*, **99**(10), 974-982 (1991).

[98] Chen, I.W. and Wang, X.H. "Sintering dense nanocrystalline ceramics without final-stage grain growth," *Nature*, **404**, 168-171 (2000).

[99] Groza, J.R. and Dowding, R.J. "Nanoparticulate materials densification," *Nanostructured Mater.*, **7**(7), 749-768 (1996).

[100] Kirchhoff, M., Specht, U. and Veser, G. "Engineering high-temperature stable nanocomposite materials," *Nanotech.*, **16**, S401-S408 (2005).

[101] Loureiro, S.M., Ramos, M.L. and Manoharan, M. "High temperature nanocomposite through engineered synthesis of hafnia nano-dispersoids in hexagonal mesoporous silica," *J. Am. Ceram. Soc.*, **88**(4), 1072-1075 (2005).

[102] Sekino, T. and Niihara, K. "Fabrication and mechanical properties of fine-tungsten-dispersed alumina-based composites," *J. Mater. Sci.*, **32**, 3943-3949 (1997).

[103] Nawa, M., Yamazaki, K., Sekino, T. and Niihara, K. "A new type of nanocomposite in tetragonal zirconia polycrystal-molybdenum system," *Mater. Letters*, **20**, 299-304 (1994).

[104] Bhaduri, S. and Bhaduri, S.B. "Recent developments in ceramic nanocomposites," *JOM*, **50**(1), 44-51 (1998).

[105] Tjong, S.C. and Ma, Z.Y. "Microstructural and mechanical characteristics of in situ metal matrix composites," *Mater. Sci. Eng. R.*, **29**, 49-113 (2000).

[106] Oberdorster, G., Oberdorster, E. and Oberdorster, J. "Nanotoxicology: an emerging discipline evolving from studies of ultrafine particles," *Environ. Health Perspect.*, **113**(7), 823-839 (2005).

[107] Nel, A., Xia, T., Madler, L. and Li, N. "Toxic potential of materials at the nanolevel," *Science*, **311**, 622-627 (2006).

[108] Lewinski, N., Colvin, V. and Drezek, R. "Cytotoxicity of nanoparticles," *Small*, **4**(1), 26-49 (2008).

[109] Brun, M. and Stubican, V.S. "Precipitation studies in the system WC-ZrC," *J. Am. Ceram. Soc.*, **57**(3),117-119 (1974).

[110] Matsumoto, O., Hirose, H., Kawara, Y. and Ohue, T. "Formation and properties of cubic solid solutions in the W-Ti-C, W-Zr-C, and W-Hf-C systems," *High Temp. Sci.*, **9**(1), 27-34 (1977).

[111] Kuz'ma, Y.B., Federov, T.F. and Shvets, E.A. "Phase equilibria in the system Zr-W-C," *Powder Met. and Metal Ceram.*, **4**(2), 106-109 (1965).

[112] Perevislov, S.N., Panteleev, I.B. and Ordan'yan, S.S. "Synthesis of complex tungsten-zirconium carbonitrides," *Russ. J. Appl. Chem.*, **78**(11), 1767-1771 (2005).

[113] Holleck, H. *Binary and Ternary Transition Metal Carbide and Nitride Systems*. Gebruder Borntraeger, Verlagsbuchhandlung, 1984.

[114] Pauling, L. "The nature of the chemical bond. IV. the energy of single bonds and the relative electronegativity of atoms," *J. Am. Chem. Soc.*, **54**(9), 3570-3582 (1932).

[115] Pauling, L. "The origin and nature of the electronegativity scale," *J. Chem. Edu.*, **65**(4), 375 (1988).

[116] Mulliken, R.S. "Electronic structures of molecules XI. Electroaffinity, molecular orbitals and dipole moments," *J. Chem. Phys.*, **3**(9) 573-585 (1935).

[117] Allred, A.L. "Electronegativity values from thermochemical data," *J. Inorg. Nucl. Chem.*, **17**, 215-221 (1961).

[118] Sanderson, R.T. "Electronegativity and bonding of transitional elements," *Inorg. Chem.*, **25**, 3518-3522 (1986).

[119] Nagle, J.K. "Atomic polarizability and electronegativity," *J. Am. Chem. Soc.*, **112**, 4741-4747 (1990).

[120] Alcock, C.B., et al. *Zirconium: Physico-Chemical Properties of Its Compounds and Alloys,* O. Kubaschewski, Ed., Atomic Energy Review Special Issue No. 6, International Atomic Energy Agency, Vienna (1976).

[121] Eremenko, V.N., Velikanova, T.Y., Artyukh, L.V., Aksel'rod, G.M. and Vishnevskii, A.S. *Dopov. Akad. Nauk Ukr. RSR, Ser. A: Fiz.-Mat. Tekh. Nauki*, 1, 80-85 (1976). From *Phase Diagrams for Zirconium and Zirconia Systems*, H. M. Ondik and H. F. Mcmurdie (ed.), American Ceramic Society, 2005.

[122] Rousset, A. "Alumina-metal (Fe, Cr, Fe0.8Cr0.2) nanocomposites," *J. Solid State Chem.*, **111**, 164-171 (1994).

[123] Backhaus-Ricoult, M. and Hagege, S. "Metal-ceramic interfaces in internally reduced (Mg,Cu)O," *Acta metall. mater.*, **40**, S267-S274 (1992).

[124] Ustundag, E., Subramanian, R., Vaia, R., Dieckmann, R. and Sass, S.L. "In situ formation of metal-ceramic microstructures, including metal-ceramic composites, using reduction reactions," *Acta metall. mater.*, **41**(7), 2153-2161 (1993).

[125] Suetsuna, T., Fukasawa, T., Suenaga, S. and Harada, K. "Defect control in a selective reduction reaction to synthesize a metal/ceramic nanocomposite," *J. Am. Ceram. Soc.*, **90**(11), 3441-3448 (2007).

APPENDIX A: Sample Calculation of Composite Phase Contents

Suppose that a preform consisting initially of pure WC has a measured pore volume fraction of 53.7% (see Table 4). Suppose also that, after reaction, the W:WC molar ratio has been measured via quantitative XRD analysis to be 11.5 (the corresponding extent of reaction is 92% [equation (1.7)]). The average linear shrinkage of external dimensions of the part was -0.6% and the final composite bulk density has been measured to be 10.993 g/cm^3. From these measurements, the reaction stoichiometry consistent with equation (1.1), and materials data for W, WC, ZrC, and Cu (reproduced below from Table 3), the phase contents of the DCP-derived composite have been calculated as follows:

Phase (JCPDS PDF Card Number[29])	Molar Weight [g/mol]	Density [g/cm^3]	Molar Volume [cm^3/mol]
WC (25-1047)	195.861	15.667	12.502
W (04-0806)	183.850	19.259	9.546
ZrC (35-0784)	103.231	6.633	15.563
Cu (04-0836)	63.546	8.932	7.114

- The external volume of the preform is 12.502 cm^3/mol WC / (1-0.537) = 27.001 cm^3. Taking 1 mole WC as a basis for calculation, this corresponds to 12.502 cm^3 WC and (27.001-12.502) = 14.500 cm^3 pore volume.
- After 92% reaction, the remaining volume of WC is (1-0.92)*12.502 cm^3 WC = 1.000 cm^3 WC [equation (1.12)]
- The volume W generated is (0.92)*12.502 cm^3 WC*(9.546 cm^3/mol W /12.502 cm^3/mol WC)*(1 mol W/1 mol WC) = 8.782 cm^3 W [equation (1.13)]
- The volume ZrC generated is (0.92)*12.502 cm^3 WC*(15.563 cm^3/mol ZrC /12.502 cm^3/mol WC)*(1 mol ZrC/1 mol WC) = 14.318 cm^3 ZrC [equation (1.14)]

- The external volume of the composite is $(1\text{-}0.006)^3$*27.001 cm^3 = 26.518 cm^3 [equation (1.10)]
- The volume fractions of WC, W, and ZrC are 1.000 cm^3 WC/26.518 cm^3 = **0.038**, 8.782 cm^3 W/26.518 cm^3 = **0.331**, and 14.318 cm^3 ZrC/26.518 cm^3 = **0.540**, respectively [equation (1.11)]
- The volume fraction Cu in the pores is (10.993 g/cm^3 – 0.038*15.667 g/cm^3 WC – 0.331*19.259 g/cm^3 W – 0.540*6.633 g/cm^3 ZrC)/8.932 g/cm^3 Cu = **0.049** [equation (1.16)]
- The pore volume fraction is 1 – 0.038 – 0.331 – 0.540 – 0.049 = **0.042** [equation (1.17)]
- The solid volume fractions of ZrC, W, Cu, and WC are 0.540/(1-0.05) = **0.563**, 0.331/(1-0.05) = **0.346**, 0.049/(1-0.05) = **0.051**, 0.038/(1-0.05) = **0.039**, respectively [equation (1.18)] (see Table 4)

APPENDIX B: Fluid Dynamics Modeling

A commercial fluid dynamics modeling package (COMSOL 4.0a, COMSOL Inc., Burlington MA) has been employed to model the viscous gas film thickness above the substrate caused by friction. The model takes as input the kinematic viscosity of Ar at 1100°C (reported as 1.6 cm^2/s[126,127] in the literature) and density of Ar at 1100°C (calculated to be $3.9x10^{-4}$ g/cm^3 from the ideal gas law). The thickness of this layer has been found to be invariant with respect to inlet gas velocity in the range of 0.03-0.85 cm/s and reaches a constant thickness as function of position along the substrate within 1 mm from the leading edge:

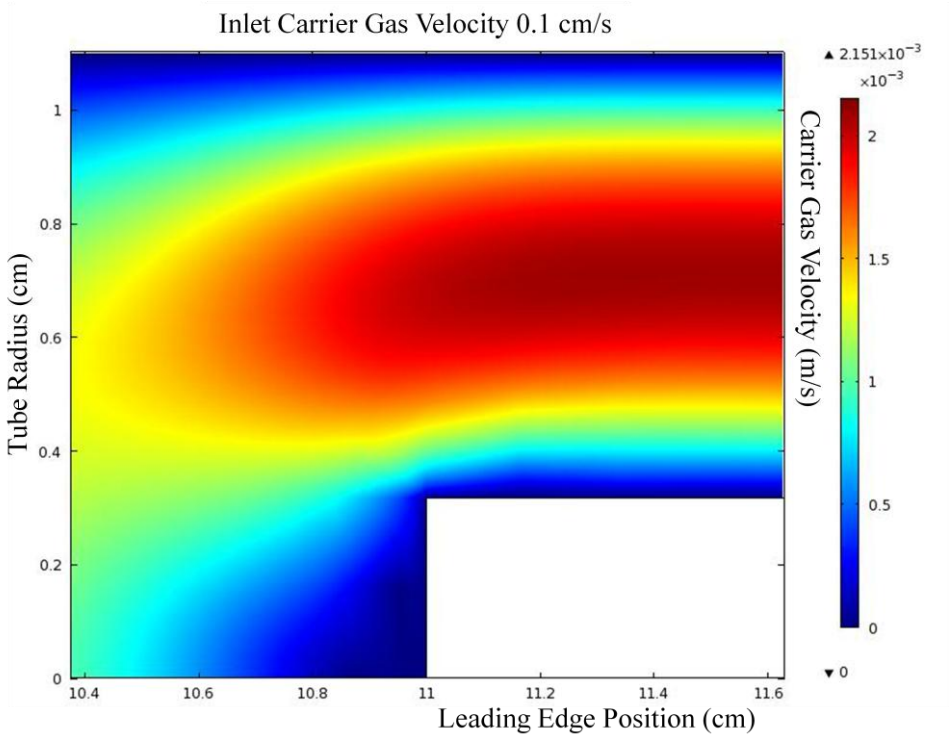

Figure 95: Carrier gas velocity distribution near leading edge of substrate for inlet carrier gas velocity of 0.1 cm/s

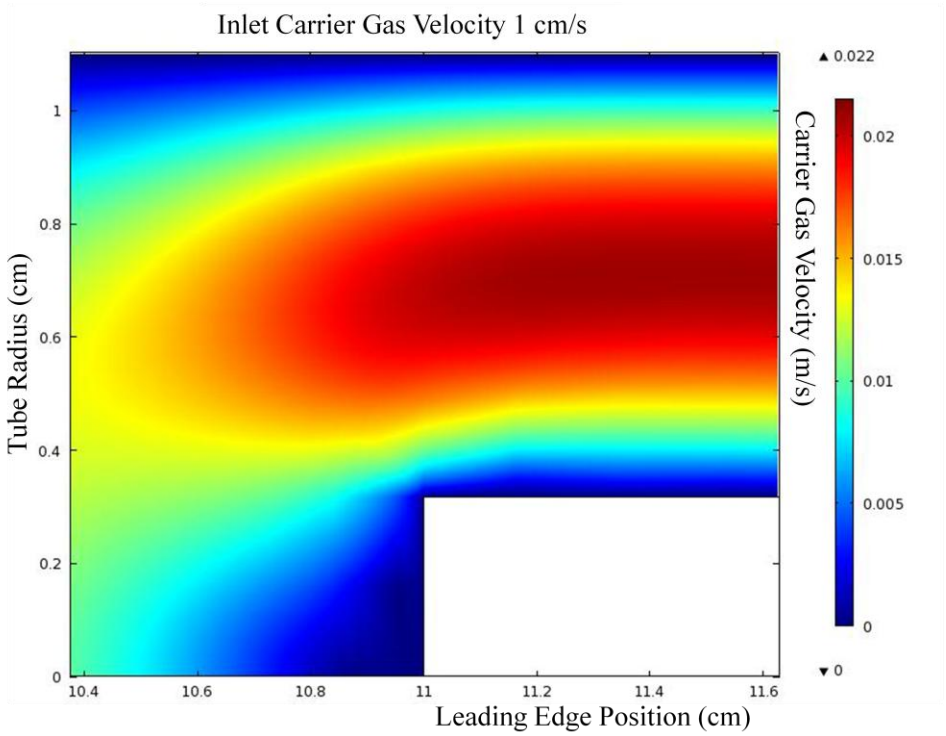

Figure 96: Carrier gas velocity distribution near leading edge of substrate for inlet carrier gas velocity of 1 cm/s

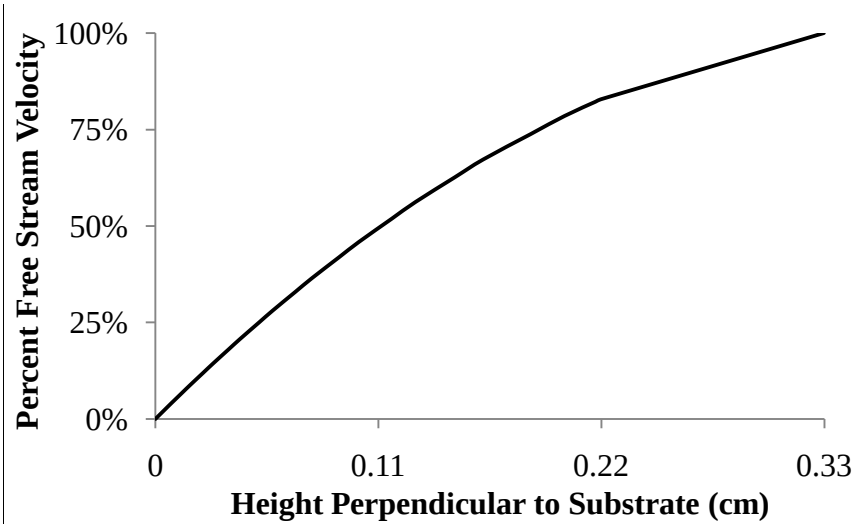

Figure 97: Simulated carrier gas velocity distribution perpendicular to the substrate at a distance of 1 cm from the leading edge for inlet carrier gas velocities from 0.1 – 1 cm/s

From the velocity profile perpendicular to the substrate, the viscous gas film layer has been modeled as a constant 0.33 cm thickness. This value represents the velocity

boundary layer thickness (δ_{film}), which differs from the concentration boundary layer thickness by:

$$\delta_{film}^{C} = \frac{\delta_{film}}{(Sc)^{1/3}} \tag{B.1}$$

where Sc is the Schmidt number, given by

$$Sc = \frac{\nu}{D} \tag{B.2}$$

defined as the ratio of the momentum diffusivity given by kinematic viscosity, *v*, to mass diffusivity given by mass diffusion coefficient, *D*. The kinetic data taken at a fixed inlet carrier gas velocity of 0.85 cm/s occurs at a calculated WO_2Cl_2 activity of 0.045 (see Table 12) and is thus modeled as a dilute mixture of WO_2Cl_2 in Ar. The diffusion coefficient of WO_2Cl_2 in Ar at 1100°C and 2.3 atm pressure can be calculated by Chapman-Enskog theory[128]:

$$D_{WO2Cl2}^{Ar} = 1.858x10^{-3} \frac{\sqrt{T^3 \left(\frac{1}{AW_{Ar}} + \frac{1}{MW_{WO2Cl2}}\right)}}{P\Omega^2\sigma^2} \tag{B.3}$$

where *T* is temperature (K), AW_{Ar} is the atomic weight of Ar (g/mol), MW_{WO2Cl2} is the molecular weight of WO_2Cl_2 (g/mol), *P* is pressure (atm), Ω is the collision integral (tabulated using the Leonard-Jones interaction energy ε), and σ is the average collision diameter of Ar and WO_2Cl_2 (Å). Data for common gases such as Ar are found in standard texts, though no data is available for WO_2Cl_2. As an approximation, data for the molecule WF_6[129] has been used since WF_6 and WO_2Cl_2 are both nonpolar gases of similar molecular weight. Data used in calculating the diffusion coefficient of dilute WO_2Cl_2 in Ar is summarized in the following Table 19:

Table 19: Data used for calculation of diffusion coefficient of WO_2Cl_2 in Ar

	AW/MW	σ(Å)	ε/k_B (K)
Ar	39.948	3.542	93.3
WO_2Cl_2	286.745	5.21 (WF_6)	338 (WF_6)

From the average collision diameter for Ar and WO_2Cl_2 (4.376 Å) and dimensionless interaction potential ($\frac{k_B T}{\epsilon}$ = 7.73), the collision integral is found from tabulated values as 0.7846[128]. Using these values in equation (B.3), the diffusion coefficient for WO_2Cl_2 in Ar is calculated to be 0.46 cm^2/s. Using this value, the Schmidt number for this system is calculated to be 3.2.

B.1. *References*

[126] Dawe, R.A. and Smith, E.B. "Viscosity of argon at high temperatures," *Science*, **163**(3868), 675-676 (1969).

[127] Suzuki, T. "Effect of annealing a silicon wafer in argon with a very low oxygen partial pressure," *J. Appl. Phys.*, **88**(11), 6881-6886 (2000).

[128] Plawsky, J.L. *Transport phenomena fundamentals*. New York, NY: Marcel Dekker, Inc., 2001.

[129] Kleijn, C.R., Hoogendoorn, C.J., Hasper, A., Holleman, J. and Middelhoek, J. "Transport phenomena in tungsten LPCVD in a single-wafer reactor," *J. Electrochem. Soc.*, **138**(2), 509-517 (1991).

APPENDIX C: Historical Perspective on Tungsten Lamp Filaments

The following excerpt has been reproduced from History of the Incandescent Lamp, pages 94-98, written by John W. Howell and Henry Schroeder (this work is now out of copyright and in the public domain)[80]. It has been provided due to the interesting historical relevance of the reactions discussed in Chapter 2.

"Alexander Just and Franz Hanaman, in 1902, were laboratory assistants to the professor of chemistry in the Technical High School in Vienna. Just was making use of his spare time by working in another laboratory trying to develop an incandescent lamp having a filament of boron. His means were very limited, his whole income being about $55 per month. In August, 1902, he got his co-worker Hanaman, whose monthly income was even less, to assist him. The two conceived the idea of trying to produce a tungsten filament lamp and they worked on both the boron and tungsten lamps for about two years. The boron lamp was a failure.

They first started experiments on the tungsten lamp by exposing a carbon filament at high temperature to the vapor of tungsten oxychloride in the presence of a small quantity of hydrogen. Their theory was that a complex chemical reaction takes place, depositing the tungsten of the oxychloride in place of the carbon, and that this reaction continues until the carbon of the filament has been entirely replaced by tungsten.

Their aim was to make a pure tungsten filament and, as they knew that tungsten was brittle and unworkable so that it could not be drawn out into a wire, they thought this carbon replacement method would finally produce a tungsten filament. This effort was a failure for the reason that the first thin coating of tungsten on the carbon filament prevents further action between the carbon and tungsten oxychloride vapor. This filament merely became one having a carbon core and a tungsten shell, and when operated at a temperature above that of the ordinary carbon lamp, the carbon would dissolve through the tungsten, vaporize, and quickly blacken the bulb, as in Bottome's scheme.

They were using a paste containing graphite and a binding material, such as coal tar, to fasten the filament to the leading-in wires. They found that much of the black deposit in the bulb came from this paste, so they heated the pasted joints in hydrogen gas and found that the blackening was very materially reduced. This led them to believe that there must be some de-carbonizing process going on. Being chemists they came to the conclusion that some oxidizing substance was acting as a go-between between the carbon and hydrogen. The hydrogen gas they obtained was produced by the action of hydrochloric acid and zinc, and they found that it contained a considerable amount of water vapor. They therefore reasoned that the high temperature decomposed the water vapor, the oxygen combining with the carbon.

Finally they evolved a process of making a substantially pure tungsten filament by coating a fine carbon filament with tungsten deposited by heating the carbon filament in a vapor of tungsten oxychloride as previously described. The coated filament was then

heated to a high temperature by passing current through it in an atmosphere of neutral gases which would not react on it chemically. This heating made the carbon core dissolve into the tungsten shell surrounding it, the carbon then being removed by another heating in an atmosphere of water vapor and hydrogen. Later the first heating was dispensed with, the second heating accomplishing the results obtained by the original first heating.

Another process was evolved by them, which was commercially used in this country for several years. It produced what was called the "pressed" filament and consisted of mixing tungsten powder with an organic binding material, of which there are several that can be used. In the commercial process, a very fine grained tungsten powder was mixed with a solution of sugar and gum arable to make a thick paste. This paste was squirted under high pressure through a diamond die and caught in loops on a piece of cardboard. Tungsten is so hard that it will soon wear out any other than a diamond die. The loops were baked enough to partly carbonize the binder and then were passed through a "forming" machine in which electric current of increasing amount was passed through them while they were in an atmosphere of hydrogen and nitrogen which contained some moisture. This removed the binder and left substantially pure tungsten in the filaments.

Just and Hanaman found that the substantially pure tungsten filament they were able to make could be operated at about 7% lumens per watt and yet give good life results. This was an enormous improvement over all previous lamps made. Their financial resources by this time were so depleted that they did not have sufficient money to apply for patents to protect their invention in all the various European countries. They finally were able to borrow $60 from a chemical manufacturer in Vienna with which to apply for British and French patents, which were filed on Nov. 4, 1904.

They found it difficult to obtain financial assistance to develop their invention further, but they finally induced a carbon lamp manufacturer in Ujpest, Hungary, to try out their lamp. Much further experimental work had to be done before the lamp could be produced commercially, the lamps being put on the market in Europe in limited quantities in September, 1906. They used the carbon filament displacement method at first, later the pressed filament. In July, 1905, they applied for a patent in this country. This lamp was originally nearly three times as efficient as the carbon lamp.

The General Electric Company bought Just and Hanaman's American patent rights and after much development work, marketed, early in 1907, a street series and 100-volt multiple lamp. The filament was rather fragile and the lamps had to be handled carefully. Notwithstanding the fragility, their high efficiency made them a great commercial success, the tungsten filament making the greatest advance ever made in the quality value of the vacuum incandescent lamp. 110-volt tungsten lamp of 1907, having an efficiency of 7.85 lumens per watt, were operated at the same efficiency as that of the tantalum lamp, it would last 27.1 times as long, making its advance over the tantalum lamp just ten times the advance of the tantalum over the Gem lamp. Nearly half a million tungsten filament lamps were sold during the first year, 1907.

Tungsten has a low electrical resistance, lower than tantalum, about half that of platinum and very much lower than that of carbon. However, when heated, tungsten increases greatly in resistance and even though the carbon filament decreases in resistance when heated, the tungsten filament in a lamp must be much longer and thinner than that in a carbon lamp. The 40-watt, 110-volt vacuum tungsten filament lamp has a

filament very nearly two feet long and about 1.6 thousandths of an inch in diameter. In order to get this long tungsten filament in a bulb, several hairpin loops of the pressed tungsten filaments were mounted on a spider, and connected in series with each other to get the requisite resistance for 110-volt circuits.

Series lamps were also put on the market which quickly displaced the carbon and Gem lamps used in street lighting. They not only consumed less energy for the same candle power given by the other lamps, but made it possible to greatly increase the lamp capacity of the constant current transformers used. As a result, larger sizes and greater numbers of street lights began to be used. The low resistance of tungsten made lower voltage lamps commercially feasible, so that in lighting trains 30- and 60-volt tungsten lamps immediately displaced the lamps formerly used. The lighting of automobiles with 6-volt lamps operating on storage batteries soon replaced the oil and acetylene lamps formerly used. Flashlights received a tremendous boom, as the 2.5 and 3.5-volt tungsten filament lamps tripled the capacity of the small dry batteries used."

Vita

David William Lipke was born to Arlene Gerken and Kenneth Lipke on November 6th, 1982 in Merrick, New York. He grew up in East Brunswick, New Jersey, graduating East Brunswick High School in May 2001. He earned his Bachelor of Science degree with honors from Harvey Mudd College in May 2005, majoring in Engineering. In May 2011, he will earn his Doctor of Philosophy degree from Georgia Institute of Technology, majoring in Materials Science and Engineering.

Beginning in January 2011, he will begin his professional career as a National Research Council Research Associate Fellow hosted by the Air Force Research Laboratory, Propulsion Directorate at Edwards Air Force Base.